Performance and Optimization of Large Deformable Elastic Braces for Seismic Resilient Structures

A dissertation submitted in partial fulfilment of
the requirements for the degree of

Doctor of Philosophy in Engineering

By

MD HARUN UR RASHID

Supervisor:
Professor Dr. Kiichiro Sawada
Assistant Supervisor:
Professor Dr. Tomohisa Hosoda
Professor Dr. Hiroki Hayashi
Associate Professor Dr. Takashi Shimizu

Graduate School of Natural Science and Technology
Shimane University, Japan
March 2026

Table of Contents

List of Figures & Photos

List of Tables

Abstract of the dissertation

Seismic resilience of building structures has historically focused on preventing collapse during major earthquakes, with less emphasis on post–earthquake functionality and residual deformations. Conventional seismic control systems, such as base isolation, hysteretic dampers, and buckling–restrained braced frames, can provide efficient protection, but they usually cause large permanent deformations that make structures in a state of severe post–elastic deformation, which may reduce their serviceability and economy. A comprehensive study of Large Deformable Elastic Braces (LDEBs) is presented in this dissertation, which are proposed as an innovative structural technology for limiting residual deformations while maintaining elastic behaviors under extreme seismic loading conditions that would otherwise lead conventional members to yield.

Large Deformable Elastic Braces adopt a new concept of seismic design, as elastic restoring forces act throughout seismic action, and structures return to their original positions even when beams or columns have experienced plastic deformation. Unlike traditional hysteretic dampers, which require plastic behavior to dissipate energy, LDEBs provide an elastic response over their wide range of deformation, up to 1/70 of their original length, as confirmed in our previous research [1,2]. This outstanding deformation capability is enabled by precision–engineered geometric forms realized from high–strength steel sheets by laser cutting, which provide complex cross–sectional shapes that result in good stress distribution and thus avoid early yielding.

This study focuses on three basic knowledge gaps regarding LDEBs. First, although the theoretical basis and initial validation existed, a thorough experimental verification under extreme deformation levels exceeding 1/200 and 1/80 of the original length had not been systematically completed. The second issue was the buckle under compressive loading, one of the main failure modes for bracing members and therefore required an intensive check to ensure they functioned reliably. Third, optimal stiffness distribution strategies for LDEBs in multi–degree–of–freedom

structures were not investigated, which limited their application in structural engineering design practice.

The experimental test employed three optimized LDEBs specimens (F1–1, F1–2, and F2) fabricated from JIS G 3106 SM490A steel with yield strengths of 325 MPa, 408 MPa & 411 MPa, respectively. Tensile loading tests were performed to more than 100 mm on specimens with a length of 660 mm, equivalent to story drift ratios from about 1/13 to 1/6.5. In addition, parallel finite element analyses with material nonlinearity and combined material geometric nonlinearity present complete numerical techniques. The research developed close form predictive equations derived from classical beam theory that enable practical calculation of yielding deformation and force without requiring complex numerical simulations. These equations agreed well with the experimental tests and predicted yielding loads of 2.901 kN, 2.88 kN, and 6.120 kN for the three specimens, which were in close agreement with the experimental results.

The investigation of compressive behavior used an eigenvalue buckling analysis, an energy–principles approach, and experimental validation to show that LDEBs can be designed so that yielding consistently precedes elastic buckling. The energy–based method, which accounts for torsional strain energy, yielded conservative estimates ranging from 19.52 kN to 39.00 kN, depending on the test specimen and boundary conditions, and were generally above the yielding loads, which is 3.0 kN. Experimental tests validate the design concept, with no signs of buckling observed in all tested specimens up to the ultimate load of 5.90 kN. It was found that buckling capacity increased by 40–100% with improved end restraint conditions, with a significant effect on connection design in practice.

The development of the optimization framework was a considerable methodological improvement over combining particle swarm optimization algorithms with full Round Robin response surface methodology for two–degree–of–freedom structural systems. This combined approach effectively found global optimal LDEBs stiffness distributions and, at the same time, assessed solution reliability under various ground shaking conditions and boosted waves, using three different ground motion records with intensities of 50 kine velocity and 90 kine velocity. The optimal solutions showed that LDEBs systems provide maximum story drift mitigation of 15%–64% compared to unbraced frames, with performance most effective at moderate seismic intensities where life safety is significant. It was found that optimal stiffness distributions are highly sensitive to earthquake intensity, structural natural periods, and ground motions with different frequency contents, leading to valley shaped response surfaces in the solution space.

The practical implications of this research extend beyond academic contribution to immediate engineering applications. The methodology for validated predictive equations enables approximate predictive assessment without recourse to be advanced finite element analysis; the energy–based buckling evaluation yields conservative screening tools for connection design; and the optimization approach provides a systematic means of obtaining performance–based forms from both a design and a retrofit perspective. It provides additional benefits in high seismicity areas that require post–quake performance and rapid recovery, as LDEBs systems can restore the residual value of structures that would otherwise need costly repairs.

This work establishes LDEBs as a seismic protection technology that has reached maturity, with full scientific validation spanning field tests to system optimization. The research provides theoretical background, validated design tools, and optimization frames to support structural engineers to confidently transfer LDEBs technology into performance based seismic design practice goals that contribute to the ultimate goal of making earthquake resilient infrastructure, not just to life safety but also damage recovery levels, where it may remain serviceable following major seismic incidents with retained functionality and economic worth, ready for serving communities in earthquake prone regions worldwide.

CHAPTER 1: INTRODUCTION

1.1 Introduction of Modern Seismic Design

The practice of earthquake resistant building design has developed from one–story force–based system and buildings to complex performance–based systems. A significant progress was achieved with the revision of Japan’s Building Standards Act in 1981, which transitioned the seismic design approach from a one–phase investigation into another way around two–phase checking because buildings were required to prevent from collapse during severe earthquake (JMA 6+ to JMA 7) besides being able to reserve an ability that preventing slight damage under a moderate–scale earthquake (JMA5+) [3,4]. This procedure included the structural characteristic factor (Ds coefficient), which combined the strength and ductility capacity of the structure [4]. There were also parallel conceptual developments in other countries, where similar factors were being found to apply factoring in that it is possible for buildings to absorb seismic shock by way of inelastic behavior [4]. The 2000 Building Standards Act revision in Japan adopted performance–based design methods that were based on the calculation of limit strengths and displacement–based methodologies [3]. Performance–based design systems provide the ability for designers to specify targeted goals from immediate occupation, down to collapse prevention at explicit detail of repairs and recovery time [5]. Performance-based seismic design has evolved significantly since the 1970s, when New Zealand pioneered capacity design principles, recognizing that displacement-based approaches offer more reliable performance indicators than traditional force-based methods [6]. The 1994 Northridge earthquake (Mw 6.7) also resulted in heavy damage and revealed deficiencies in the steel moment frame connections which led to major changes in the code provisions [7]. The 1995 Kobe (Great Hanshin–Awaji) Earthquake (Mw 6.9), with peak ground accelerations more than 0.8 g, resulted in the death of 6434 people and collapsed more than 240,000 buildings worth over $100 billion; approximately 90% of fatalities were due to collapse of pre–1981 structures [4,8].

The 2010 Chile earthquake (Mw 8.8) had less than 600 fatalities despite enormous magnitude, because of strict code implementation which indicates the efficiency of modern earthquake–resistant design [9]. The 2011 Great East Japan Earthquake (Mw 9.0) claimed over 18,000 lives mostly due to tsunami and its structural collapses owing to ground shaking were relatively limited [10]. A major seismic risk Japan is subjected to is the Nankai Trough, where it is anticipated that a serious earthquake will occur within only a few decades [6,11], with an increased focus on resiliency, asset protection and rapid restoration.

Seismic isolation technology employs flexible base interfaces such as natural rubber (NRB), high–damping rubber (HDRB), and lead–rubber bearings (LRB) systems that decouple buildings from high–frequency ground motions, lengthen structural periods from 0.5–1.0 s to 3–5 s, and reduce accelerations by 60–80 %, though their adoption remains limited by cost and displacement demands [12–14].

The buckling–restrained braced frames (BRBFs) overcome the buckling weakness of conventional bracing by enclosing a yielding steel core within a restraining mechanism that allows axial yielding and provides stable, symmetric hysteretic behavior, though limited post–elastic stiffness can cause P–delta effects and residual drifts of 0.8–2.0 % after design–level earthquakes [15–19].

Passive energy dissipation devices reduce seismic response by consuming kinetic energy as heat through metal yielding, friction or viscous fluid deformation that is supplied with metallic yielding dampers, friction dampers and viscous fluid dampers to obtain reliable energy absorption, yet the units need replacement after some large seismic events [20].

Self–centering systems improve defects of traditional systems which will accumulate plastic deformation with residual displacement leading to functionality loss [21]. These systems include elastic restoration elements that reduce the residual drift, without however losing dissipating energy capacity [21]. Tendons are often used in self–centering systems to provide restoring forces [21]. In shape memory alloys, super elastic behavior is observed whereby after deformation by up to 6–8 % without any plastic strain [22].

Although there have been major developments, the performance of any one seismic control strategy has limitations and is insufficient to reach its optimal resilience potential. Seismic isolation has economic barriers to widespread application and architectural issues [14]. BRB have residual displacements that need to be repaired for high rise buildings Additionally, BRB provides a low stiffness because of their yielding [18,19]. Self–centering systems reduce effectively residual drift but are based on expensive materials or complex devices [21,22]. The requirement for new approaches to achieve earthquake performance demands methods that can tackle multiple tasks while preserving practical feasibility for a widespread application [5]. An ideal system would provide large reductions in both maximum response and residual deformation, work well at the full range of earthquake intensity levels, and accomplish this with cost–effective construction practices, which are consistent with standard construction practice.

CHAPTER 2: LARGE DEFORMABLE ELASTIC BRACES

2.1. Large Deformable Elastic Braces (LDEBs) Introduction

This study proposed the large deformable elastic brace to address the limitations of conventional seismic control systems. Various methods have been developed to address checkerboard patterns in continuum topology optimization, including filtering techniques, morphological geometric representations with genetic algorithms, and Fourier-based representations for imposing length scale constraints [23]. This approach allowed multiple shapes to be made from a single steel plate model, optimized designs of which were manufactured using high strength steel (H–SA700) and physically tested and analyzed by Seism Struct software. Sawada et al. performed analytical study with finite element method to explain the relation between yield displacement and yield load, demonstrating that displacement increased and load decreased due to an increase in plate width, while Teramoto et al. also improved the technology by incorporating bending to enhance buckling resistance and compressive strength capacity [24,25].

LDEBs are devices that never yield, even when subjected to large deformations during major earthquakes, as introduced by Sawada [26] and representing a special class of structural components fabricated from steel plates with optimized geometric configurations that enable large elastic deformation at stress levels that would cause yielding in conventional members. The most important characteristic of LDEBs is how they operate; they do not dissipate energy by inducing permanent plasticity. LDEBs provide elastic restoration throughout the entire record of ground motion and actively restore the structure to its original position even after main frame members have yielded. LDEBs are developed through precision laser cutting process which allows exact reproduction of complex optimized geometries with fine tolerances, minimal material wastages. However, thermal effects induced by laser cutting can lead to hardening and residual stresses on material that could affect the mechanical performance of specimens, with standard dimension 660

× 200 × 9 mm thickness which are made from JIS G 3106 SM490A steel, whose yield strengths ranged from 325– 411 MPa and Figure 2.1 shown the standard geometry of the LDEBs [27].

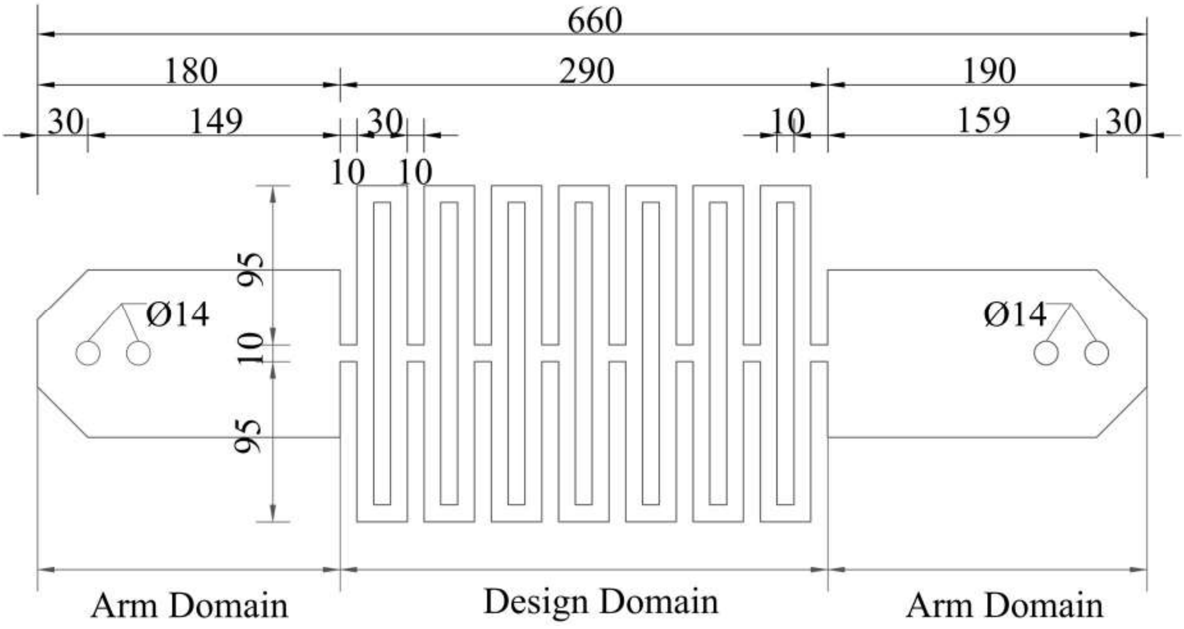

Figure 2.1 Typical geometric configuration of the large deformable elastic brace: arm domain (370 mm total length, 10 mm mesh) and design domain (290 mm length, 2.5–5 mm refined mesh). All dimensions in mm.

2.2 Comparative Analysis of Seismic Control Technologies

LDEBs represent a new seismic control technology which is distinct from traditional systems using elastic material properties to improve their seismic behavior [23,24]. Here are discussed the basic operational features and performance characteristics of LDEBs together with those of seismic control technologies such as seismic isolation and hysteretic energy dissipation devices.

Seismic Isolation Systems operate through period elongation and energy dissipation at the base level, shifting fundamental periods from 0.5–1.0 seconds to 3–5 seconds and achieving 60–80% reduction in superstructure accelerations [25–27]. Specialized elastomeric or sliding bearings (NRB, HDRB, LRB) accommodate large horizontal displacements while supporting vertical loads, maintaining the superstructure essentially elastic [27,28]. However, they have limitations such as requiring considerable vertical clearance, being very expensive to implement and not suitable for tall or irregular structures, the need of periodic bearing maintenance and possibly replacement after extreme events, and disadvantageous correspondence periods elongation for sites with long–period ground motions.

Vibration control systems are a broad group of structural seismic protection mechanisms, and dampers are the specific mechanical devices implemented by these systems [29,30]. Dampers are passive or semi-active systems installed in building structures to dissipate earthquake energy and minimize seismic vibration of the structure [31,32]. Recently, energy dissipation using damping devices as an effective adjunct to conventional strength- and ductility-based design is becoming more established [33, 34].

Dampers are categorized by their energy dissipation mechanisms into four primary types: viscous, viscoelastic, friction, and metallic yielding [35,36]. Hydraulic viscous dampers dissipate energy through fluid flow , and their force is directly proportional to velocity, which avoids residual deformation and allows the structure to fully recenter [37,38]. Viscoelastic dampers combine viscous and elastic properties such that the range in movement velocities at which energy is absorbed can be broadened [39,40]. Mechanical friction dampers are very simple and cheap and are based on the construction of interfaces that allow mechanical friction to convert kinetic energy into heat [39,40]. Metallic yield dampers, including buckling-restrained braces (BRBs), are designed to absorb seismic energy through the controlled yielding of specially engineered components [35,36].

Among these, buckling-restrained braces were first developed in Japan during the late 1980s and have since become widely employed in building structures worldwide [41–44]. BRBs are made of a ductile steel core that is confined to resist buckling under compression and to achieve symmetrical yielding in both tensile and compressive modes (rotation or translation) through the restraint mechanism provided by BRB action, thereby developing stable hysteretic loops [41,42].

However, as effective as they are, BRBs have a fundamental limitation in that they dissipate seismic energy through permanent plastic deformation, which results in residual deformation after a major earthquake, making them need to be replaced following large earthquakes with substantial economic losses and long downtimes [31, 32, 43, 44].

Hysteretic Energy Dissipation Systems work by controlling inelastic behavior, absorbing the seismic energy via stable plastic dissipation cycles [45–47]. Such systems are composed of metallic yielding dampers, BRBFs and steel plate devices which disseminate plastic energy over the structure [45, 48, 49]. They were to ensure symmetry in yielding under both tension and compression through buckling–restraining means, generating stable hysteric loops with improved energy dissipation [48–50]. However, there is a fundamental limit to the accumulation of plastic deformation; when attacked by design level earthquakes, they usually develop little residual drift per round 0.8–2.0%, which although ensuring that frames will not collapse can result in very costly retrofitting or complete demolition due to low post–yield stiffness and the associated increased sensitivity to the second–order P–Δ effect under severe loading [18, 45, 51]. Moreover, devices are usually not reusable after large earthquakes leading to more expenses, out–of–service downtime and lower post–earthquake operability [17, 45].

Large Deformable Elastic Braces (LDEBs) are innovative structural members designed to achieve large elastic deformation of specially shaped steel plates, which can sustain high levels of elastic strain without rupture under expected earthquake loads [52–55]. Unlike traditional hysteretic dampers, which require plastic behavior to dissipate energy, LDEBs provide an elastic response over their wide range of deformation and can provide a self–centering action that automatically pulls back to the structure's original position without external force [52]. This is due to a highly optimized geometry that distributes the load and enables an extremely high elastic strain capacity of the brace, far exceeding what could be achieved by regular steel members. Therefore, LDEBs can effectively control inter–story drift and reduce residual deformation under unloading, resulting in a high flexibility as well as strong restoring performance [52–55].

2.3 Research Gaps and Objectives

Review of relevant literature even though theory provides support and initial empirical validation for these relationships, there are several gaps in this research:

1. **Limited Experimental Validation Range:** The earlier experimental studies gave data of the LDEBs performance up to about 1/70th of its original length. Validations under large deformations higher than 1/10 original length representing extreme earthquake conditions are not yet available.
2. **Buckling Behavior Under Compression:** The buckling fatigue failure as induced by compression load is a major issue for any bracing component and has not been systematically addressed in the case of LDEBs. Although the problem of buckling restraint has been discussed in previous studies on folded braces [56], explicit techniques that guarantee LDEBs yield should be further explored.
3. **Optimal Stiffness Distribution Strategies:** Although optimization techniques have been used effectively for normal dampers and bracing systems, neither has found optimal spatial distributions of stiffnesses for LDEBs in multistory buildings. Since LDEBs have unique elastic properties, specific optimization schemes taking into consideration their extended elastic limits and restoring–force parts are necessary.
4. **Validation of Global Optimality:** Optimization research commonly uses metaheuristic algorithms, which are far from the global optimal solution. The complex, potentially multimodal response surfaces of MDOF systems with LDEBs require robust validation techniques.

This research fills in these gaps through the combined experimental, analytical, and optimization analyses and thus provides a solid scientific/engineering basis for LDEB design, analysis, and optimal development for seismic use. The specific objectives are:

1. **Experimental and Analytical Validation of Tensile Performance**: Perform tensile loading tests on optimized LDEB plates that are conducted until the deformation range of 1/200 and 1/80 of the original length and comparison of experimental performance with finite element results which include material nonlinearity (MNL) and combined material & geometric nonlinearities (M&GNL).
2. **Development of Predictive Models:** We use classical mechanics to build theoretical equations to predict the yielding deformation and force for LDEBs, which allows for practical design calculations without the need for complex numerical simulations.
3. **Investigation of Buckling Prevention**: Study the compressive behavior of LDEBs through finite element eigenvalue and experimental testing to provide the design configurations for making yielding occur before buckling, therefore keep intact under compression.
4. **Stiffness Distribution Optimization:** Develop and solve the stiffness distribution optimization problem for generating optimized LDEBs stiffness distributions in a multi degree of freedom structural system by aggressively designed particle swarm optimization (PSO) algorithms, complemented with extensive Round Robin response surface investigation.
5. **Seismic Performance Evaluation:** Verify that the optimal LDEBs design can be applied against several seismic demands, such as different levels of intensity with respect to frequency contents and correspondingly show superior performance.

CHAPTER 3: PERFORMANCE OF OPTIMIZED LARGE DEFORMABLE ELASTIC PLATES

3.1 Introduction

Public awareness of earthquake safety has grown significantly in recent years. This has led to a growing focus on comprehensive earthquake preparation, aiming not only to safeguard lives during major earthquakes, but also to protect the integrity and value of buildings as critical assets. Traditional seismic control structures and isolation structures have been effective in minimizing damage to columns and beams in large buildings, like disaster prevention bases [46–48, 57, 58]. These advancements are the result of years of dedicated research.

However, these methods seem to require a high cost. This paper explores Large Deformable Elastic Plates (LDEPs) [26, 59–61] as a promising alternative for addressing residual deformations after earthquakes. LDEPs are intended for use as braces or knee braces within buildings, those are called Large Deformable Elastic Braces (LDEBs). LDEBs are unique structural components that can deform significantly without permanent damage. Unlike conventional seismic control methods, LDEBs employ distinct response reduction mechanisms [60].

It's important to distinguish LDEBs from hysteresis dampers, which are energy–absorbing devices commonly used in seismic mitigation [50, 52, 55]. While both aim to reduce maximum deformations, they achieve this in different ways. Hysteresis dampers absorb energy through a process called plasticization, which results in permanent changes to their structure. While this process helps protect the main frame during seismic events, in the case of very strong earthquakes, both the dampers and the main frame may experience permanent deformation, reducing their overall effectiveness.

LDEBs, on the other hand, maintain their elasticity even under large deformations. This allows them to provide substantial restoring forces that help pull the structure back into shape after an earthquake. While LDEBs might allow for slightly larger deformations compared to dampers, their ability to maintain elasticity ensures their continued effectiveness in reducing residual deformations [26, 60]. By incorporating LDEBs into structures, their elastic properties offer a viable alternative for seismic mitigation.

Indeed, minimizing residual deformation is the most challenging aspect of the seismic resilience target because, as post–earthquake functional requirement, it dictates the serviceability and safety of buildings after an earthquake. This is decreased structural strength, higher maintenance costs, and in extreme cases demolition, which has extensive costs in a densely populated city. LDEPs are uniquely positioned in this context. They serve as secondary stiffness to the fundamental frame of the building by providing an additional restorative force, and they do so without the negative implications of period shifts of the superstructure or early onset of inelastic deformation found in some other systems.

Potential benefits of LDEPs include high reusability, low maintenance costs, and better post–earthquake functional performance following aftershocks. However, this new technology presents challenges, particularly in optimizing material properties and geometric configurations to achieve the desired performance metrics. Careful calibration is required to ensure that the LDEPs meet their intended structural and functional objectives.

To develop ground property measurement technique, and spread of sensors, it is now not so difficult to clarify the dominant period property of site. Then, it is likely to be of particular interest at the design stage to choose devices which shift respectively the building natural period toward a shorter side, longer one or do not really modify it. As a result, there is great expectation for the advent of a variety of responding reduction instruments having improved performance characteristics.

A primary challenge in the use of large deformation elastic braces is that it is difficult to prevent buckling of the large deformation elastic plates formed under a compression load. Previous investigations presented tests on these plates by stabilizing them against buckling with channel sections [62]. In addition, examples of large deformation elastic members that are effective even under compression have been suggested [63].

This investigates the high elastic property of LDEPs through a systematic study of tensile and compression phenomena. We performed experimental tests and FEM simulations for both loading cases. Moreover, we also investigate plastic deformation after yielding as an extremely rare event for reference. In our previous research [59, 61], tensile tests or nonlinear analysis have already been conducted on LDEPs up to the range of small plastic deformation (up to around 1/70 of the original length of the plate), however, here we conduct a tensile test up to the range of large plastic deformation (around 1/10 of the original length of the plates). We primarily established demands of LDEPs, then applied a topology optimization method to find the optimal topologies. Then numerical simulations of linear and nonlinear mechanical behavior are performed, which are validated with experiments.

The first part of this chapter concentrates on tensile properties, in that a theoretical model has been developed to predict the tensile yield load and displacement. In the second part we perform FEM linear compressive load analysis and eigenvalue buckling analysis for large deformation elastic braces under several kinds of boundary conditions and investigate the condition where elastic buckling load is larger than compressive yield load. We also derived linear buckling equations for torsion from energy considerations and experimentally confirmed these equations using a universal tester. Load testing verified that the system achieves a high elastic limit response, and no buckling was observed at any load level. The results of this study help in the development of light weight, high strength structures for many engineering applications.

A similar study to our approach has been conducted on the folded brace [56], however it differs from our approach in terms of the manufacturing method and the target of expanding the elastic limit at a story drift angle of around 1/200. However, our study focusses on enhancing the elastic limits at a story drift angle of 1/100 to 1/50 as introduced in section 3.2.1

3.2 Under Tensile Load

3.2.1 Demands for performances of LDEPs

The LDEPs are flexible members that retain elastic properties, even for large deformations under major earthquakes as we mentioned earlier. The building structure frame gets secondary stiffness, that is, elastic resilience by incorporating LDEPs into the whole frame system as knee braces. In this way, even after the columns and beams have plasticized, the elastic resilience can make the whole frame still resist deformation and regain its initial forms. As a result, the residual and maximum deformation of the building is reduced [50, 53, 64]. Furthermore, A response analysis on a portal steel frame of an earthquake response showed that using LDEPs as knee braces with an axial stiffness of only 500 N/mm (which gives a horizontal stiffness of approximate 15% of the horizontal stiffness of the main frame) reduced the maximum deformation response by around 20% and the residual deformation response extremely [61, 64–66]. The demand story drift angle in a major earthquake is approximately between 1/100 and 1/50, while a large deformation elastic member inclined at 45° requires at least 1/140 and 1/70 of the original length as the elastic deformation [61].

Consequently, in this paper, the following demands are considered for the performances of LDEPs as knee braces for the portal frame.

(1) Axial stiffness of around 500 N/mm

(2) large elastic deformation of 1/70 to original length corresponding to 1/50 of story drift angle.

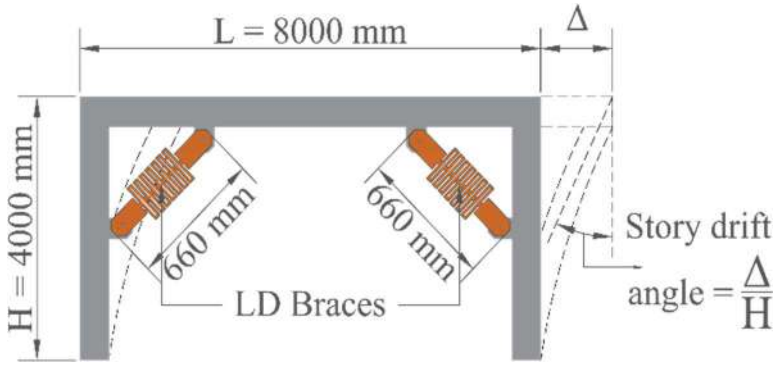

Figure 3.1. Inter story drift and angle with LDEPs (Reference [27]).

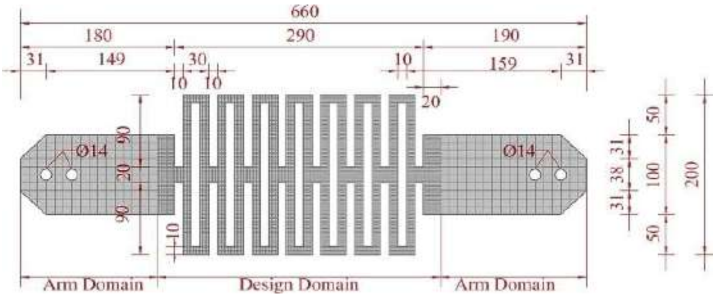

Figure 3.2. F1–1 & F1–2 large deformable elastic plates topology (Reference [27]).

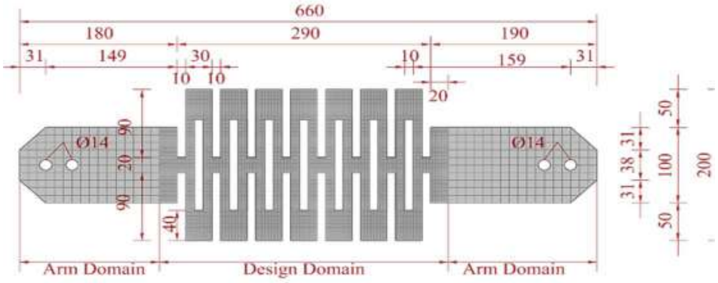

Figure 3.3. F2 large deformable elastic plates topology (Reference [27]).

3.2.2 Formulations of LDEPs

3.2.2.1 *Multi objective optimization problem* [59]

In this study, we selected three model specimens shown in Figure 3.2 & Figure 3.3 among the multi objective solutions [59]. The specimen F–1 has the largest yielding deformation among the multi–objective solutions. The specimen F2 has the yielding load capacity to some extent. The multi objective optimization was solved by genetic algorithm (NSGA–II). The optimization problem is formulated based on a four–column method posts mentioned in 3.2.2.2. This method involves dividing the LDEPs into rough rectangular elements and representing each element as either solid or void, according to design variables. The NSGA–II was used to explore the design space and provide a Pareto in front of non–dominated solutions, each representing a different balance between the objectives. The two objectives' functions are to maximize tensile yielding deformation and maximize tensile yielding load. These two objectives often conflict with each other, meaning that increasing one can reduce the other. The optimization aims to find a balance between these objectives. The optimization problem is defined with design variables x_1 and x_2 which represent the positions of the solid and void elements in the four–column topology. The problem is solved by finding the combination of x_1 and x_2 that maximizes both tensile yielding deformation (U_y) and tensile yielding load (P_y).

$$f_1 = U_y = U\frac{\sigma_0}{\sigma_{M\,\max}} \qquad \text{and} \qquad f_2 = P_y = P\frac{\sigma_0}{\sigma_{M\,\max}}$$

where,

f_1 & f_2 *is* the objective function for the multi objective optimization problems.

U is the maximum tensile displacement in all nodes by static linear FEM.

P is the total tensile load in all nodes by static linear FEM.

σ_0 is the tensile yield strength of steel plate material.

$\sigma_{M\,\max}$ is the maximum value of von Mises stress in all nodes.

3.2.2.2 *Four–column formulation* [59]

The four–column formulation topology representation is used to get the optimal solutions sufficiently and simply [59]. This approach defines the topology of the material by specifying, for each of the finite elements in a grid, whether that element is solid or void. Finite elements are arranged in a grid, and the z_{ij} value for each element is assigned to 1 (solid) or 0 (void). The procedure for determining the value of z_{ij} is described as follows:

The finite elements grid is arranged by column (i) and row (j), and then the index i is divided by 4. The remainder of this category (written as MOD(i/4)) is used to classify the elements (i,j) into one of four possible cases.

Case 1: When MOD(*i*/4) = 0:

For elements where the column number i, gives the reminder of i is divided by 4, the element z_{ij} is determined by the row number j:

- When the element is solid: $z_{ij}= 1$ if ($j \leq x_1$ or $j \geq ny - 2 - x_1$).
- When the element is void: $z_{ij} = 0$ if ($ny - 2 - x_1 > j > x_1$).

Case 2: When MOD(i/4) = 1:

- For elements where MOD(i/4) = 1, all elements (i,j) is solid: $z_{ij}=1$

Case 3: When MOD(i/4) = 2:

For elements where MOD(i/4) = 2, the decision is like Case 1 but using x_2 as the reference point instead of x_1:

- When the element is solid: $z_{ij}=1$if ($j \leq x_2$ or $j \geq ny - 2 - x_2$)
- When element is void: $z_{ij} = 0$ if ($ny - 2 - x_2 > j > x_2$)

Case 4: When MOD(*i*/4) = 3:

- For elements where MOD(i/4) = 3, all elements (i,j) are solid: $z_{ij}=1$

where,

x_1, x_2: Integer design variables that define the boundaries for the regions where elements are solid or void.

i: column number of finite element (i,j) ($i = 0,1, 2, \dots nx - 1$).

j: row number of finite element (i,j) ($j = 0, 1, 2, \ldots ny - 1$).

This set of rules is applied to all finite elements in the grid to generate a topology where certain elements are solid, and others are void based on the design variables x_1 and x_2.

3.2.3 Analysis

3.2.3.1 *FEM linear analysis and an evaluation by von mises condition*

This study investigates the behavior of large deformable elastic plates (F1–1, F1–2 & F2) undergoing significant deformation under tensile load. For finite element method (FEM) linear analysis software, LISA [67], is used to determine the deformation and Von Mises stress distribution in Figures 3.4–3.6 (A–B). The three models' specimens have dimensions of 660 mm by 200 mm. All plates are made of JIS G 3106 (SM490A) steel with a Young's modulus of 205 GPa, a Poisson's ratio of 0.3, and a thickness of 9 mm. Yield strengths (σ_y) are 411 MPa for F1–1 and 408 MPa for both F1–2 and F2. The yield strengths are obtained from two different mill sheets. Here, the boundary condition in the nodes (Fix0) at the left end of the single–sided side are fixed nodes in all directions. At the right end are free and applied the tensile load (F_{xt}) 220 N. However, the plate total length is divided into two segments: (i) the design domain 290 mm and meshed more finely with 4–node plane stress elements of 2.5 mm mesh; (ii) the arm domain 370 mm and meshed with 4–node plane stress elements of 5 mm mesh.

Figures 3.4–3.6(A–B) represent the displacement, and the von Mises stress distribution that most just satisfies von Mises yield condition. It is obtained through linear finite element analysis with a 2.5 mm mesh, and the multiplication factor just satisfies the condition. At the initial yielding point, as shown in the post–processing results in Figures 3.10(A)–(C). However, Table 3.1 presents the linear analysis results of F1–1, F1–2 & F2 model spacemen's, indicating a tensile yielding displacement for all plates are 8.10 mm, 8.05 mm and 3.07 mm and a tensile yielding load for all plates is 2471 N, 2453 N & 5656 N. The yield load and displacement in Table 3.1 was calculated from the load factor that most just satisfies the von mises condition.

For instance, (F1–1 specimen)

Tensile Yield Load $= \dfrac{F_{xt}\sigma_y}{\sigma_v} = \dfrac{220}{36.59} \times 411 = 2471.00N$

Tensile Yield Displacement $= \dfrac{\Delta_x \sigma_y}{\sigma_v} = \dfrac{0.722}{36.59} \times 411 = 8.10mm$

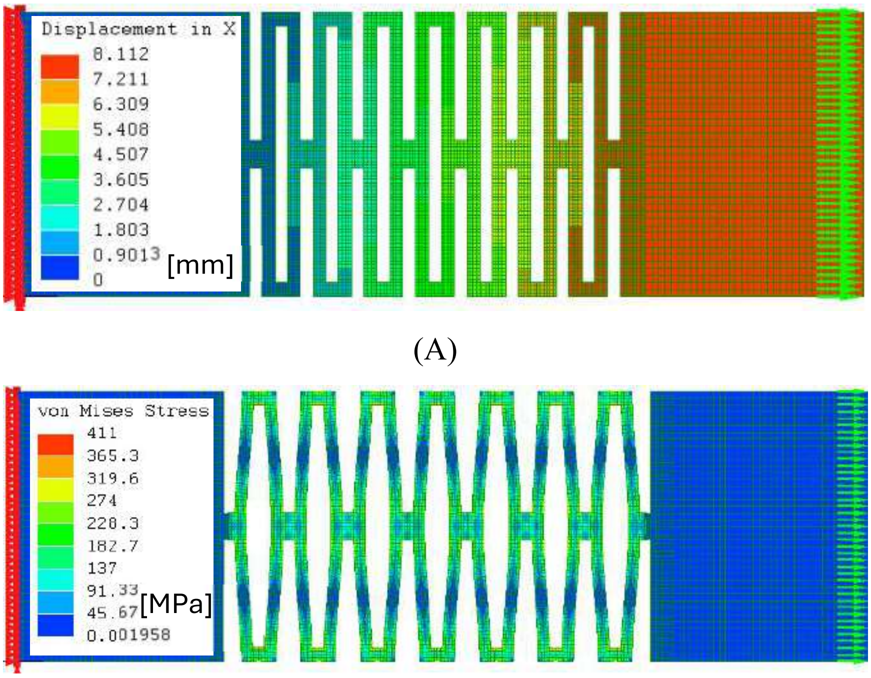

(A)

(B)

Figure 3.4. Finite element analysis of LDEPs F1–1 showing (A) displacement distribution in X–direction and (B) von Mises stress distribution (Reference [27]).

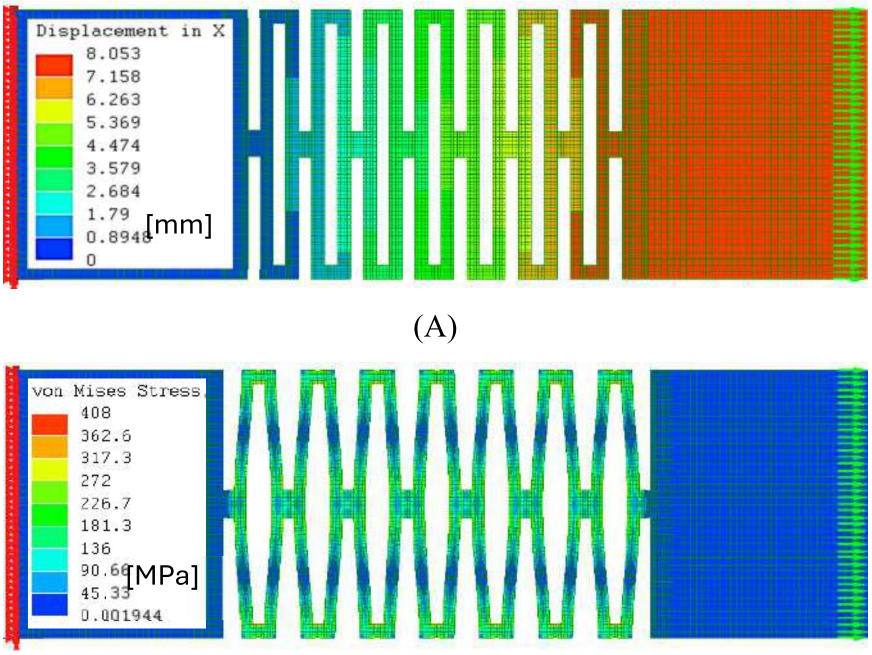

(A)

(B)

Figure 3.5. Finite element analysis of LDEPs F1–2 showing (A) displacement distribution in X–direction and (B) von Mises stress distribution (Reference [27]).

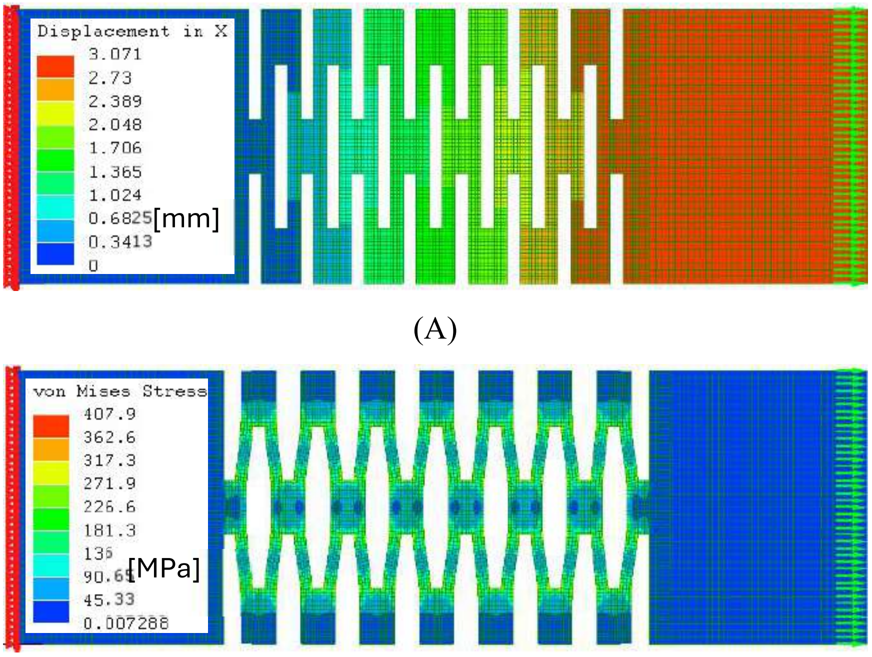

(A)

(B)

Figure 3.6. Finite element analysis of LDEPs F2 showing (A) displacement distribution in X–direction and (B) von Mises stress distribution (Reference [27]).

Table 3.1. Tensile yield load and tensile yielding displacement calculated based on analysis results by Lisa 8.0 and von mises condition at applied load (F_{xt}) on 220N.

Specimen / Plates	Linear Analysis Displacement (Δ_x)	Mises Stress (σ_v)	Tensile Yield Load $\left(\frac{F_{xt}\sigma_y}{\sigma_v}\right)$	Tensile Yield Displacement $\left(\frac{\Delta_x\sigma_y}{\sigma_v}\right)$
Unit's	mm	MPa	N	mm
F1–1	0.722	36.59	2471	8.10
F1–2	0.722	36.59	2453	8.05
F2	0.120	15.87	5656	3.07

3.2.3.2 *FEM nonlinear analysis*

In this study, the analysis used a uniaxial stress–strain relationship to capture material nonlinearity. The arc–length increment method was applied to ensure accurate equilibrium path tracing, particularly under large deformations. This method allowed for more stable and accurate simulations, especially for materials exhibiting nonlinear behavior after yielding, which is crucial for analyzing large deformable elastic plates.

Fortran, a pioneering programming language in the world of scientific and engineering computing, remains a staple in the domain of structural analysis, particularly when dealing with complex nonlinear problems. In our study, we utilized Fortran in conjunction with HYPLAS_v2.0, a specialized finite element analysis tool, to accurately simulate the behavior of materials and structures under extreme conditions. By incorporating both material nonlinearities (MNL), where stress–strain relationships deviate from linearity due to plastic deformation, and material & geometric nonlinearity (M&GNL), where large deformations alter the structure's load–bearing capacity. This program used finite element analysis (FEM) mesh grid with global co–ordinate conditions. The analysis condition and the material properties are like FEM linear analysis. A quadrilateral four–node element (QUAD_4) is employed within a single element group.

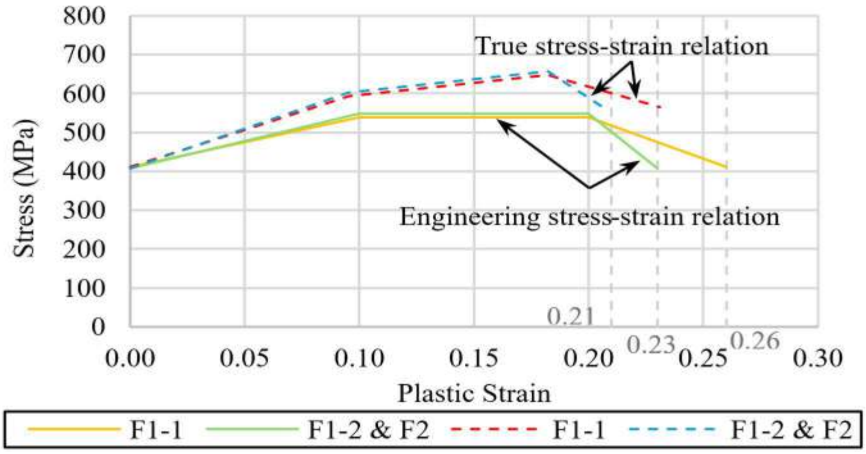

Figure 3.7. Stress–strain relationship during plastic deformation (Reference [27]).

A true stress–true strain relationship (See Figure 3.7) is used in Material and Geometric Nonlinear (M&GNL) analysis, while an engineering stress strain relationship (See Figure 3.7) is used in Material Nonlinear (MNL) analysis. An approximation of four–fold points and three lines is used as the engineering stress–strain relationship. The folding points are determined by mill certificates and a typical engineering stress strain curve shape [68]. Referring to [69], the true stress relationship is obtained from a direct output, that is, true stress $\sigma_t = \sigma_e(1+\varepsilon_e)$, and true strain $\varepsilon_t = \ln(1+\varepsilon_e)$, from the engineering stress–strain relationship. Here, σ_e and ε_e represent engineering stress and strain. Consequently, the material properties are not strictly bilinear.

A partial model

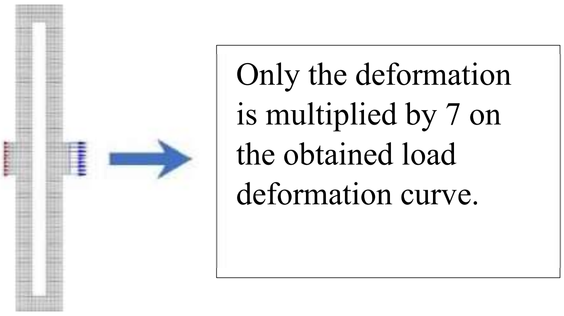

Only the deformation is multiplied by 7 on the obtained load deformation curve.

Figure 3.8. A partial model of LDEPs (Reference [27]).

In the nonlinear analyses of this study, a partial model shown in Figure 3.8 is analyzed. After the analysis, only the deformation is multiplied by 7 on the obtained load deformation curve. The material properties are the same as section 3.2.3.1 except for nonlinear properties and the nonlinear properties used the isotropic hardening rule.

3.2.4 Tensile experimental test specimens

This study investigates the behavior of a 9 mm thick three steel plate (JIS G 3106 SM490A) shaped using a laser cutting machine in Photo 3.1. The steel plates used in this study have a yield strength (σ_y) of 411 MPa for F1–1 and 408 MPa for F1–2 & F2, as verified by the two different mill sheets. The tensile tests were conducted on specimens using a universal testing machine at Shimane University in Photo 2(A)–(C). In addition, to improve the experiment's accuracy, the testing specimens were cut into suitable shapes, and the gripping part of the large deformable elastic plate was explored to prevent skidding.

(A)

(B)

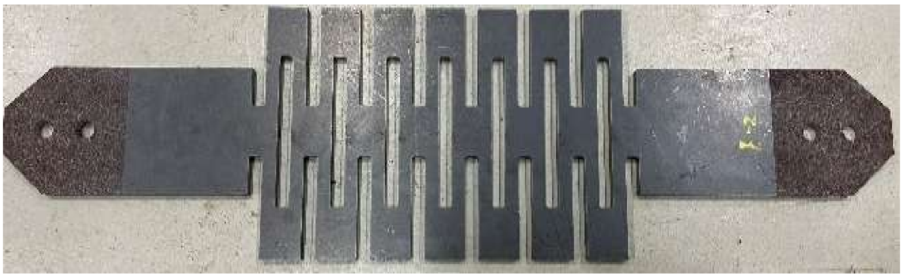

(C)

Photo 3.1. Large Deformable Elastic Braces: (A) F1–1; (B) F1–2; (C) F2 (Reference [27]).

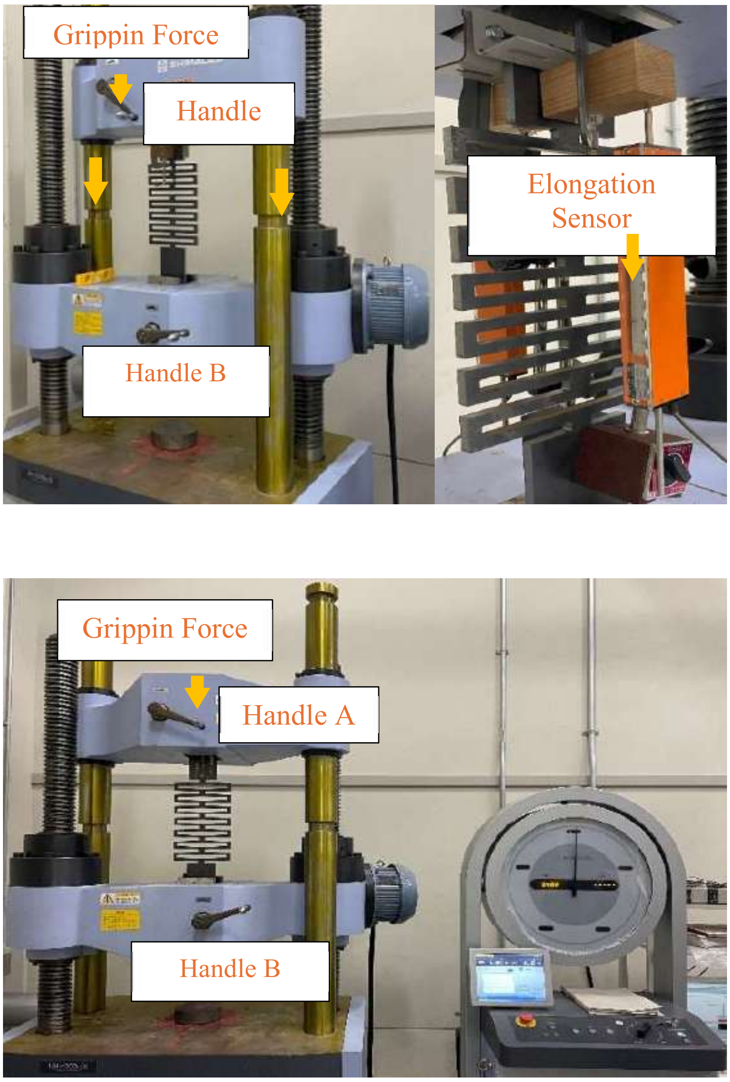

(B)

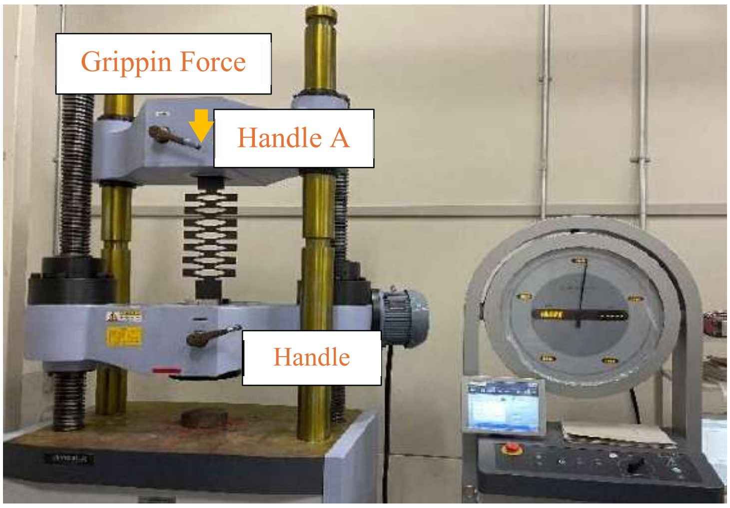

(C)

Photo 3.2. Tensile experiments by universal testing machine: (A) F1–1; (B) F1–2; (C) F2 (Reference [27]).

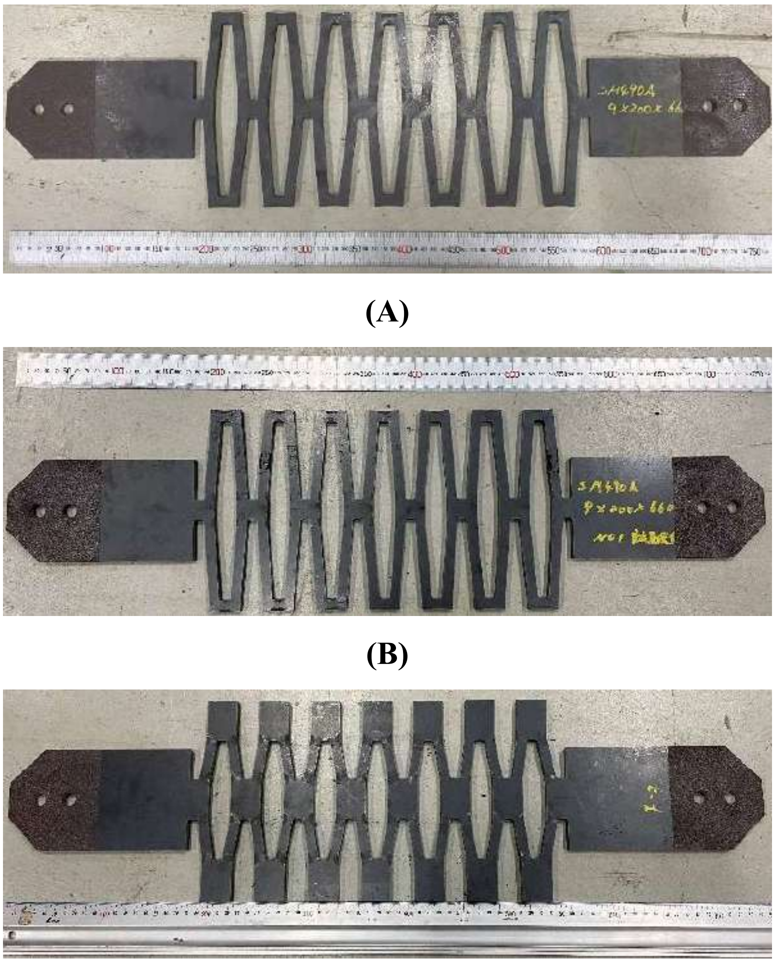

(A)

(B)

(C)

Photo 3.3. Model after tensile experimental tests: (A) F1–1; (B) F1–2; (C) F2 (Reference [27]).

3.2.5 Results of numerical analysis and experiment

Figures 3.10(A)–(C) show experimental test results (load vs. tensile deformation curves). The experimental test results show initial slight fluctuations around the 400 N loads marked on orange circle in Figures 3.10(A)–(C). At an early stage (up to around 1200 N) during the tests, the gripping handles A and B were applied manually according to arrows in Photo 3.2(A)–(C). Then, F1–1 specimen was loaded until the displacement transducer picked its limits, that is ratio of deformation to original length is around 70 mm / 660 mm followed by unloading. However, the ratio corresponds to around 1/13 of the story's drift angle. After the unloading, F1–1 specimen was again loaded and measured by displacement gauge built into the head of the universal testing machine until the ratio of deformation to original length exceeds 100 mm / 660 mm followed by unloading. The final state is shown in photo 3.3(A). F1–2 and F2 specimens were loaded and measured by the built–in displacement gage from an initial stage until the ratio of deformation to original length exceeds 100 mm / 660 mm followed by unloading. The final states are shown in photos 3.3(B) and (C).

Figures 3.10(A)–(C) also represent load deformation curves or stiffness lines obtained from the Material Non–Linear analysis (━MNL), Material and Geometrical Non–Linear analysis (━M&GNL), static linear analysis (– –linear analysis) as well as experimental tests (━Test). Figures 3.10(A)–(C) also show yielding points for three curves (○Test_yp, ╳ MNL_yp, and □ M&GNL_yp). The yielding points were evaluated by 95 % point of maximum ratio of the load to the deformation ratio. This method ensures consistency across the evaluated methods while approximating the onset of yielding, as illustrated in Figure 3.9. The approach facilitates comparative analysis of material behavior under different modeling assumptions. Figures 3.10(A)–(C) also show initial yield points that just meet the Von Mises yield condition (○ Mises_yp) plotted from Table 3.1. It is observed from the Figures that the stiffness lines by linear analysis correspond exactly to the initial stiffness of MNL and M&GNL. Moreover, from the Figures, Mises_yp points underestimate yield load and yield deformation compared to three yielding points (Test_yp, MNL_yp, and M&GNL_yp), while they seem to correspond roughly to one another.

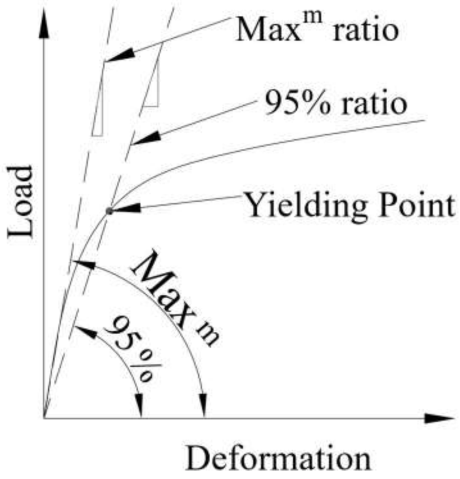

Figure 3.9. Load–deformation curves yield points determined by the 95% maximum load–to–deformation ratio (Test, MNL, and M&GNL) (Reference [27]).

However, after the load increases beyond 4.5 kN, the materials (F1–1 & F1–2) begin to plastically deform, while the F2 plate requires 10.1 kN. As a result, the differences between the curves become more pronounced. As the material deforms plastically (beyond its elastic limit), material hardening occurs, meaning the material becomes stronger and more resistant to further deformation. This behavior is reflected in the blue (Test) curve, where the tensile load continues to increase even as the deformation progresses. The presence of heat hardening in the experimental data causes the material to withstand higher loads compared to the gray (MNL) and red (M&GNL) curves. These models do not fully capture the heat hardening effects observed in the experiment, likely contributing to the lower predicted load capacity in the simulations. Previous research [70–76] found that material hardening from thermal effect by laser cutting significantly influences the behavior of the material.

Table 3.2. Comparison of tensile load and displacement across different methods at the deformation of 70.0mm.

Methods	Tensile Load (kN)	Tensile Deformation (mm)
Test (F1–1)	6.020	70.00
MNL	5.107	70.00
M&GNL	5.261	70.00

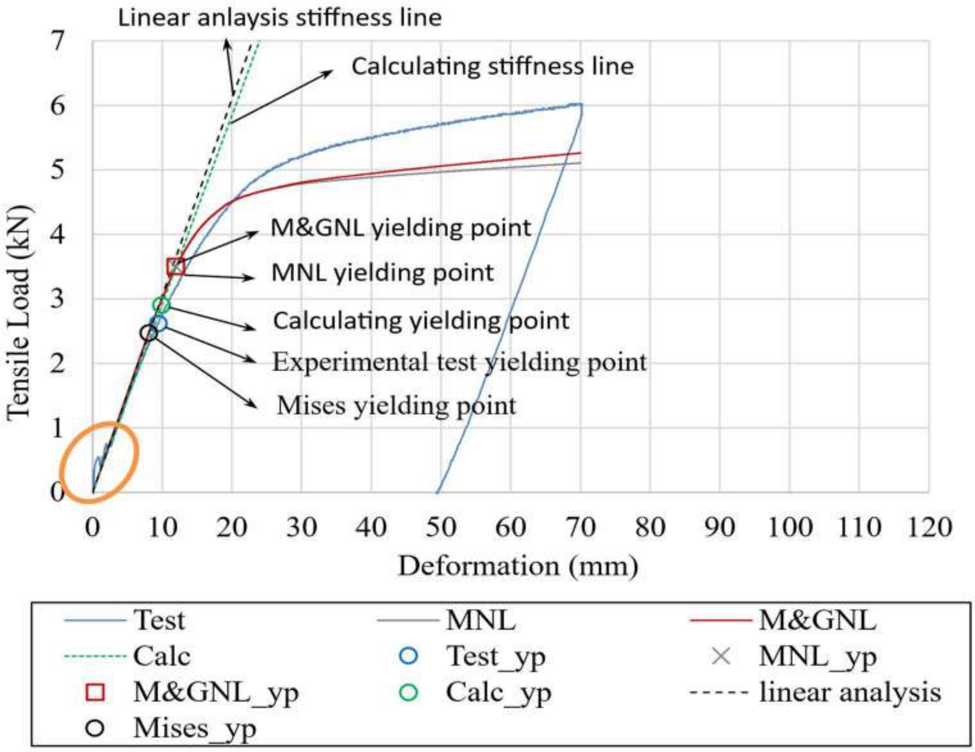

Figure 3.10(A). Tensile load shaped curve for F1–1 (Reference [27]).

Figure 3.10(A) Illustrated of a specimen F1–1; the three curves (Test, MNL, M&GNL) start from the origin and initially follow a similar path. This region is called the elastic zone, where the tensile load increases linearly with the deformation. However, compared to MNL and M&GNL, the test curves have an early yielding. The reason is the effect of residual stress, which is a cross–ponder of previous research [70–76]. As the deformation increases beyond the elastic limits, the material undergoes plastic deformation, leading to large plastic deformation capacity during severe earthquakes. However, both numerical models (MNL and M&GNL) show likely similar trends, suggesting that the numerical models could withstand more load before significant deformation and the end curve data shown in Table 3.2. Previous research [61] also found that the numerical models of material non–linearity and material & geometric non–linearity analysis results are approximately similar.

Table 3.3. Comparison of tensile load and displacement across different methods at the deformation of 110.0mm.

Methods	Tensile Load (kN)	Tensile Deformation (mm)
Test (F1–2)	5.840	110.00
MNL	5.372	110.00
M&GNL	5.612	110.00

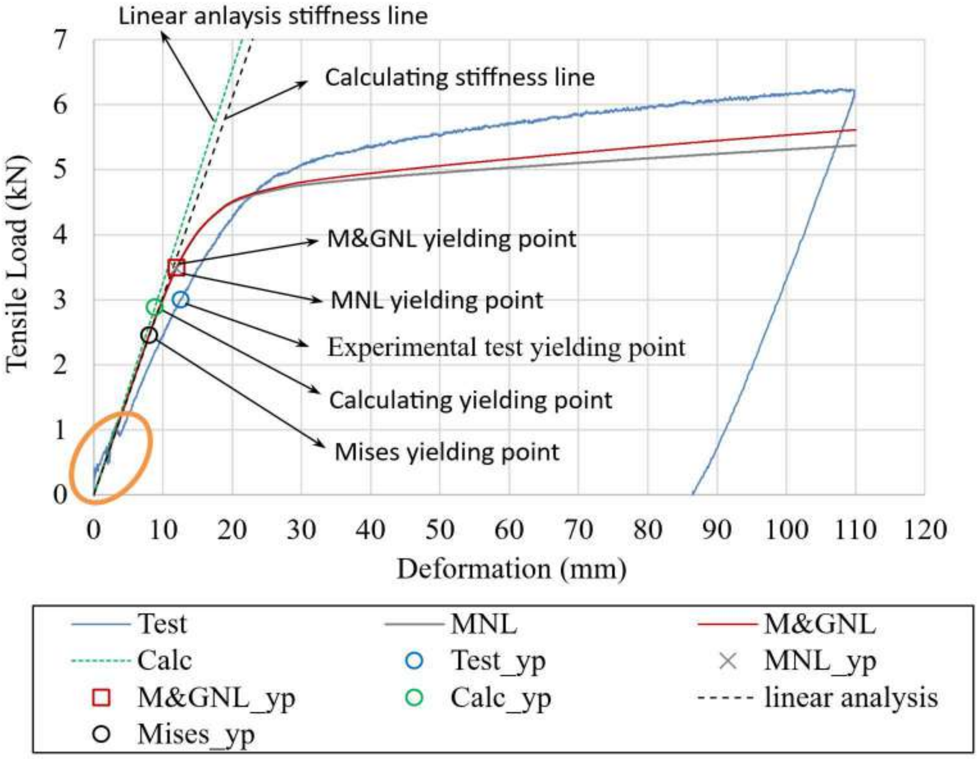

Figure 3.10(B). Tensile load shaped curve for F1–2 (Reference [27]).

Figure 3.10(B) shows the corresponding load–deformation response of specimen F1–2. The blue experimental curve represents the transition from elastic to plastic deformation of the material, with the yielding point denoted by the blue circle. The yielding displacement obtained from this curve is overestimated. The yielded point from the simulation of the M&GNL model has no differences with the MNL model numerical analysis results, and both curves exhibit a similar tendency, as shown in Table 3.3 and the curve data. F1–2 specimens exhibit a similar tendency to F1–1 specimen. The linear analysis results are representative of the initial stiffness, while the stiffness calculated from the models' predictions is represented by the green dotted line. The actual experimental test results show a larger yielding displacement. Therefore, the yielding displacements calculated by the MNL, M&GNL, calculated stiffness line, and linear analysis stiffness line are underestimated, while the linear analysis stiffness line corresponds to the MNL and M&GNL analysis results.

Table 3.4. Comparison of tensile load and displacement across different methods at the deformation of 101.00mm.

Methods	Tensile Load (kN)	Tensile Deformation (mm)
Test (F2)	16.280	101.00
MNL	12.617	101.00
M&GNL	14.020	101.00

Figure 3.10(C) demonstrates the load–deformation behaviors for the F2 specimen. The blue experimental curve shows the transition from elastic to plastic deformation in the material, and the yielding point is denoted by the blue circle. However, the yielding displacement obtained from this curve is an overestimation. As shown again in Table 3.4 and the curve data, it can be found that the yield point of the M&GNL simulation corresponds to that of the MNL model, and the trends of both curves are also basically consistent. The initial stiffness (from linear analysis) is indicated

with the black dashed line, and the calculating stiffness from the model predictions is indicated with a green dotted line. The results show that, experimentally, the yielding displacement is much larger. As a result, the yielding displacements obtained from the MNL, M&GNL, calculated stiffness, and linear analysis stiffness lines are underestimated, while the linear analysis stiffness line corresponds to the MNL and M&GNL analysis results. However, the behavior of F1–2 and F2 material models was also similar to that of F1–1 material model.

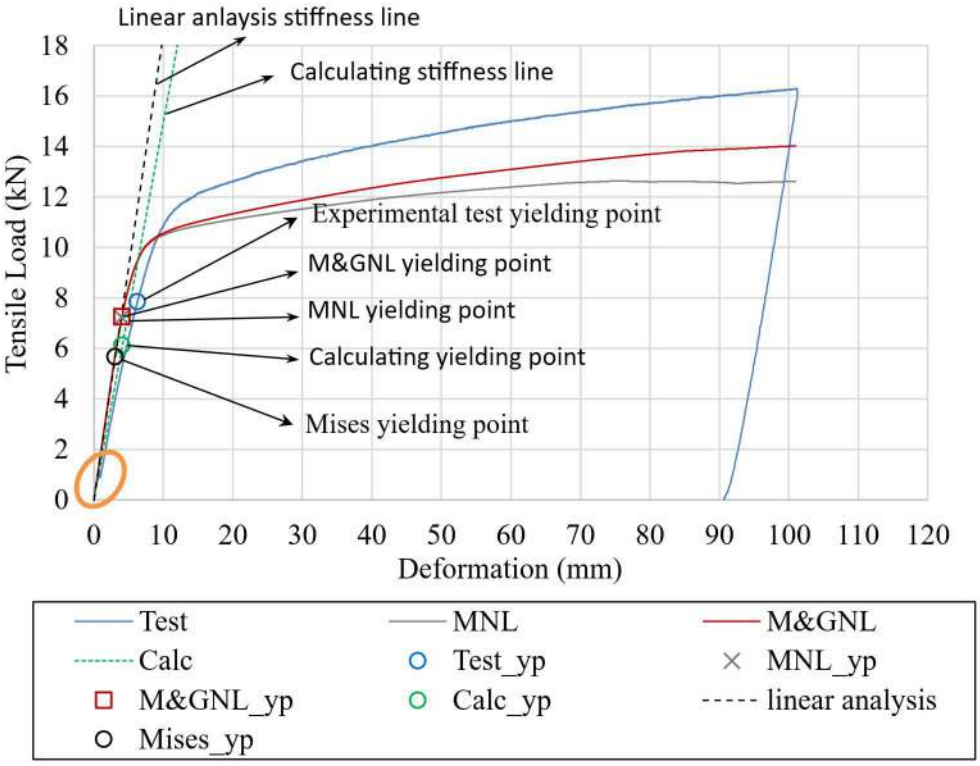

Figure 3.10(C). Tensile load shaped curve for F2 (Reference [27]).

3.2.6 Predictive equations for yielding deformation and force in LDEBs plates

This study finds a possible numerical calculation of the tensile–yielding displacement and tensile–yielding force in LDEPs. Figures 3.4–3.6(A), (B) show the Von Mises stress distribution, which indicates the Von Mises stress uniformly distribution in seven springs. Based on such kind of stress behaviors, we selected one LDEPs spring for developing numerical calculation. The geometrical properties of one spring are shown in Figure 3.11(a), and the dimension is 200 mm length and 30 mm width. Also shown in the cross–sectional details of LDEPs spring flange. Figure 3.11 (b) & (c) shows a face free body diagram and moment diagram, where the load (F_{xt}) is applied into the center and the support is fixed with both ends for calculating LDEPs spring face moments.

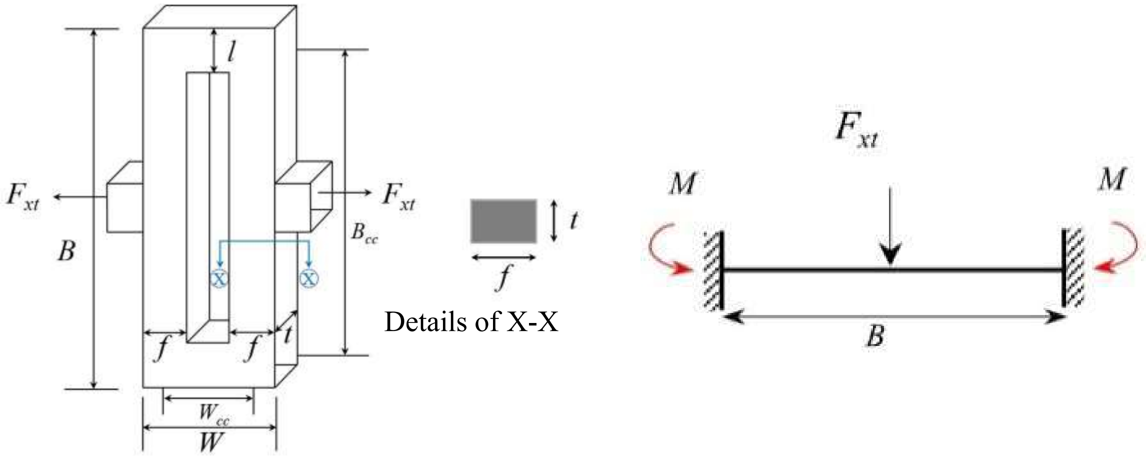

(a) One spring of LDEPs.

(b) Free body Diagram

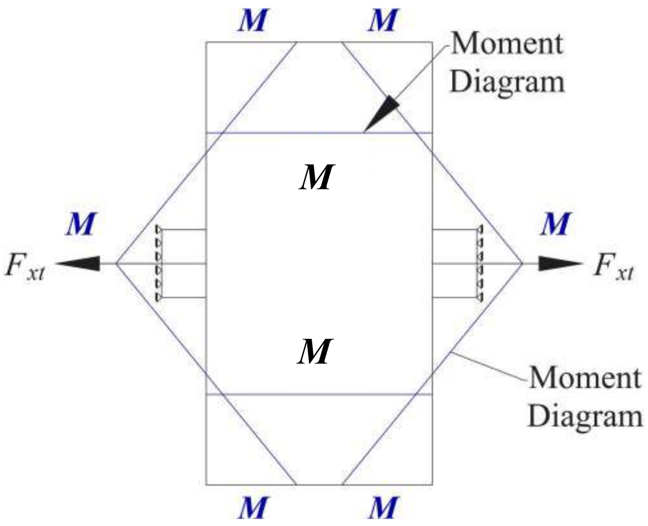

(c) Moment diagram.

Figure 3.11. One spring of spring face free body diagram and moment diagram (Reference [27]).

The equations were derived to find the yielding deformation and yielding force under tensile load for LDEPs. The bending theory to calculate the flexural stress (σ) on the LDEPs surface, as expressed in Eq. (3.1) is as follows.

$$\text{The flexural stress, } \sigma = \frac{M_f}{Z} \tag{3.1}$$

Where, M_f is the face moment, Z is the section modulus and σ is the yielding strength. The geometric property of a cross–section (X–X) measures its bending strength.

$$\text{The Section Modulus, } Z = \frac{I}{C} = \frac{\dfrac{tf^3}{12}}{\dfrac{f}{2}} = \frac{tf^2}{6} \tag{3.2}$$

However, Figure 3.11(b) & (c) is presented in the one spring free body and moment diagram, as the moment (*M*) values are assumed from both ends and loading point are equal and the face is segmented into two parts 1 and 2 as depicted in Figure 3.12. The stiffer region is excluded, while the stiffest region is removed from the structure; as demonstrated in Figure 3.12, that splits the structural faces into two regions for moment calculation. A quarter moment diagram is used; using symmetrical and equal moments, the face moments are calculated from center–to–center moment as shown in Eq. (3.3). It facilitates accurate assessment by limiting the analysis to necessary regions while simplifying calculations due to reduced diagram representation, improving accuracy without imposing realignment since structural behavior is uniformly considered across segments.

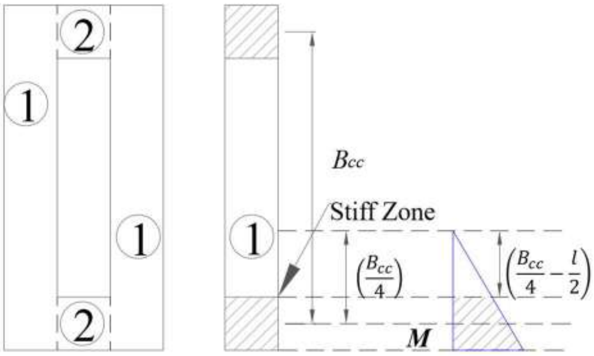

Figure 3.12. Segmentation of faces for moment analysis excluding stiff zones (Reference [27]).

$$M_f = \frac{\frac{B_{cc}}{4} - \frac{l}{2}}{\frac{B_{cc}}{4}} M = \left(\frac{B_{cc} - 2l}{B_{cc}}\right) \cdot \left(\frac{F_{xt} B_{cc}}{8}\right) \tag{3.3}$$

Where t is the thickness of the LDEPs spring, B is the length of the LDEPs springs, f is the flange thickness, l is the web thickness of the LDEPs spring and M maximum moment. Substituting Eq. (2.2) and Eq. (2.3) into the formula for yielding strength Eq. (3.1), Eq. (3.4) is obtained as follows.

$$M_f = \sigma Z$$

$$\left(\frac{B_{cc} - 2l}{B_{cc}}\right) \cdot \left(\frac{F_{xt} B_{cc}}{8}\right) = \sigma \frac{tf^2}{6}$$

$$\therefore F_{xt} = \frac{8\sigma t f^2}{6B_{cc}\left(\frac{B_{cc} - 2l}{B_{cc}}\right)} = \frac{8\sigma t f^2}{6\left(B_{cc} - 2l\right)} \tag{3.4}$$

Where F_{xt} is the yielding force. However, we do not consider the elongation deformation. We considered only bending deformation because it occurs very small deformation based on the compared to the bending deformation. The yielding displacement (U_{xt}) is determined using the area moment of inertia. The numerical equation is as follows:

$$U_{xt} = \frac{1}{EI}\left[2\left\{W_{cc}\left(\frac{F_{xt} B_{cc}}{8}\right)\frac{B_{cc}}{8}\right\} + 2\left\{\left(\frac{F_{xt} B_{cc}}{8}\right)\frac{B_{cc}}{8}\left(4\frac{1}{3}\frac{B_{cc}}{4}\right)\right\}\right]$$

$$= \frac{1}{EI}\left(\frac{F_{xt} W_{cc} B_{cc}^2}{32} + \frac{F_{xt} B_{cc}^3}{96}\right)$$

$$\therefore U_{xt} = \frac{F_{xt} B_{cc}^2}{32EI}\left(W_{cc} + \frac{B_{cc}}{3}\right) \tag{3.5}$$

Substituting the yielding force F_{xt} into Eq. (3.5).

$$U_{xt} = \frac{8\sigma t f^2}{6B_{cc}\left(\frac{B_{cc} - 2l}{B_{cc}}\right)} \cdot \frac{B_{cc}^2}{32EI} \cdot \left(W_{cc} + \frac{B_{cc}}{3}\right)$$

$$\therefore U_{xt} = \frac{\sigma B_{cc} t f^2}{24EI\left(\frac{B_{cc}-2l}{B_{cc}}\right)} \cdot \left(W_{cc} + \frac{B_{cc}}{3}\right) \tag{3.6}$$

Considering the stiffness zone and that the face is early yielding, the yielding displacement equation, Eq. (3.6) is modified as follows:

$$\therefore U_{xt} = \frac{\sigma B_{cc} t f^2}{24EI\left(\frac{B_{cc}-2l}{B_{cc}}\right)} \cdot \left(\left(\left(W_{cc} - f\right) + \frac{B_{cc}}{3}\right) \cdot \left(\frac{B_{cc}-2l}{B_{cc}}\right)^3\right)$$

$$\therefore U_{xt} = \frac{\sigma B_{cc} t f^2}{24EI} \cdot \left(\left(\left(W_{cc} - f\right) + \frac{B_{cc}}{3}\right) \cdot \left(\frac{B_{cc}-2l}{B_{cc}}\right)^2\right) \tag{3.7}$$

Where W_{cc} is the center–to–center width of the LDEPs spring web and B_{cc} is the center–to–center distance of the length of the LDEPs spring flange as shown Figure 3.11, E is the LDEPs modulus of elasticity, I is the moment of inertia of the LDEPs.

However, to validate the predictive equations for yield deformation and force in LDEBS plates, a comparison is made with results from linear and nonlinear numerical analyses, as well as experimental data. It is clearly demonstrated that the proposed Eq. (3.7) accurately predicts the combined tensile yielding load (F_{xt}) of 2.901 kN for the LDEPs (F1–1), 2.88 kN for the LDEPs (F1–2) and 6.120 kN the LDEPs (F2) in all spring. Additionally, Eq. (3.7) calculates a corresponding yielding displacement (U_{xt}) of 9.94 mm for the plate’s (F1–1), 8.83 mm for the plate’s (F1–2) and 4.09 mm for the plate’s (F2) seven springs and the Stiffness lines are shown in Figures 3.10(A)–(C). These results agree well with experimental test results even though they do not consider the thermal effects of laser cutting. As a result, this calculation is accurate only because the laser cutting has negligible thermal effects.

3.3 Under Compression Load

3.3.1 Mechanical properties of LDEBs under tensile load

The LDEBs are introduced to enable substantially larger recoverable deformations than conventional steel structural members by converting global axial deformation into flexural displacement of the slit spring segment. Existing numerical studies of thick 9 mm large deforming elastic plates under tensile loading have been able to duplicate the non-linear response using an elastic–plastic J_2 constitutive model with isotropic hardening [27]. In the present work, the steel stiffness is characterized by Young's modulus E = 205 GPa and Poisson's ratio v = 0.30. For the optimization model, a nominal yield stress of 325 MPa is assumed [77], with values of σy = 411 MPa used to confirm experimentally; plates tested showed measured yield strengths of 408 and 411 MPa from the mill certificates. While the tensile model presented in [27] is developed for LDEP devices, LDEBs employ a similar opening slit-spring premise and thus bending-dominated tensile mechanics accompanied by one spring approximation apply directly to LDEBs.

The tensile response mechanism is mainly bending dominated deformation of each individual spring segment, and almost even force distribution among the multiple springs. Finite element analysis results reported in [27] indicate that the von Mises stress is almost uniform among the seven springs, suggesting they are repeated springs working in parallel and allowing for a one-spring idealization of mechanical evaluation. As a result, the force–deformation response at the global level can be captured by considering only one representative spring and summing up the contributions of the repeated units.

Derive the predictive equations of the tensile yielding force and the tensile yielding displacement according to the bending theory based on one-spring model [27]. The flexural stress at the spring face is given by $\sigma = M_f / Z$, where M_f is the bending moment at the front of the spring section and Z is a section modulus; axial elongation was ignored because it considerably less than bending deformation in slit springs [27]. Thus, tensile yielding load and recoverable deformation capacity are essentially determined by spring geometry via its flexural rigidity and section modulus.

As far as the seismic design is concerned, LDEBs are expected to be maintained in an elastic state during severe earthquakes for which the demand story drift angle is about 1/100 and 1/50. In the case of a 45° installed large deformation elastic member, this amounts to an axial elastic deformation demand in the form of 1/140 to 1/70 of the original length [27].

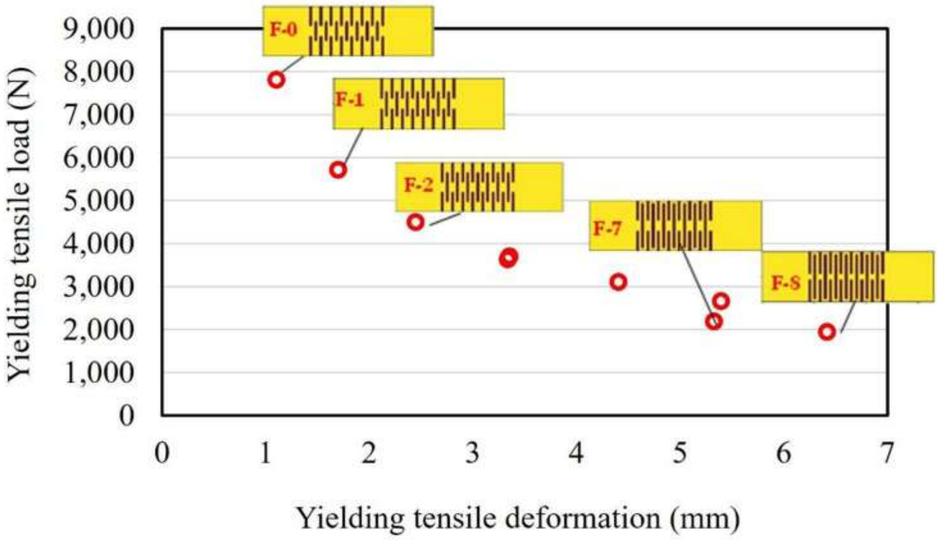

Figure 3.13. Relationship between tensile yielding deformation and tensile yielding load (2.5 mm grid elements) [77].

Therefore, a compromise between tensile deformability and strength has to be considered in the design and optimization of these devices. The multi–objective optimization solution reveals an interesting trade–off: shapes with higher tensile yielding load tend to yield less deformation, while shapes that yield more tensile stretching also have a lower tensile load requirement [77]. This relationship is illustrated in Figure 3.13 based on reanalysis results at 2.5 mm resolution [77]. In addition, since rough meshes may over predict tensile yielding load, [77] suggested reevaluating the pre-optimized fine mesh solution for final tensile properties. Figure 3.14 provides a schematic representation of how LDEBs contribute to overall system restoring force in terms of both the main–frame component and the supplementary restoring force originating from the LDEBs as a function of inter-story drift [27].

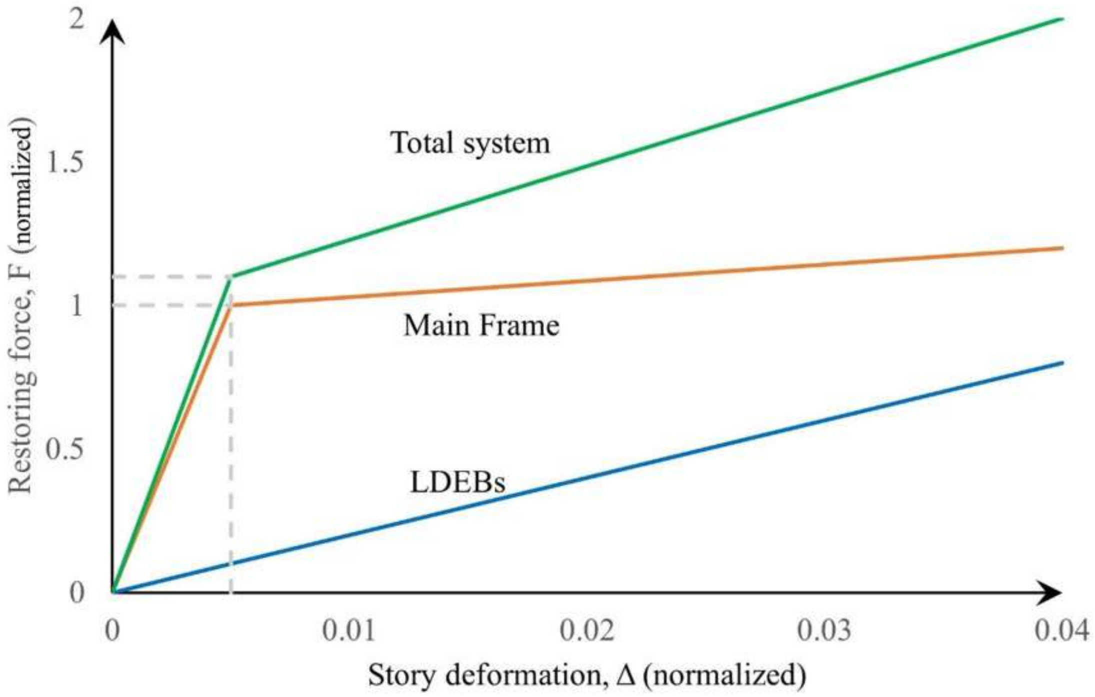

Figure 3.14. Conceptual Restoring Force–Deformation Relationship of the Main Frame with LDEBs.

Traditional seismic hysteric dampers attenuate response mainly by inelastic energy dissipation due to yielding, which could cause residual drift and might become unsterilized after a severe event. Unlike these, LDEBs are to be made nearly elastic against the target deformation range and have a strong restoring force, so even if the main-frame members suffer inelastically under a seismic load of great magnitude, it is expected that the elastic recovery of LDEBs will suppress residual deformation and relieve repair demand after earthquake [27]. These features lead to consideration of LDEBs in the context of elastic limit capacity and stability considerations, not maximizing plastic energy dissipation as with yielding devices.

3.3.2 Behavioral characteristics

Traditional seismic hysteresis dampers generally reduce response by early energy dissipation and depend on the main structure for elastic restoring force [45, 78, 79]. Although widely effective as energy dissipation tools, if it is intended that increasing damper rigidity to achieve a high vibration control effect tends to shorten the natural period, and their behavior is largely controlled by energy dissipation mechanisms. LDEBs, on the other hand, are engineered as a completely different type of responsive material. They have much higher elastic limits than the main frame and are capable of elastic recovery even when the main structure is plastically deformed. If LDEBs are adopted as supplementary braces, their initial stiffness contribution is usually less than of the stiff-dominated hysteretic dampers; therefore, a large variation in the fundamental period should not be observed. Conversely, the smaller increase in stiffness can result in slightly larger peak displacements (story drifts) for the same level of lateral excitation. Moreover, due to their strong residual response mitigation capacity with a combined stiffness and enhanced elastic deforming capacity when being well designed, the LDEBs can be extremely effective in improving the seismic performance of structural systems [80].

3.3.3 Applications and design considerations

LDEBs have broad application prospects such as braces, knee braces, stiffened plate, and steel plate walls [63]. Figure 3.15 shows representative application ideas and installation locations into a frame (brace, knee-brace at the beam–column joint area, plate type link/connector and replaceable panel in steel plate wall). It is also worth mentioning that optimized geometries gotten by topology optimization were reported in previous works [27, 66].

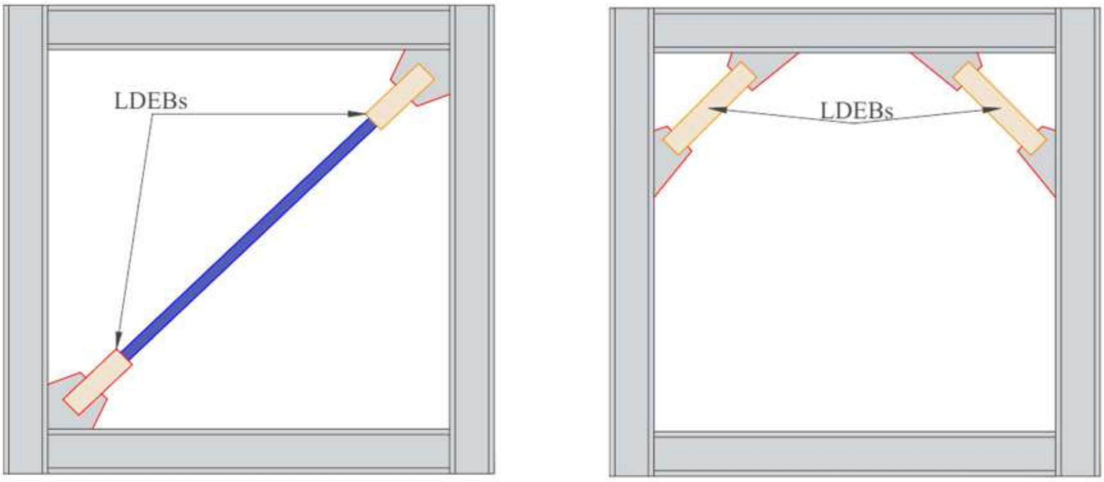

(a). Diagonal Braces (LDEBs)

(b). Knee Braces (LDEBs)

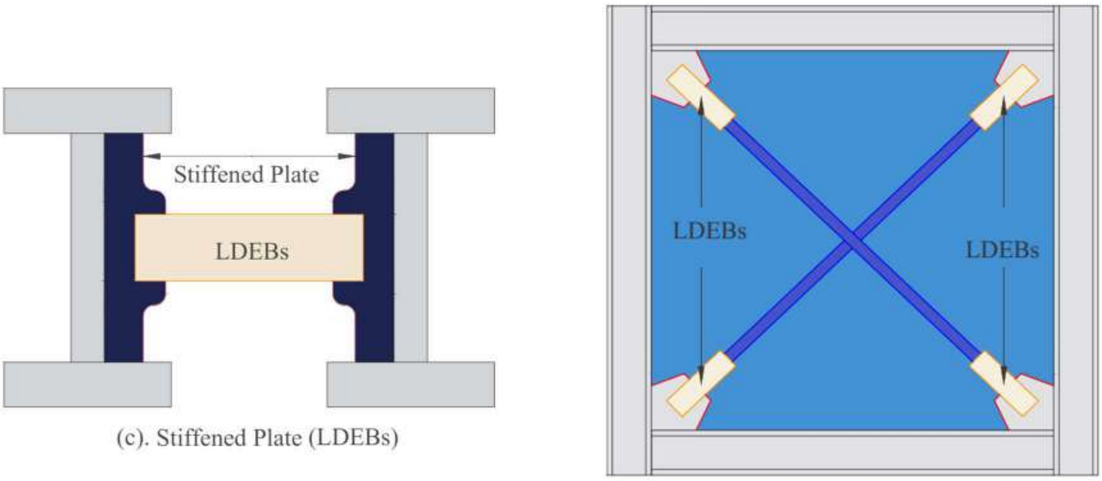

(c). Stiffened Plate (LDEBs)

(d). Steel Plate Wall (LDEBs)

Figure 3.15. Conceptual application examples of Large Deformable Elastic Braces in steel structures: a) diagonal braces; b) knee braces; c) stiffened plate; d) steel plate walls components.

For practical considerations, to achieve proper performance LDEBs should be designed: i) to ensure an elastic restoring force can be reached without increasing the global lateral stiffness excessively, ii) to ensure that the braces demand remain recoverable during the design earthquake and iii) to confine the buckling prevention requirement under compression loading. Due to sensitivity of buckling resistance to brace–to–frame end restraints, connection detailing needs to be accounted for in the assumed boundary condition used for assessment. In this study, the focus is on 660 mm × 200 mm × 9 mm SM490A steel plates of of 408 MPa and 411 MPa yield strength, which is with 3.3 aspect ratios, a practical aspect ratio in the case of slit–type knee braces in which the mutual effect of yielding and buckling cannot ignore.

3.3.4 Methodology

This study consists of three stages: (1) FEM linear buckling analysis from which elastic buckling load can be obtained, (2) formulation of elastic buckling load with torsional energy considerations, and (3) experimental verification for preventions of buckling.

3.3.4.1 *FEM linear buckling analysis*

Finite element analyses were performed by using LISA 8.0 [71] to assess the buckling behavior of Large Deformable Elastic Braces. We analyzed the F1–1, F1–2, & F2 plates specimens and the plates were meshed with shell elements (QUAD4) with base mesh degree of freedom 66×20 (10 mm cell size) and refined mesh degree of freedom 132×40 for the convergence study. Figure 3.16 shows specific dimensions of each sample. The three samples have the same size of outer plate and arm design domain geometry, but a different slit/cut configuration within the design domain between models. The material properties are the same as section 2.1. The boundary condition Fix30 was applied, where the left end was completely fixed and the right end was fixed except in the compression direction, in which 30 mm long end zones were completely fixed to emulate partial end restraint. Fix30 is used as an illustrative form of finite-end restraint created from practical brace-connection regions and the experimental end fixtures in this study, meaning it is used as a typical partially restrained boundary condition to test for sensitivity. The displacement fields, the distribution of the von Mises stress and the shapes of the first eigenmodes resulting from the three specimens are shown in Figure 3.17–3.19. The corresponding yield and buckling results for the three specimens are listed in Table 3.5. The compressive yield load P_y is determined as the load corresponding to first yielding, when the maximum von Mises stress in the design domain attains the measured yield stress of the steel (408–411 MPa). Since pre-yield behavior can be described as linear-elastic, P_y was calculated by scaling a reference linear-static analysis with $F_{xc} = 1$ kN. Here, F_{xc} is the applied compressive load; σ_y is the plates yielding stress; σ_v is the plate meses response stress; $\Delta_x$is the plate linear yielding displacements; and λ_{cr} is the buckling load factor. Loading was applied as the load was $F_{xc} \times \sigma_y/\sigma_v$ instead of 1kN, and the buckling load was calculated as $P_{cr} = \lambda_{cr} \times$ applied load. The later theoretical expression in Section 3.2 is expressed in terms of the torsional strained energy defined with the eigenmode and work-energy equation based on Clapeyron's theorem.

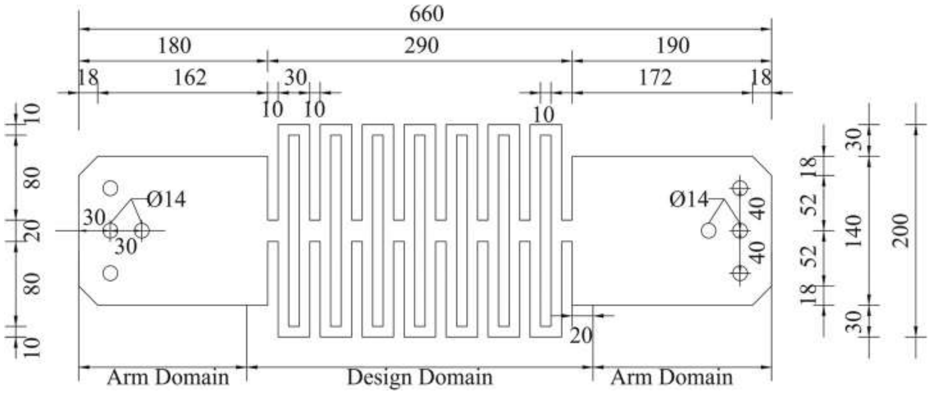

(a) F1-1

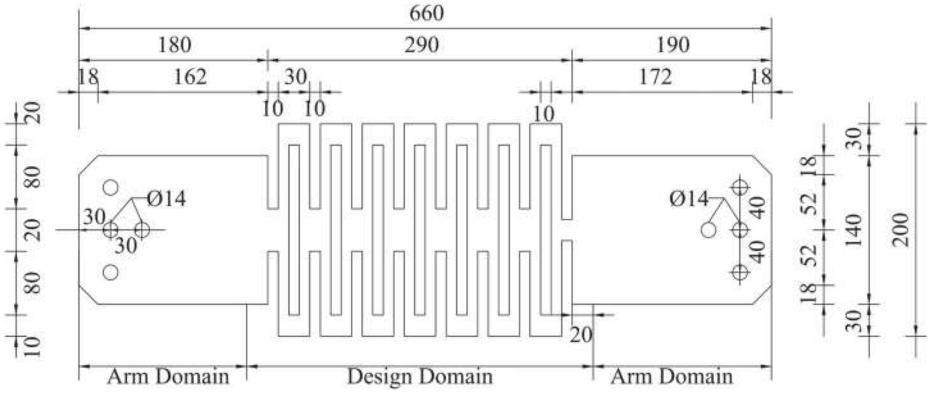

(b) F1-2

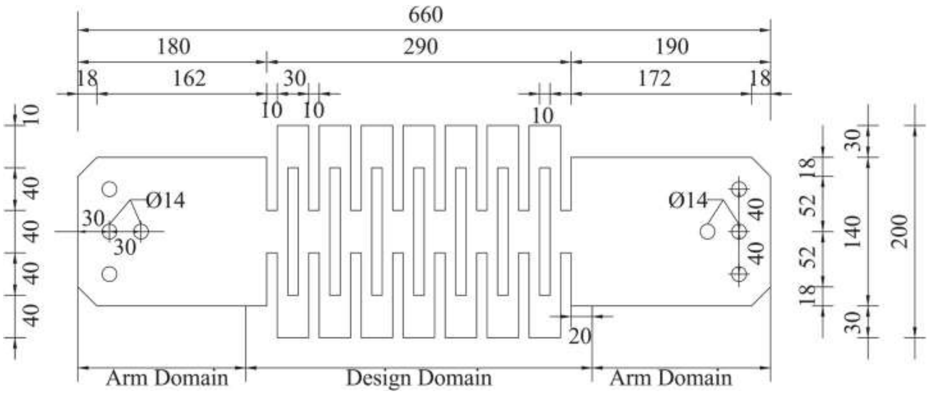

(c) F2

Figure 3.16. Geometry and dimensions of plate specimens: (a) F1-1; (b) F1-2; & (c) F2. (Units: mm.)

Table 3.5. Comparison of Yielding and Buckling Behavior under Applied Load, F_{xc} = 1.0 kN.

Specimen / Plates	Yielding Displacement $\left(\frac{\Delta_x \sigma_y}{\sigma_v}\right)$	Mises Response Stress (σ_v)	Yielding load $\left(\frac{F_{xc}\sigma_y}{\sigma_v}\right)$	Buckling Load $(\lambda_{cr} \times F_{xc})$
Unit	mm	MPa	N	kN
F1–1	9.25	410.90	3,145	16.83
F1–2	6.70	408.00	5276	23.48
F2	3.81	408.00	7849	33.55

Table 3.5 shows a stiffness hierarchy that the yielding displacement decreases from 9.25 mm to 3.81 mm, with the yield load known as 3.145 kN to be7.849 kN and the eigenvalue buckling load increases from16.83 kN to 33.55 kN of F1–1, F1–2 & F2. This gain of buckling resistance matches the twist/torsion dominated first eigenmode encountered in Figure 3.18 and discussed in post section 3.3.4.2, since cut-patterns govern the effective torsional stiffness of the deformable region and prevent out–of–plane twisting due to torsion domination. Thus, a higher effective torsional stiffness of the tube in more continuous models implies that they have also larger critical buckling loads.

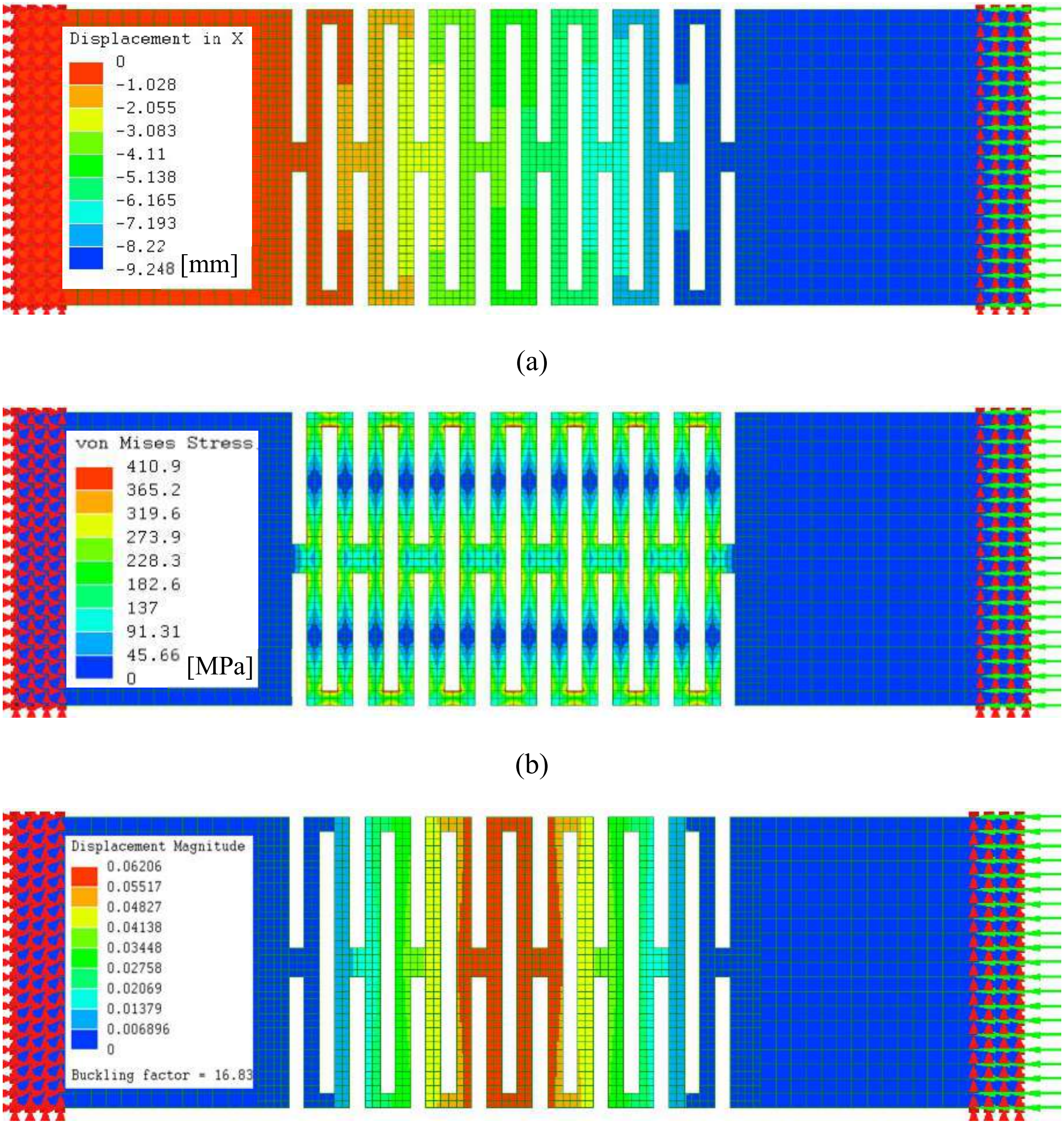

(a)

(b)

(c)

Figure 3.17. F1–1 Specimen finite element analysis results for structural response of perforated plate with with 30 mm fixed boundary conditions under 1000 N applied load: (a) displacement (mm) field in *x*–direction, (b) von Mises stress (MPa) distribution, and (c) first eigenmode buckling configuration is 16.83 kN.

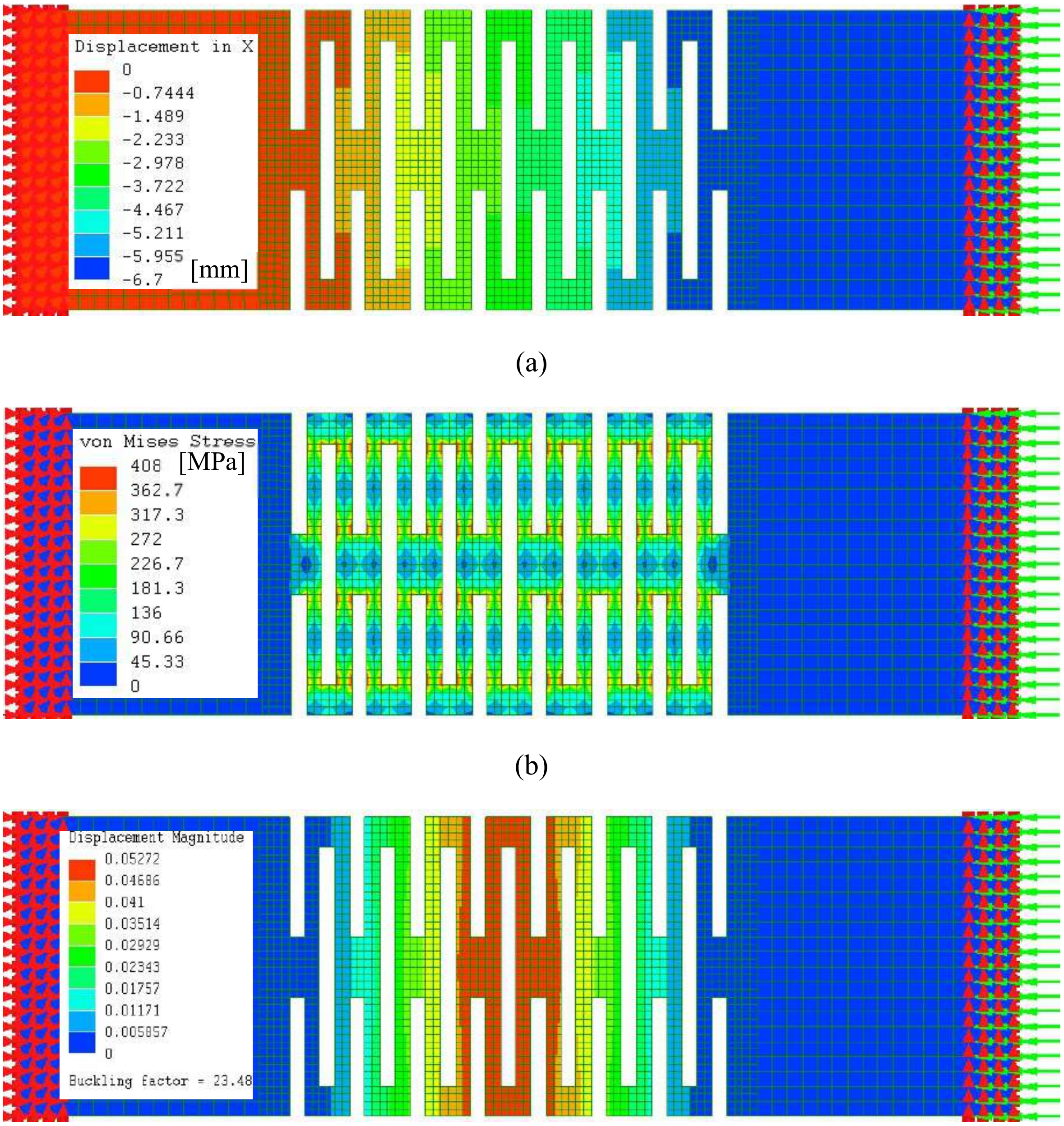

(a)

(b)

(c)

Figure 3.18. F1–2 Specimen finite element analysis results for structural response of perforated plate with 30 mm fixed boundary conditions under 1000 N applied load: (a) displacement (mm) field in *x*–direction, (b) von Mises stress (MPa) distribution, and (c) first eigenmode buckling configuration is 23.48 kN.

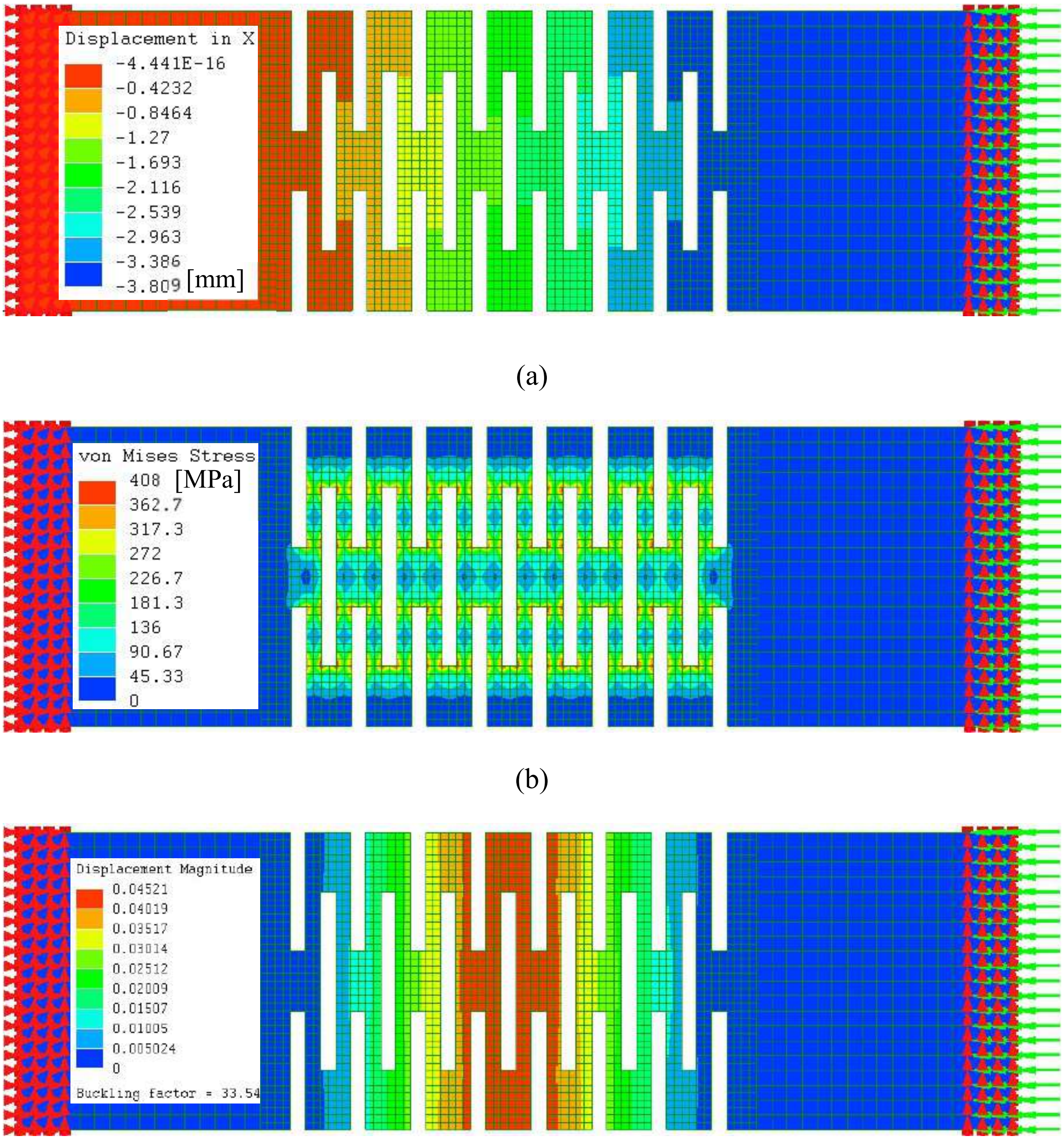

(a)

(b)

(c)

Figure 3.19. F2 Specimen finite element analysis results for structural response of perforated plate with 30 mm fixed boundary conditions under 1000 N applied load: (a) displacement (mm) field in *x*–direction, (b) von Mises stress (MPa) distribution, and (c) first eigenmode buckling configuration is 33.55 kN.

3.3.4.2 *Energy–based formulation for critical buckling load determination*

Torsion Energy Formulation: According to the FEM linear buckling deformation behaviors shown in Figure 3.20, we neglect other strains and only consider the torsional strain energy (U_T) due to twist deflection in this study. The red circle in Figure 3.20 (c) shows the representative plate strip selected to obtain the torsional strain energy. The tensile energy of torsional strain integrated over the torsion–effective length (L_T) is given by the work-conjugate relation between the applied torque (M_T) and twist rate $d\varphi/dx$:

$$U_T = \int_0^{L_T} \frac{1}{2} M_T \left(\frac{d\varphi}{dx} \right) dx \tag{3.8}$$

In the above expression, $x = 0$ represents the beginning of the torsion-active region and L_T is its end according to the FEM eigenmode where torsional rotation contributions become negligible. The applied torque $M_T = GJ_c \left(d\varphi / dx \right)$ where G is the shear modulus and J_c is the Saint–Venant torsional constant of effective section as illustrated in Figure 3.20 (c). Substituting this relation into Eq. (3.8) and employing the FEM-based assumption that the rate of twist is nearly constant over $0 \leq x \leq L_T$ give rise to the analytical torsional strain energy equation:

$$U_T = GJ_c L_T \sum_{i=1}^{n} \left(\frac{d\varphi_i}{dx} \right)^2 \tag{3.9}$$

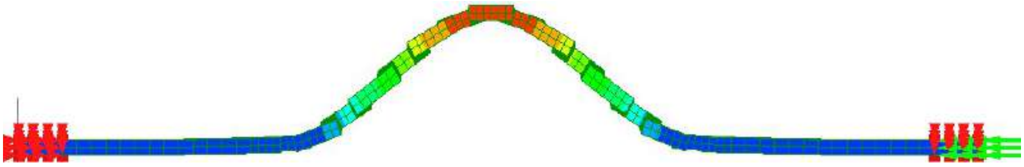

(a)

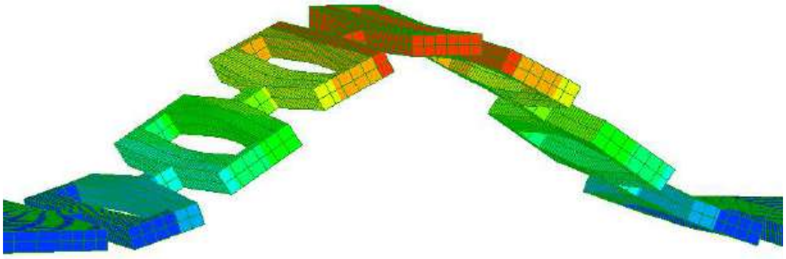

(b)

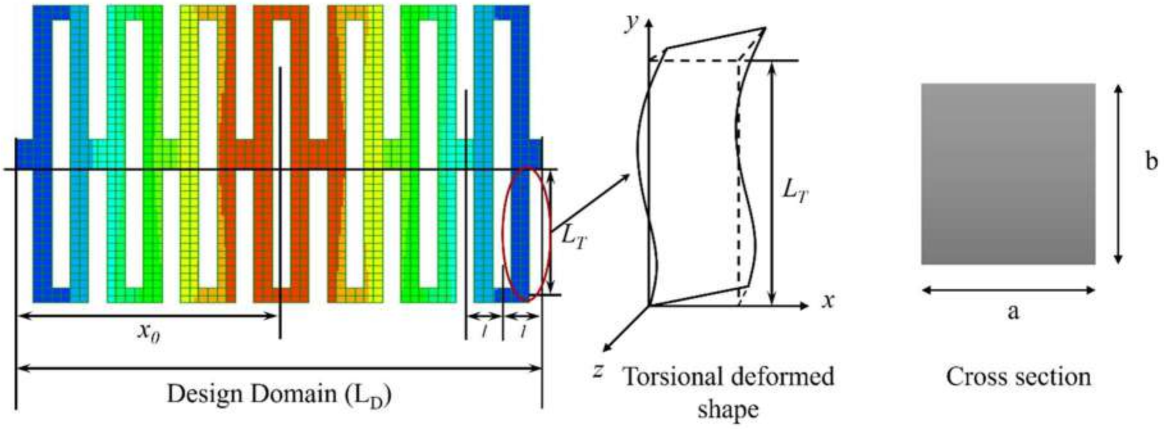

(c)

Figure 3.20. Elastic buckling mode shapes from finite element analysis: (a) full plate buckling deformation under compressive loading; (b) magnified deformation gradient; (c) Definition of the torsion effective length and cross section parameters for cross section's modelling of the torsional deformation.

Calculation of Tortional Angles: The origin of the x–axis is taken at the end of the left arm domain of the plate, and the buckling waveform function in Figure 3.21 is assumed as follows:

$$Z(x) = \frac{Z_0}{2}\left[1+\cos\left(\frac{2\pi}{L_D}(x-x_0)\right)\right] \tag{3.10}$$

Here, $Z_0$is the maximum out-of-plane displacement; x is the longitudinal coordinate along the plate axis measured from the defined origin; x_0 is the coordinate of the plate center; and $L_D$is the length of the design domain of the plate. By applying the second differentiation to Eq. (3.10), the curvature of the deformation curve is obtained, which corresponds to the rate of change of the torsional angle along the plate axis. Hence, the torsion angle distribution can be expressed as:

$$\varphi(x) = \frac{d^2z}{dx^2} = -\frac{2\pi^2 Z_0}{L_D^2}\left[\cos\left(\frac{2\pi}{L_D}(x-x_0)\right)\right] \tag{3.11}$$

Considering the local torsional deformation of each discretized segment of the plate, the incremental twist angle over the segment length can be related to the curvature of the deformation function $Z(x)$. Accordingly, the relationship between the normalized torsion angle and the curvature distribution can be written as:

$$\frac{\Delta\varphi}{L_T} = \frac{l}{L_T}\frac{dZ^2(x)}{dx^2} \tag{3.12}$$

Squaring Eq. (3.11) and substituting Eq. (3.12), the normalized element torsion becomes:

$$\therefore \left(\frac{\Delta\varphi}{L_T}\right)^2 = \left(\frac{l}{L_T}\right)^2 \left(\frac{2\pi^2 Z_0}{L_D^2}\right)^2 \left[\cos^2\left(\frac{2\pi}{L_D}(x - x_0)\right)\right] \tag{3.13}$$

Evaluating Eq. (3.13) at the representative point of the i–th segment, the normalized torsion for element i becomes:

$$\therefore \left(\frac{\Delta\varphi_i}{L_T}\right)^2 = \left(\frac{l}{L_T}\right)^2 \left(\frac{2\pi^2 Z_0}{L_D^2}\right)^2 \left[\cos^2\left(\frac{2\pi}{L_D}(x_i - x_0)\right)\right] \tag{3.14}$$

The mode of deformation utilized in these calculations corresponded to the first buckling mode vector provided by FEM eigenvalue analysis. The resultant torsional curvature was subsequently computed post-processing the eigenvector data using the discretized domain; Figure 3.17 is meant exclusively for visualizing the eigenmode. The figure illustrates the elastic buckling mode shapes, confirming the validity of the assumed torsion–angle distribution along the plate axis and the correlation with theoretical expressions.

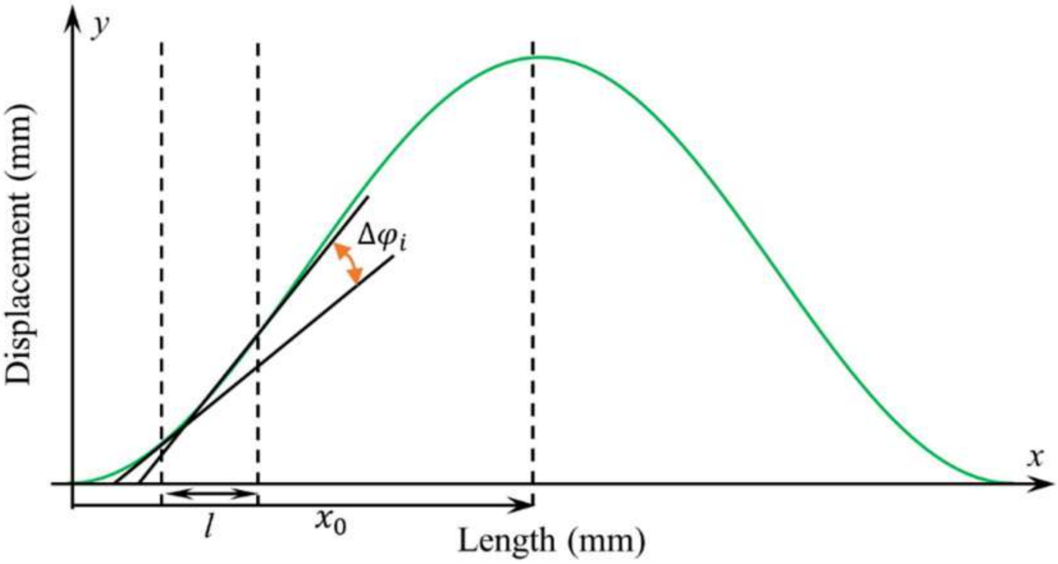

Figure 3.21. Assumed displacement (buckling) shape functions along the member length for energy formulation.

Work –Energy Balance: Compressive axial work is done by the out-of-plane buckling mode end-shortening (*Δl*) at the start of elastic buckling. With proportional loading and a linear elastic system, the balance for generalized work of external loads and internal torsional strains energy (U_T) follows from Clapeyron's theorem in form:

$$W = P_{cr}\Delta l = U_T \tag{3.15}$$

Here, *Δl* represents the geometric shortening associated with the buckled centerline and is evaluated (small-slope assumption) as

$$\Delta l = \frac{1}{2}\int_0^{L_D}\left(\frac{dz}{dx}\right)^2 dx$$

For the assumed first-mode shape $z(x)=Z_0\sin(\pi x/L_D)$,

$$\Delta l = \frac{\pi^2 Z_0}{4L_D} \tag{3.16}$$

Substituting Eq. (3.9), Eq. (3.14) and Eq. (3.16) into the Eq. (3.15):

$$P_{cr} = \frac{U_T}{\Delta l} = \frac{1}{\dfrac{\pi^2 Z_0}{4L_D}}\cdot GJ_c L_D \sum_{i=1}^{n}\left(\frac{\Delta\varphi_i}{L_T}\right)^2$$

$$\therefore P_{cr} = \frac{4GJ_c L_D^{\,2}}{\pi^2 Z_0}\cdot\sum_{i=1}^{n}\left(\frac{\Delta\varphi_i}{L_T}\right)^2 \tag{3.17}$$

This closed form links the buckling load directly to material properties, geometric stiffness, and the deformation mode shape. For thin rectangular sections (a × b), J_c is determined by the standard St. Venant torsional approximation:

$$J_c = \frac{1}{3}a^3 b\left(1-\frac{192a}{\pi^5 b}\sum_{n=1,3,5....}\frac{1}{n^5}\tanh\frac{n\pi b}{2a}\right)$$

The twisting deformation pattern providing the physical basis for this energy formulation is illustrated in Figure 8, showing the eigenmode configuration of the LDEB under compression, confirming consistency between analytical and FEM–based results.

3.3.4.3 *Experimental methodology*

Experimental tests were conducted on Large Deformable Elastic Brace (LDEB) plates fabricated from JIS G 3106 SM490A steel using laser cutting. Figure 3.22 shows the specimen geometry with dimensions of 660 mm × 200 mm × 9 mm and the characteristic slit pattern designed for enhanced elastic deformation capacity. The specimens had a yield strength of 408–411MPa as verified by mill certificates. Prior to testing, the gripping portions were treated with blasting to prevent slippage during loading.

The test setup utilized a universal testing machine with 1000 kN capacity at Shimane University's Structural Testing Laboratory show in Photo 3.4. For compression tests, specimens (F3) were directly gripped by the machine jaws with 40 mm grip length at each end. L–shaped steel angles were attached to specimen ends for compression tests, with bolted connections at two locations to prevent rotations during loading. The boundary conditions were defined as the left end fixed in all directions and the right end only restrained in the transversal directions to allow the axial displacement.

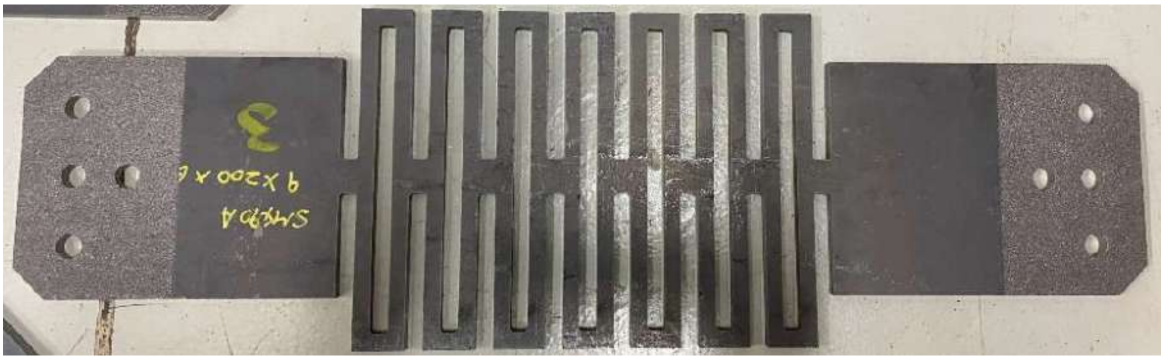

(a)

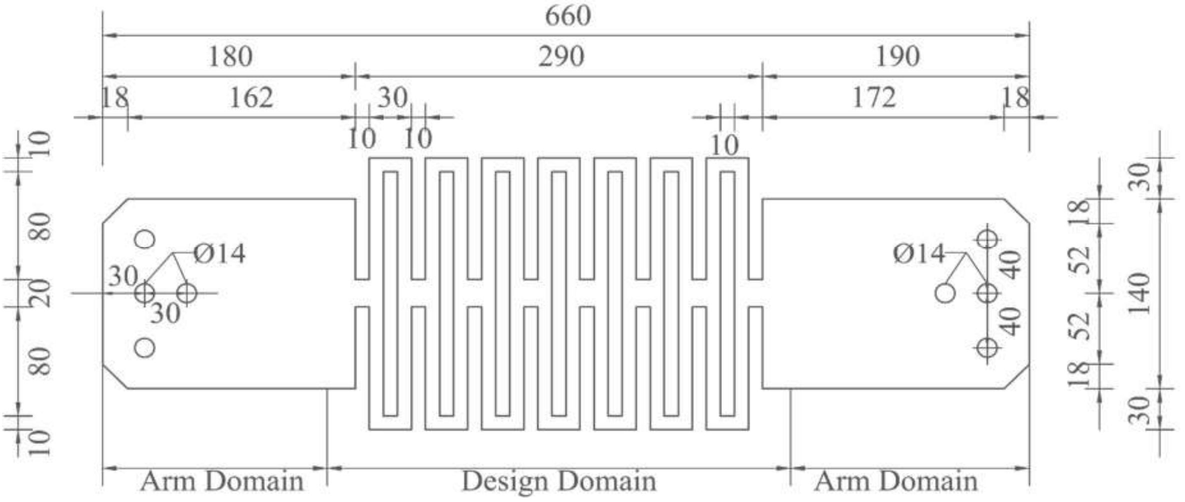

(b)

Figure 3.22. LDEB specimen (F3) geometry and dimensions showing (a) overall dimensions 660 mm × 200 mm × 9 mm, (b) detailed slit pattern with 290 mm design domain and 370 mm arm regions (all units are mm).

Displacement measurements were performed using two magnetic–adhesive displacement transducers, which were mounted on the front and back surfaces of the specimen. The transducers met wooden reference blocks fixed to the specimen with L–shaped members and clamps, allowing for homogeneous measurement during the tests. Prior to loading, specimen alignment was verified using a level to ensure perpendicularity to the loading axis.

The loading protocol employed displacement–controlled loading at 0.50 mm/min for compression tests. Testing proceeded continuously through the elastic range, yielding point, and into the plastic deformation regime with data acquisition. When the displacement transducers reached their 50 mm measurement limit, the test was paused, sensors were removed, and loading resumed until either specimen failure occurred in tension or internal contact occurred in compression, or the testing machine's 1000 kN capacity was reached. To check the repeatability of the tests, a single identical specimen (F3) was tested for each loading condition and the final shape of specimen F3 is shown in photo 3.5 after compression test.

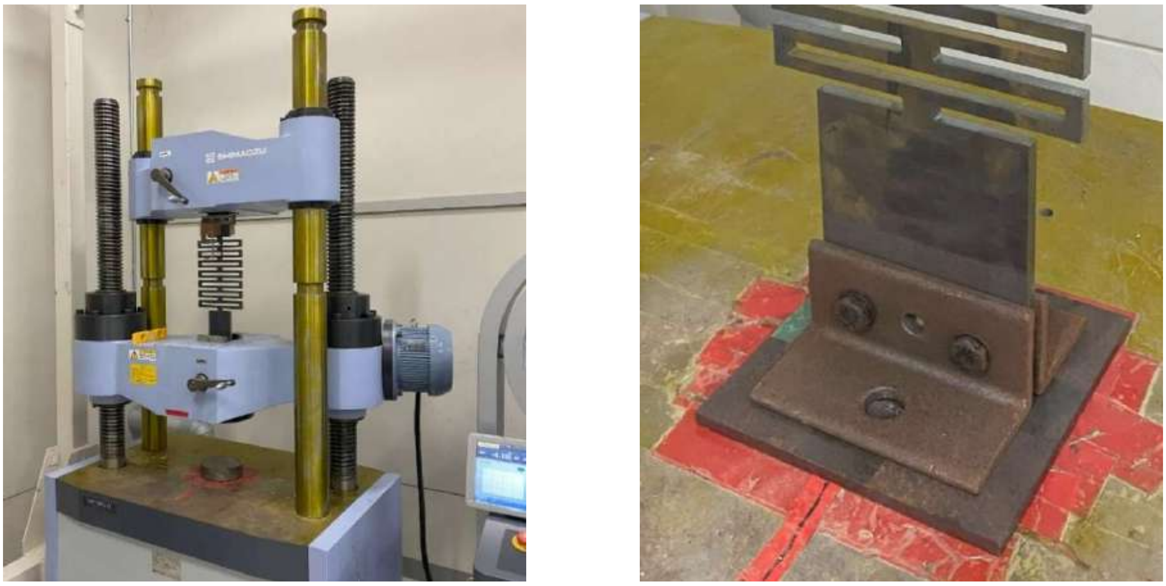

(a) (b)

Photo 3.4. F1-1 Experimental test setup showing (a) universal testing machine overview, (b) compression test configuration with L–shaped steel angles and bolt connections.

Photo 3.5. F1-1 Model after compression experimental tests.

3.3.5 Results and discussion

The eigenvalue analysis using FEM revealed the primary instability mode in compression of perforated steel plates. The FEM buckling loads of specimen F1–1, sample F1–2 and specimen F2 were 16.83 kN, 23.48 kN and 33.55kN, respectively (Table 3.5). The enhanced buckling strength from F1-1 to F2 signifies that a more continuous cutting pattern mobilizes greater effective torsional stiffness in the design space with the same 30 mm end-restraint. Due to the end restraints sensitivity of stability against buckling, partial-end-restraint condition (Fix30) was chosen as it would be used to simulate the experimental end brace connection region. For this common boundary condition, variation in the buckling load levels among specimens appear to depend primarily on the configuration of the cut.

The energy–formulation problem formulated in section 3.3.4.2 was used to predict the elastic buckling in a theoretical manner. Based on the principle of torsional strain energy method and the approach to work–energy balance (Eq. 3.8–3.17), theoretical critical buckling loads were determined, taking torsional patterns deformation obtained in FEM analysis. Table 3.6 from the energy approach, elastic buckling loads of 19.52 kN, 26.00 kN, and 39.00 kN were obtained for specimens F1–1, F1–2 and F2 respectively. Table 3.6 compares the present energy-based estimate with the FEM eigenvalue buckling loads tabulated for three representative geometries. Energy approach yields P_{cr} values which are on average 11–16% greater than FEM (ratio P_{cr}/ P_{FEM} = 1.11–1.16) suggesting a mild conservatism for these cases. This is to be considered as an initial validation and a broader comparison through further geometries and restraint conditions are needed. The higher value of the buckling strength for longer restrained length (F1– 1, F1– 2 & F2) indicates that substantial torsional stiffness is mobilized within 30 mm of supports. The assumed curve for buckling deformation is completely accounted for within this approach in terms of the torsional constant and twist angle distribution $\varphi(x)$, confirming the deformation mode which was guessed in Eq. (3.10). The corresponding yielding load of 3.145 kN (both determined by FEM and by classical yield theory) is although clearly below all critical buckling loads. Therefore, the corresponding instability in all three cases is that of the yield before buckling design philosophy.

Table 3.6. Comparison of FEM, and theoretical elastic buckling Results.

Specimen	Theoretical Buckling Load (kN)	FEM Buckling Load (kN)	Ratio (Pcr/ PFEM)
F1–1	19.52	16.83	1.16
F1–2	26.00	23.48	1.11
F2	39.00	33.55	1.16

*No buckling observed; minimum values based on maximum test load

Compression tests showed the anticipated yielding behavior. The test specimen (F3) failed at 3.0 kN and 11 mm (Figure 3.23). The experimental result shows a good agreement with the FEM prediction (3.145 kN) and is slightly lower by about 5%. The load plateau, at an applied load ranging from 5.2 to 5.8 kN shows that the rate of plastic flow is constant with a lack of buckling, as this was predicted in the design hypothesis that yielding should appear always before the appearance of stability to buckling.

One difficulty with complete validation is that the tested specimen effectively experienced at an ultimate load of 5.90 kN, but without visibly buckling, which undermines any direct comparison to the critical buckling load. Instead, the buckling resistance was indirectly characterized by the absence of instability up to failure, which proved the effectiveness of the anti–buckling design strategy. Both the FEM predictions and energy–based theoretical results are much higher than the experimental ultimate load (2.85–5.68, 3.31–6.61 times larger, respectively), indicating that buckling was effectively prevented throughout the entire loading progression.

The comparison results in Table 3.6 show that both the FEM and energy–based theoretical elastic buckling loads are significantly higher than the yield load and experimentally determined at a ultimate load, which confirms the success of the proposed design philosophy. The energy–based model provides a useful design tool for designers and has been proven to yield conservative prediction results, taking torsional deformation effects into consideration, while avoiding the use of FEM. The lack of direct evidence of buckling is nevertheless a limitation, and future validation could include measurements with lateral displacement and different experimental designs, where the onset of buckling can be observed more clearly if it occurs at higher loads.

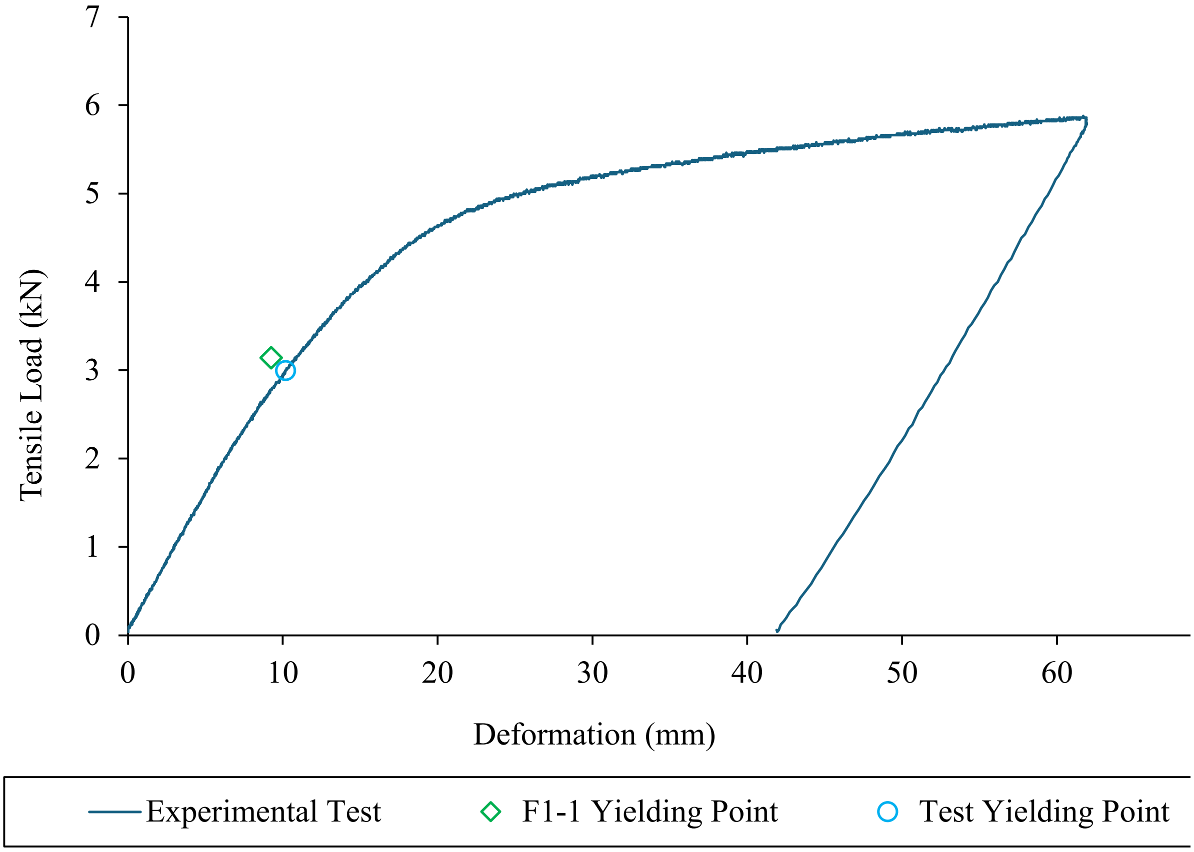

Figure 3.23. F3 Specimen load–deformation response of 660 mm × 200 mm × 9mm SM490A LDEB specimen under compression loading showing experimental yield at 3.00 kN compared to analytical prediction of 3.145 kN.

3.4 Conclusions

This research contributes to a fundamental knowledge and behavior of LDEPs/LDEBs under tensile loading and compressive loading, an essential precursor for their implementation in seismic–resisting structural systems. The general picture of numerical, theoretical and experimental investigation for the two loading states is summarized as follows:

1. **Validated tensile design tools:** Predictive formulas for tensile yielding load and deformation were derived, which well corresponded to the experiment and nonlinear FEM, providing simple heuristic equations for initial sizing and engineering level calculations. Points evaluated from a Von Mises yield condition and linear FEM are conservative for safety, while residual stress due to laser cutting causes slighter earlier yielding and post–yield hardening increases load carrying capacity, both effects which must be explicitly catered for in design and testing regimes.
2. **Buckling prevention by design–induced yielding:** Under compression, three approaches (FEM eigenvalue analysis, energy–based torsional formulation, and experiments) consistently show that LDEBs can also be designed so that yielding always occurs before any elastic buckling. The energy approach provides conservative critical buckling predictions about 11–16% higher than FEM eigenvalues whilst both analytical methods exceed the experimental ultimate load by factors of around 2.85–6.61, demonstrating that buckling was effectively mitigated during loading.
3. **Sensitivity to Connection Detailing and Geometric Configuration:** Buckling capacity for representative specimens (F1–1, F1–2, & F2) increased by about 40–100% with the Fix30 end–restraint configuration, underscoring that restraint length, slit geometry, and local stiffness distribution near the ends are decisive levers for design.

4. **Design implications for seismic resilience:** The tensile and compression results collectively support LDEBs/LDEPs as elastic, re–usable members which are high reversible deformational capable, and they offer restore force that could be used for reducing residual drift after strong motion. The tensile formulas permit simple capacity checks, the energy–based buckling model serves as a quick conservative screen without labor–intensive FEM, and plain linear FEM is still useful for initial stiffness and lower–bound yield checks.
5. **Engineering Implications and Future Directions:**
    - Introduce measured residual stress/hardening parameters of laser–cut plates into nonlinear material models to minimize the scatter of yield point.
    - Make connection detailing standard in a design guide to consistently maintain $P_{cr} > Py$.
    - Extending experimental techniques to instrument lateral out–of–plane responses, so that any delayed onset of buckling could be observed directly and compared with theory.
    - Prepare simple selection diagrams (axial stiffness vs elastic limit vs end–restraint) based on the verified equations to assist with story–drift targets in 1/100–1/50 range for practical building designs.

This study has shown effectively that LDEBs are a promising technological innovation for the seismic reduction which can exhibit reasonable tensile and compressive performance. The combined analytical, numerical, and experimental approaches used here build a strong basis for their safe use in earthquake–resistant structural design by addressing the fundamental problem of reducing residual displacements with simultaneous avoiding loss of the safety criteria in seismic loads.

CHAPTER 4: OPTIMIZATION OF LARGE DEFORMABLE ELASTIC BRACES IN TWO–DEGREES–OF–FREEDOM SYSTEMS

4.1. Introduction

Current Japanese earthquake resistance standards permit building structures to be damaged during large earthquakes while protecting human life. However, there is an increasing demand for structural members to reduce damage and maintain the value of their properties, even in large earthquakes. Due to this background, various seismic response control technologies [46–48, 81] have been implemented in the last decades, including optimization–based approaches for stiffness and damping distribution [82–84]. Metallic–yielding dampers [50, 65] are widely used in Japanese buildings and are generally intended to dissipate seismic energy before the material of the main frame yields or buckles. While they allow the main frame to remain elastic under major earthquakes, this assumption may not be effective for severe motions beyond the design level [53, 85]. Consequently, large residual deformation may occur, disrupting the continuous usability of buildings.

The LDEBs proposed by Sawada are processed steel plates with special shapes that have a larger elastic limit than normal braces due to their flexible performance. In structures with LDEBs, the elastic restoring force works until LDEBs yield; therefore, the structure obtains additional post–yielding stiffness even when the main frame members yield. Past research conducted monotonic tension loading experiments on LDEBs to verify their elastic yielding deformation, and seismic response analysis frameworks clarified their effectiveness [26].

However, two key research gaps remain unaddressed. First, while metaheuristic optimization techniques have been widely applied to conventional dampers and bracing systems, limited attention has been given to optimizing the stiffness distribution of LDEBs. Second, prior studies often relied solely on optimization algorithms without systematically validating global optimality across broad seismic scenarios.

To fill this gap, this work presents a new hybrid optimization framework that integrates particle swarm optimization (PSO) with Round Robin response surface analysis. This dual approach identifies globally optimal stiffness configurations for LDEBs in multi–degree–of–freedom (MDOF) systems and verifies the solutions' robustness under different seismic inputs. The importance of these studies is their applicability worldwide and the validation of their results via experimental work, formally establishing the leading–edge technology for the robust optimization of LDEBs that can be applied with confidence to enhance the seismic safety of structural buildings. Recent studies have optimized dampers and braces using metaheuristic algorithms [86–88], but the optimum stiffness distributions of LDEBs in multi–story buildings are still unknown. Previous research [27] confirmed the elastic limit and post–yielding performance of large deformable elastic plates (LDEPs), validating their potential in seismic mitigation. This study advances the practical use of LDEBs by optimizing their stiffness distribution in two–story structural models.

While PSO has been applied to optimize damper placement and stiffness in seismic design, limited attention has been given to the unique behavior of LDEBs, whose highly nonlinear elastic characteristics require careful optimization. The interaction between MDOF systems and the variable stiffness levels of LDEBs has not been systematically explored. This study introduces a hybrid framework combining PSO and Round Robin response surface analyses. PSO enables efficient global search, while Round Robin analysis validates the results through comprehensive response surface mapping, enhancing reliability in capturing global optima and structural performance trends across varying seismic intensities. This combination ensures robust, optimized stiffness configurations across different seismic scenarios.

This study aimed to obtain the optimum stiffness distribution of LDEBs in MDOF systems as useful knowledge for structural designs. This study considered two–degrees–of–freedom (2–DOF) systems that represented two–story buildings as the first stage of this research. First, the optimization problem that finds the optimum stiffness of LDEBs was formulated and solved using the PSO method, which has been successfully applied in seismic design optimization [89, 90]. Next, a Round Robin analysis of 2–DOF models with a wide range of secondary stiffness ratios subjected to three different earthquake types was carried out. Through comparison, the PSO solution corresponded to the global optimum identified via Round Robin analysis.

4.2. Target Models

This study demonstrated the performance of 2–DOF systems, as shown in Figure 4.1. K_{fi} and K_{bi} denote the stiffness of the main frame and LDEBs in the ith story, respectively. Therefore, the ith overall stiffness (K_i) and stiffness ratio (α_i) of the LDEBs against the main frame can be expressed as:

$$K_i = K_{fi} + K_{bi} \tag{4.1}$$

$$\alpha_i = K_{bi} / K_{fi} \tag{4.2}$$

The damping coefficient of the ith story's dashpot C_i was assumed to be proportional to K_i. The mechanical properties of each story are shown in Table 4.1. The yield shear force in each story was calculated from the required strength against the level 2 seismic force specified by the Building Center of Japan (BCJ) code [91].

Table 4.1. Mechanical properties for two–story main frames.

Data	1st Story	2nd Story
Weight, W	1000 kN	1000 kN
Yielding story shear force, Q_{yi}	600 kN	378 kN
Yielding deformation, δ_{yi}	2 cm	2 cm
Story stiffness, K_{fi}	300 kN/cm	189 kN/cm

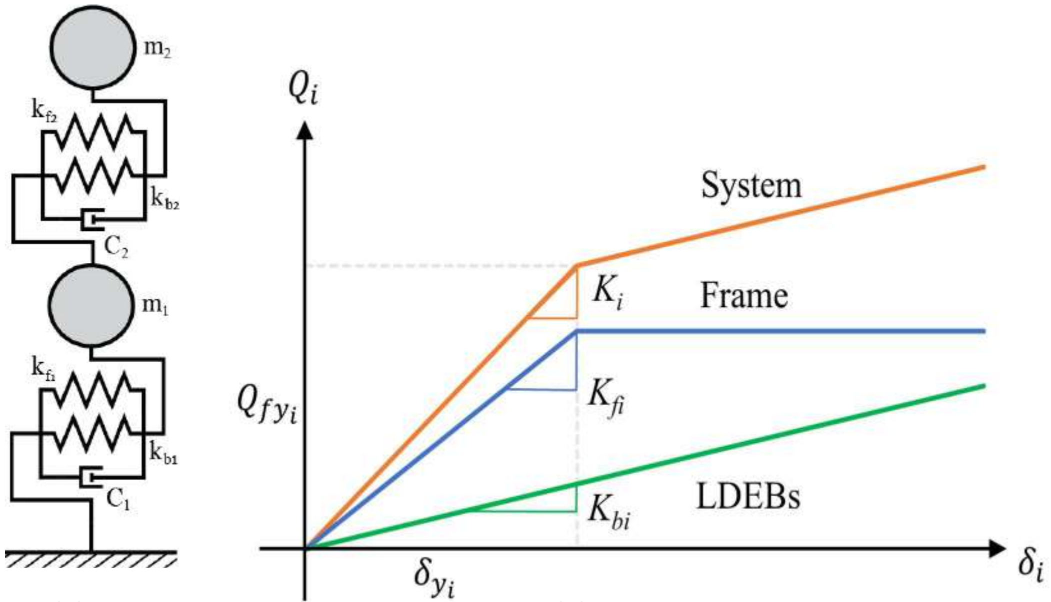

(a) (b)

Figure 4.1. Two–degrees–of–freedom system model (Reference [101]).

This research used a simplified 2–DOF system as a preliminary step to systematically explore the fundamental optimization behavior of LDEBs under seismic excitation. It enables the unambiguous identification of dominant parameters, nonlinear responses, and the interactions between LDEBs and the primary frame components, while the computational cost is affordable. Even though a 2–DOF system does not fully reflect the complexity of multi–story building structures compared with the real situation, it offers a well–defined test bed to verify the efficiency of the PSO and Round Robin hybrid optimization scheme. The understanding obtained here provides a solid ground for generalization to full multi–story MDOF models, which consider further aspects, including higher–mode effects, inhomogeneous stiffness distributions, and realistic combinations of load effects. Further research will apply the optimization methodology to taller structures with enhanced damping models and compare it with a more detailed structural representation and experimental data to validate the framework.

4.3. Natural Period and Mode Shapes

In earthquake engineering, each structure possesses a unique natural period governing its response to lateral forces such as ground motion during earthquakes. This inherent period, often identified through eigenvalue analysis, is crucial for design as it determines how a building sways in response to shaking. An effective seismic response relies on harmonizing forces with this natural period, allowing the building to resonate and efficiently dissipate energy.

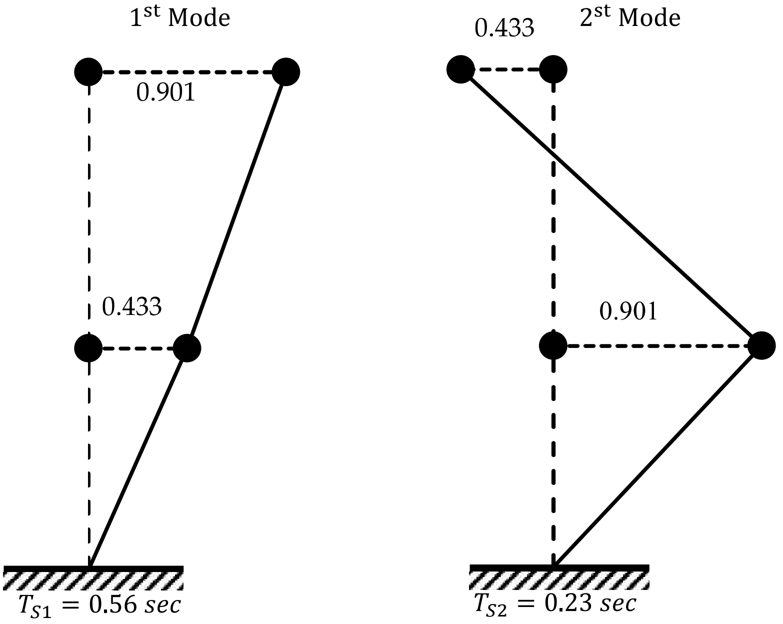

Figure 4.2. Mode shapes of 2–DOF system with LDEBs (Reference [101]).

Table 4.2. Natural periods.

Mode	1st Mode	2nd Mode
Without LDEBs	0.64	0.26
With LDEBs (K_{b1} = 90 kN/cm; K_{b2} = 56.7 kN/cm)	0.56	0.23
Change (%)	–12.50	11.54

Eigenvalue analysis helps us understand the dynamic behavior of 2–DOF systems. Table 4.2 presents the results of this analysis, highlighting the natural periods of different modes. Figure 4.2

provides the mode shapes, visually depicting the deformation patterns of the structure at each natural period. As shown, the first mode has a natural period of 0.56 sec, while the second mode vibrates faster, with a period of 0.23 sec. This knowledge of the 2–DOF system's natural periods and mode shapes forms the foundation for understanding how it interacts with earthquake forces.

4.4. Response Spectrum

Buildings, including our simplified 2–DOF models, are not passive recipients of earthquake force. Their response varies based on both their own natural periods and the earthquake's characteristics. To account for this dynamic interplay, engineers utilize response spectrum graphs. These graphs illustrate the maximum responses (e.g., displacement and velocity) a building experiences at different periods (or frequencies), essentially covering a range of potential earthquake scenarios. The velocity response spectrum is displayed in Figure 4.3. The selected earthquake records exhibit distinct frequency characteristics. At a natural period of approximately 0.5 seconds, Ohta NS produced a peak response of approximately 112 kine, whereas BCJ–L1 maintained a relatively constant response near 70 kine. However, for a natural period of approximately 0.9 seconds, Wakuya NS showed a response at a much higher level that was approximately estimated to be 285 kine. Hence, these three earthquakes were chosen so that their frequency contents and seismic intensities would cover a wide range of parameters for a more complete evaluation of the optimization performance of LDEBs in different seismic environments.

Figure 4.3 displays a velocity response spectrum, plotting the maximum expected velocity response (kine) against the natural period of the structure. This spectrum directly informs our understanding of how the 2–story model behaves in different earthquake scenarios. By comparing the natural periods identified in Table 4.2 and Figure 4.2 with the response spectrum in Figure 4.3, we can achieve the following:

- **Predict the dominant response:** If the natural period falls within a peak region of the spectrum, that specific frequency will likely cause significant vibrations in the building.
- **Understand the building behavior using the response spectrum:** Two–degrees–of–freedom models react differently during earthquakes depending on their natural vibration periods and the type of earthquake. To understand this, engineers use response spectrum graphs. These show the maximum shaking velocity a model might experience at different natural periods.
- **Optimize design interventions:** Knowing the expected response allows engineers to tailor reinforcements and energy dissipation strategies to effectively address the anticipated earthquake forces, considering the specific limitations and advantages of the 2–DOF model.

Incorporating both eigenvalue analysis and response spectrum analysis into the design process is crucial for ensuring an earthquake–resistant structure. Engineers can create effective strategies to minimize damage and safeguard occupants by understanding the 2–DOF model's natural periods and how it interacts with different earthquake frequencies.

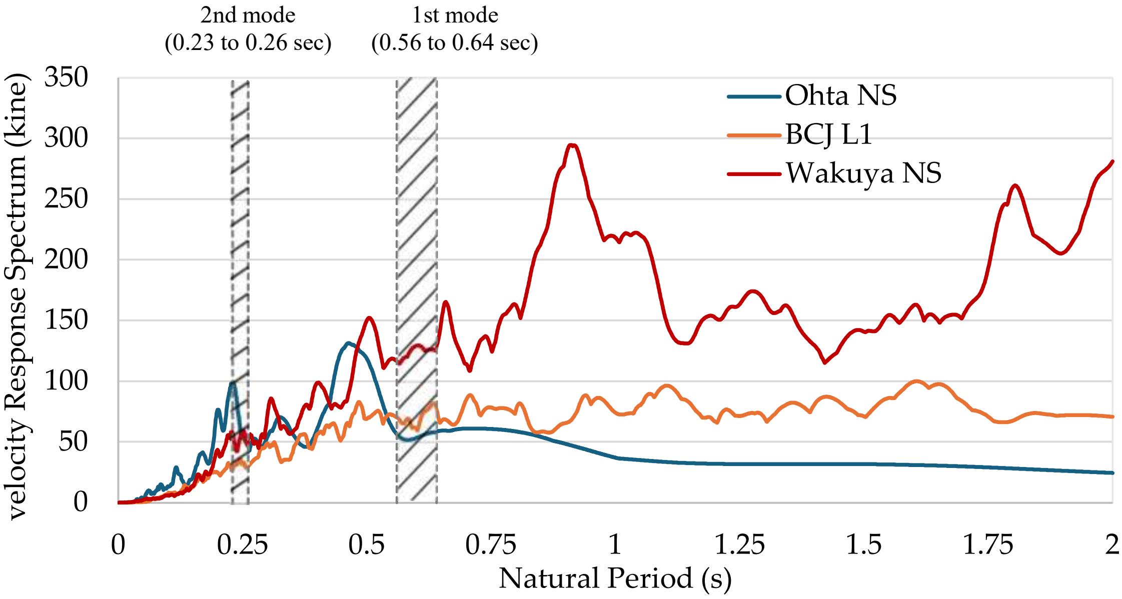

Figure 4.3. Velocity response spectrum of 2% damping ratio (Reference [101]).

4.5. Large Deformable Elastic Braces (LDEBs)

LDEBs are devices that never yield, even when subject to large deformations during major earthquakes [85]. In structures equipped with LDEBs, the elastic restoring force generated by these devices can improve the seismic response of major earthquakes [60]. Our study confirmed that LDEBs exhibit elastic properties. Figures 4.4 and Figure 4.5 illustrate LDEBs and their capability for substantial elastic deformation. The corresponding natural periods of the system with these devices are listed in Table 4.2. However, traditional braces have limitations in adjusting their elastic limits. In contrast, LDEBs possess a large yielding capacity and can dynamically modify their elastic limits, making them more effective in mitigating seismic responses across a wider range of earthquake intensities.

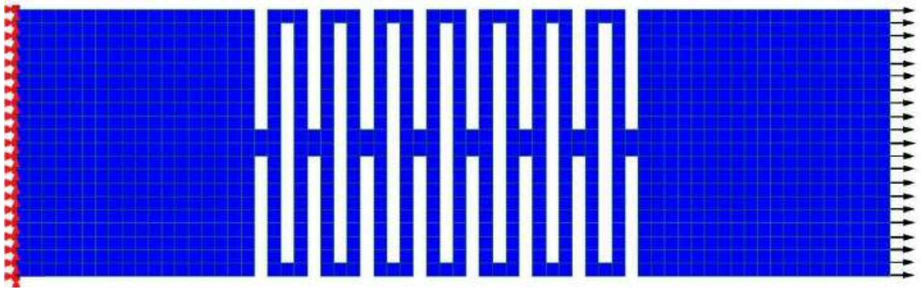

Figure 4.4. An example of LDEBs (Reference [101]).

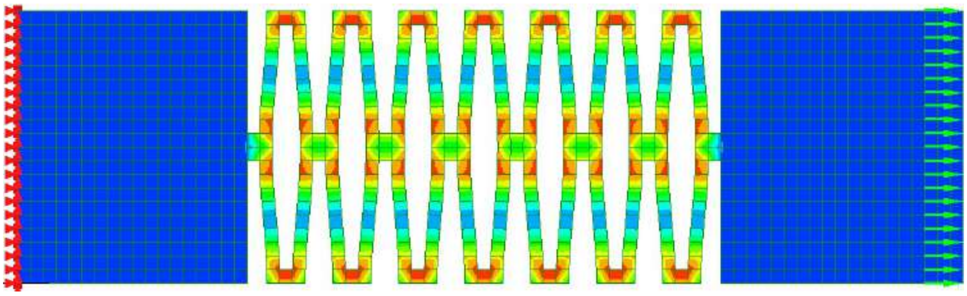

Figure 4.5. Deformation shape of LDEBs (Reference [101]).

4.6. Formulation of Optimization Problem

This study aimed to determine the optimal stiffness distribution of LDEBs in MDOF systems, which minimizes the maximum story drift response under seismic excitation. The LDEBs are represented as elastic spring elements installed in parallel with the primary frame elements at each story level. The optimization problem can be expressed in the following mathematical form:

$$\min_{\alpha} \max_{i=1,2} \left\{ \delta_{yi}(\alpha) \right\} \tag{4.3}$$

where $\alpha = (\alpha_1, \alpha_2)$ represents the stiffness ratio of LDEBs to the main frame at each story. $\delta_{yi}(\alpha)$ denotes the maximum story drift at story i, obtained via seismic response time–history analysis. The design variables α_i are dimensionless and bound within practical ranges based on preliminary structural considerations and the LDEBs' properties.

The search space for the design variables is constrained as

$$0 \leq \alpha_i \leq 0.3$$

This upper bound (30%) reflects realistic limits on the additional stiffness that can be introduced by LDEBs without compromising constructability, cost efficiency, or introducing excessive stiffness that may amplify higher–mode responses.

The maximum story drift serves as the objective function since excessive drift directly correlates with structural and non–structural damage during seismic events. The solution obtained aims to minimize the worst–case drift across both stories, enhancing seismic resilience.

4.7. Condition of Seismic Response Analysis

The seismic response analysis was performed iteratively to find the stiffness of a large deformable spring in each story. For the numerical solution of the equation of motion, the Newmark–β method was used with $\beta = 0.25$, the numerical integration time interval was 0.001 (s), the damping type was stiffness proportional damping, and the damping constant was 2% [91].

In this study, damping was assumed to be proportional to the overall stiffness of each story, including the main frame and LDEBs. This assumption compared the various stiffness setups consistently and simplified the numerical modeling as well. Although damping that is proportional to stiffness is standard for the analysis of the seismic response of MDOF systems, it may not model the complicated energy dissipation mechanisms that contribute to the LDEBs, which can show material hysteretic and geometrical nonlinearities while undergoing large deformations. The potential implications of this simplification are discussed in the Limitations Section.

4.8. Ground Motion Data

After a meticulous selection process, three ground motion records, including two real–world recordings and one artificial simulation, were obtained. Table 4.3 provides a concise overview of the key characteristics of these records. The ground acceleration for each individual record is presented in Figure 4.6. Figure 3.3 visualizes the 2% damped velocity response spectra for each record, along with the placement of the two–story systems modeled as 2–DOF systems within these spectra. This research utilized seismic waves at two distinct scaled velocity levels to facilitate a comprehensive analysis: 50 kine and 90 kine. Detailed information regarding these levels is available in Table 4.4. The velocity level of 50 kine corresponded to the major earthquake level in the current Japanese seismic code [92]. The velocity level of 90 kine was slightly above the largest value of strong motions from 79 moderate magnitude ($5.9 \geq Mw$) earthquakes that caused various degrees of impact on humans and built environments in Japan between 1996 and 2019, after the start of K–NET and KiK–net [93].

Table 4.3. Input seismic wave data.

Earthquake Name Station	Shimane 2018	Artificial	Tohoku 2011
	Ohta NS (SMN006)	BCJ–L1	Wakuya NS (JMA)
Seismic record duration time(s)	50	60	360
Maximum ground acceleration (gal)	477	207	406

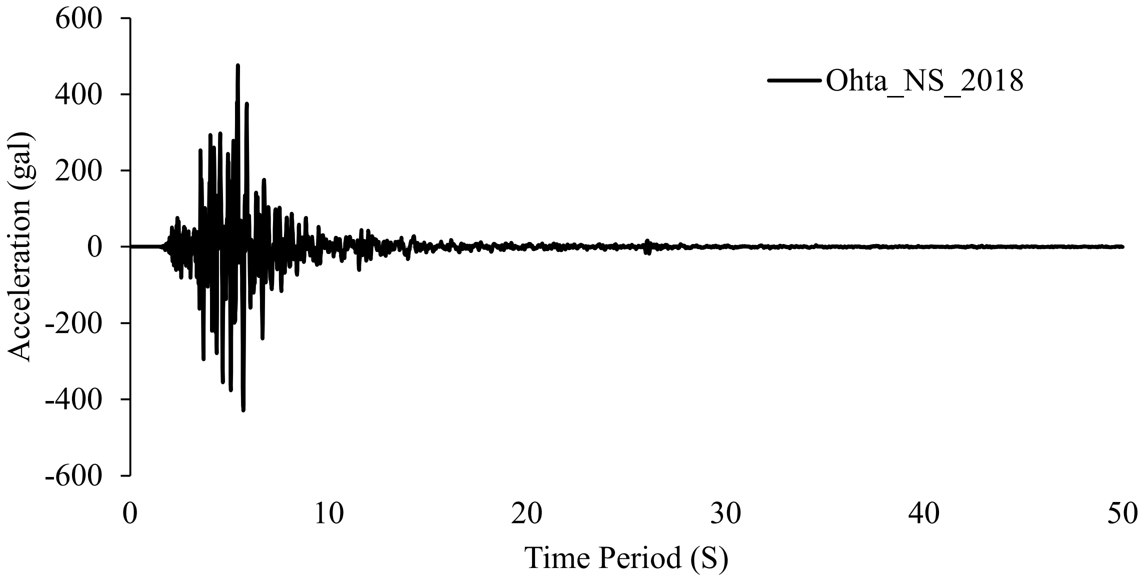

(a)

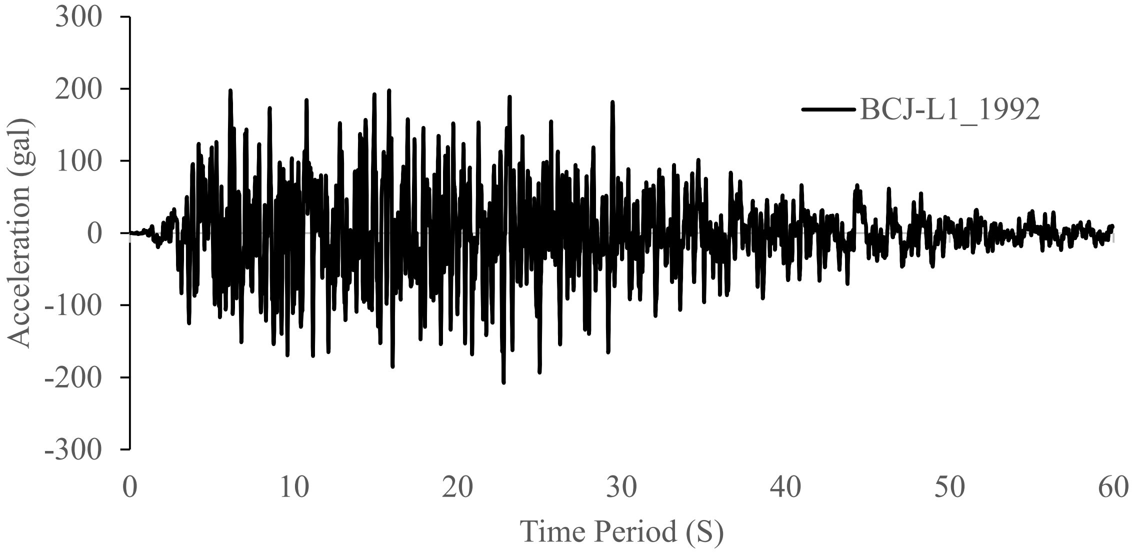

(b)

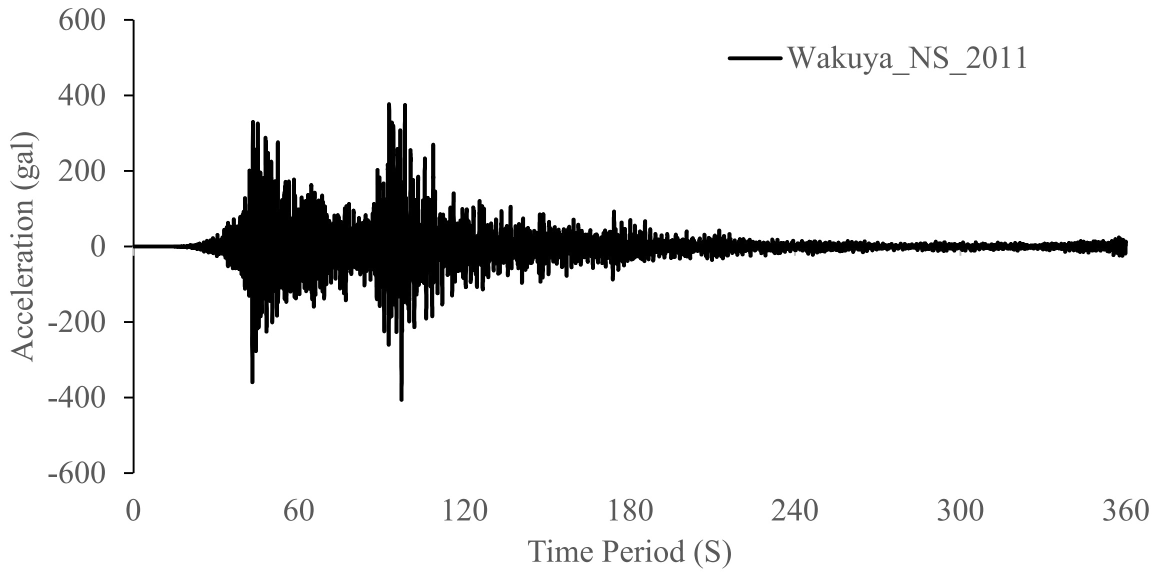

(c)

Figure 4.6. Seismic wave ground acceleration as (a) Ohta NS; (b) BCJ–L1; and (c) Wakuya NS (Reference [101]).

Table 4.4. Seismic multiplication factor.

Solutions	Maximum Acceleration (gal)	Maximum Velocity (kine)	Amplitude Multiplication Factor	
			50 kine	90 kine
Ohta NS	477	22.75	2.198	3.956
BCJ–L1	207	33.75	1.481	2.667
Wakuya NS	406	85.22	0.587	1.056

4.9. Optimization Methods

A two–stage hybrid computational framework was employed to effectively solve the formulated optimization problem, combining the global search capability of PSO with the verification robustness of Round Robin response surface analysis.

4.9.1. Phase 1: particle swarm optimization (PSO)

PSO is a population–based metaheuristic optimization algorithm, which is inspired by flocks' social behavior. Each particle moves toward its last best local position (P_{best}) and the global best position (G_{best}) in the swarm to obtain the best solution [94–96]. We minimized the problem such that

$$P_{best_i} = \min_{k=1,2...,t} \left\{ f\left(x_i^k\right) \right\}, \qquad \text{where } i \in \{1,2,...,N\} \tag{4.4}$$

$$G_{best_i} = \min_{k=1,2...,t} \left\{ f\left(x_i^k\right) \right\}, \qquad \text{where } i \in \{1,2,...,N\} \tag{4.5}$$

where i and N represent the particle index and the total number of particles, t denotes the current iteration number, f is the fitness value of the function, and P indicates the particles' position. In this study, each particle represents a candidate solution vector $\alpha = (\alpha_1, \alpha_2)$. The particles explore the defined solution space according to the following velocity and position update rules, detailed as follows:

$$V_i^{(t+1)} = \omega V_i^{(t)} + c_1 r_1 (P_{best_i} - x_i^{(t)}) + c_2 r_2 (G_{best_i} - x_i^{(t)}) \tag{4.6}$$

$$x_i^{(t+1)} = x_i^{(t)} + v_i^{(t+1)} \tag{4.7}$$

where $V_i^{(t)}$ and $x_i^{(t)}$ are the velocity and position of the particle. c_1 and c_2 are cognitive and social acceleration coefficients, respectively. r_1, r_2 are independent uniformly random variables between 0 and 1.

Since the inertia weight concept was proposed, a linear time–variant inertia weight was proposed to enhance the PSO algorithm's performance [97–100]. The role of the linear time–variant inertia weight ω_1^t is presented by the following equation:

$$\omega_1^{(t)} = \omega_{ini} - \left(\frac{i}{i_{max}} \right) (\omega_{ini} - \omega_{fin}) \tag{4.8}$$

Here, the initial value, $\omega_{ini} = 1.0$, the final value, $\omega_{fin} = 0.0$, and i_{max} is the maximum number of iterations. PSO efficiently searches the defined solution space to identify near–optimal stiffness ratios that minimize the maximum story drift for each seismic input considered.

4.9.2. Phase 2: Round Robin response surface analysis

Following PSO optimization, Round Robin analysis is employed to systematically verify the optimality of PSO solutions and visualize the sensitivity of the structural response over the entire solution space. In this phase,

1. A dense grid of α_1 and α_2 combinations within [0, 0.30] is generated.
2. For each grid point, time–history seismic response analysis is conducted using the Newmark integration method, with $\beta = 0.25$, a time step of $\Delta t = 0.001$ s, and a damping ratio of 2%.
3. The response surfaces of the maximum story drift are constructed, capturing the nonlinear interactions between the stiffness ratios and seismic response.
4. The PSO results are overlaid on these response surfaces to confirm whether they coincide with the global minimum identified through exhaustive Round Robin evaluations.
5. This two–stage optimization–validation framework ensures that the final solutions are both computationally efficient and globally reliable, capturing the complex nonlinear behaviors of LDEBs under varying seismic intensities.

4.10. Numerical Results Using PSO Optimization

This section showcases the optimization results for the two–story model (Figure 4.1) with LDEBs in various seismic scenarios. PSO, our chosen optimization method, tackled two distinct earthquake intensities: 50 kine and 90 kine. The optimization of the LDEBs' stiffness was conducted within a defined range to ensure practical and effective solutions. The minimum and maximum stiffness values were set to 0% and 30% of the LDEBs' stiffness against the frame, respectively. Each scenario aimed to minimize the maximum story drift while keeping the computational burden under 3000 iterations.

Table 4.5. Two–story PSO minimum solution results for Ohta NS waves.

Seismic Multiplication Factor	1st Story Stiffness Ratio α_1	2nd Story Stiffness Ratio α_2	Story Drift (cm)	Ductility Factors $\mu_{max} = max\ \{\mu_1, \mu_2\}$
50 kine	0.06	0.30	5.90	2.95
90 kine	0.21	0.30	10.52	5.26

Table 4.6. Two–story PSO minimum solution results for BCJ–L1 waves.

Seismic Multiplication Factor	1st Story Stiffness Ratio α_1	2nd Story Stiffness Ratio α_2	Story Drift (cm)	Ductility Factors $\mu_{max} = max\ \{\mu_1, \mu_2\}$
50 kine	0.24	0.26	3.90	1.80
90 kine	0.14	0.20	6.08	3.04

Table 4.7. Two–story PSO minimum solution results for Wakuya NS waves.

Seismic Multiplication Factor	1st Story Stiffness Ratio α_1	2nd Story Stiffness Ratio α_2	Story Drift (cm)	Ductility Factors $\mu_{max} = max\ \{\mu_1, \mu_2\}$
50kine	0.15	0.27	2.78	1.39
90kine	0.30	0.27	4.82	2.41

Tables 4.5, 4.6, and 4.7 unveil the optimal stiffness distribution for each story and the corresponding objective function values for the different seismic intensities. An intriguing observation emerged for the most intense scenario (90 kine), where both stories exhibited similar elastic–plastic behaviors, as depicted in the table. However, this harmony waned at lower intensities (50 kine). This phenomenon can be attributed to the interplay between earthquake characteristics and structural response mechanisms. At higher intensities, the dominant earthquake forces necessitate a more uniform distribution of stiffness across the stories to effectively counter

the larger deformations. In contrast, lower intensities might trigger localized responses, leading to optimal stiffness distributions that prioritize strengthening specific stories.

Figure 4.8 vividly illustrates the trade–off relationship between the stiffness ratio (α_i) and the ductility factor (mi = maximum story drift of ith story/δ_{y_i}) for the first and second stories' Round Robin response surface. The stiffness ratio is defined as the ratio of the LDEBs to the frame's stiffness ($\alpha_i = K_{b_i}/(K_{b_i} + K_{f_i}$). The ductility factor is a measure of how much the brace can deform before failure. These Figures also depict the combined results of the first and second stories. The global optimum point on the graph where the stiffness ratio was minimized corresponds to the PSO results in Tables 4.5, 4.6, and 4.7.

This study clearly states that the optimal stiffness ratio for LDEBs depends on several factors including:

The earthquake intensity: Different earthquake intensities require different stiffness distributions to optimize the response.

The natural periods of the structure: The natural periods of the structure influence how it interacts with earthquake forces, and the optimal stiffness ratio should account for these periods.

Ground motion characteristics: The specific characteristics of the ground motion (e.g., frequency content) can also impact the optimal stiffness ratio.

Therefore, it is impossible to provide a single best stiffness ratio for all situations. The optimal value will vary depending on the specific scenario and design requirements. This study presents optimization methods such as PSO and Round Robin analysis to help determine the optimal stiffness ratio for a particular case.

4.10.1. Quantitative comparative analysis

While Tables 4.5–4.7 and Figure 4.8 provide descriptive insights into the optimized stiffness ratios and ductility factors under various seismic intensities, a quantitative comparative analysis further clarifies the effectiveness of the optimization framework. Table 4.8 summarizes the percentage reduction in maximum story drift achieved using PSO optimization compared with the unbraced frames (i.e., without LDEBs).

Table 4.8. Percentage reduction in maximum story drift after optimization.

Seismic Input	Unbraced Drift (cm)	Optimized Drift (cm)	Reduction (%)
Ohta NS (50 kine)	9.99	5.90	41.00%
Ohta NS (90 kine)	12.36	10.52	15.00%
BCJ–L1 (50 kine)	9.01	3.90	57.00%
BCJ–L1 (90 kine)	17.01	6.08	64.25%
Wakuya NS (50 kine)	5.35	2.78	48.00%
Wakuya NS (90 kine)	13.17	4.82	63.50%

The formula to compute the percentage reduction in maximum story drift is

$$\text{Reduction }(\%)=\frac{\text{Unbraced Drift - Optimized Drift}}{\text{Unbraced Drift}}\times 100 \tag{4.9}$$

These findings show that optimized LDEB designs significantly enhance structural properties. Reductions in maximum story drift between 15% and more than 64%, depending on ground motion features and intensity. The maximum percentages of reductions were found under the high–intensity inputs, which shows the superiority of the developed LDEB system under severe seismic actions.

4.10.2. PSO convergence behavior

The convergence behavior of the PSO algorithm was monitored for all seismic input cases to assess its computational efficiency. Figure 4.10 illustrates the convergence histories for all earthquake records at both 50 kine and 90 kine intensity levels.

In most scenarios, PSO achieved stable convergence within approximately 800 iterations, significantly below the maximum allowed 3000 iterations. The smooth and consistent decline in the objective function across all cases indicated stable search behavior, the efficient exploration of the solution space, and the reliable identification of global optimal stiffness distributions.

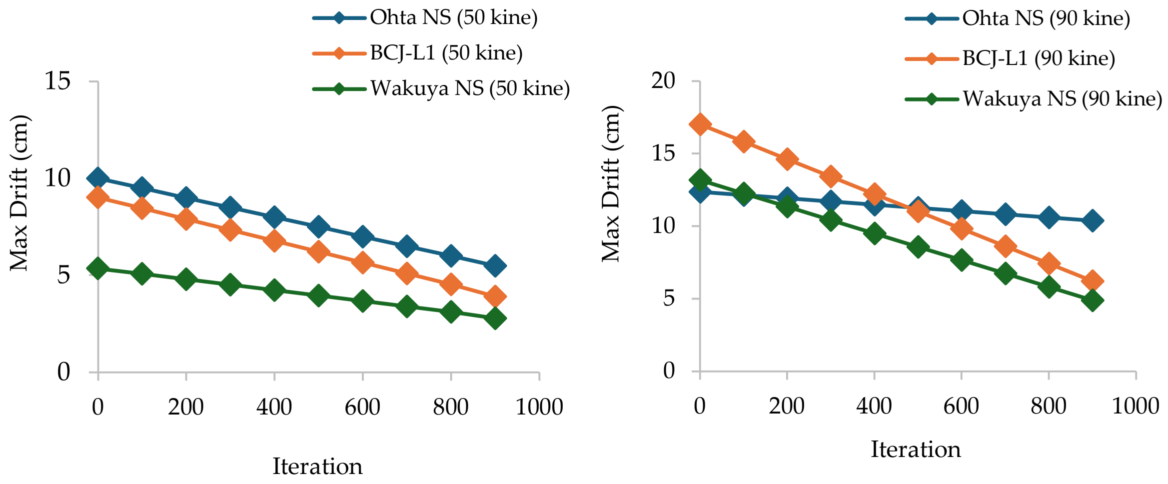

Figure 4.7. PSO convergence behavior for all seismic inputs (Reference [101]).

The PSO convergence behavior for all seismic inputs is presented. The left subfigure shows the convergence for Ohta NS, BCJ–L1, and Wakuya NS under a 50 kine seismic intensity. The right subfigure shows the convergence for the same earthquake records under a 90 kine intensity. PSO achieved convergence within 800–900 iterations across all cases, confirming the robustness and stability of the optimization framework.

4.10.3. Relationship between stiffness and ductility

Figure 4.7 visualizes the relationship between stiffness ratios and ductility factors. As the LDEB stiffness ratios increased, the ductility factors decreased, reflecting reduced deformation demands. However, excessive stiffness can elevate higher mode participation, potentially introducing detrimental dynamic effects. Therefore, the optimal solution balances sufficient stiffness to suppress drift while maintaining flexibility to avoid adverse higher–mode amplification.

4.11. Numerical Results by Round Robin Analysis

This study underscores the suitability of steel construction in earthquake–prone regions and emphasizes the critical concept of seismic resilience. This research introduced LDEBs to enhance seismic performance in structural design. This investigation focused on steel buildings incorporating LDEBs, which were represented as 2–DOF systems (Figure 4.1).

Figure 4.2 and Table 4.2 present the natural periods of the two–story model. These periods could have been used to inform the initial stiffness ratios for the PSO and Round Robin analyses. For instance, knowing the dominant vibration modes (shapes) and corresponding periods could help tailor the stiffness distribution to better counteract specific earthquake frequencies.

Figure 4.3 showcases a three–velocity response spectrum, revealing how our structure responded to different earthquake scenarios. Under the Ohta NS wave, the first mode swayed a significant 56 kine, while the second mode followed closely at 100 kine. The BCJ–L1 wave elicited a more subdued response, with 70 kine in the first mode and 28 kine in the second. The Wakuya NS wave packed the biggest punch, sending the first mode rocketing to 117 kine while the second mode peaked at 58 kine. These insights, along with additional velocity response spectra presented in Figure 4.3 for various seismic events, could have been leveraged in two keyways: firstly, by strategically choosing scaled velocity levels (50 and 90 kine) for optimization, and secondly, by guiding the initial placement of stiffness ratios within the optimization algorithms' search space. This would have ensured our structure was adequately prepared to handle diverse tremors.

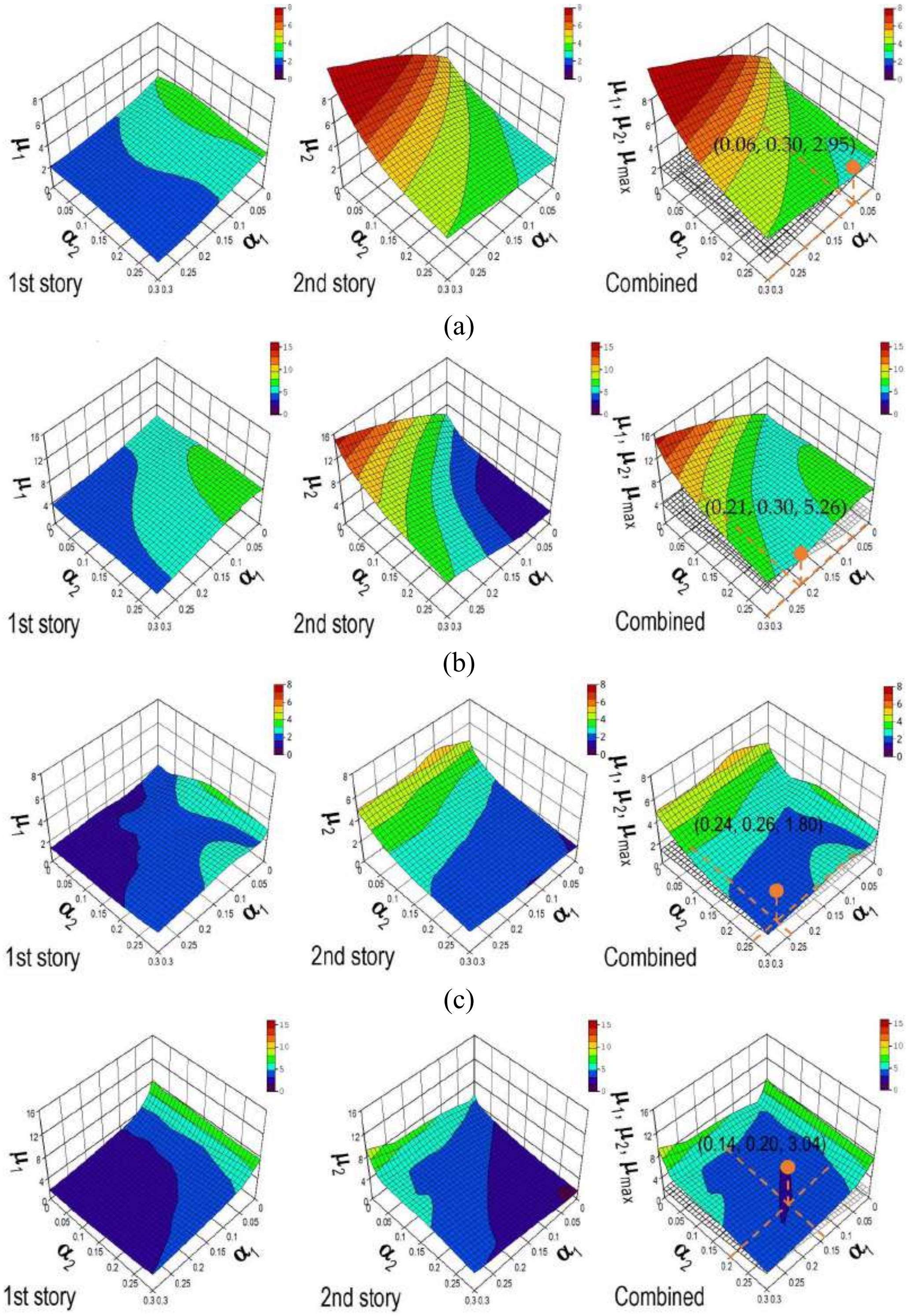

(a)

(b)

(c)

(d)

Figure 4.8. The relationship between maximum story drift and story stiffness ratio by Round Robin analysis (Reference [101]).

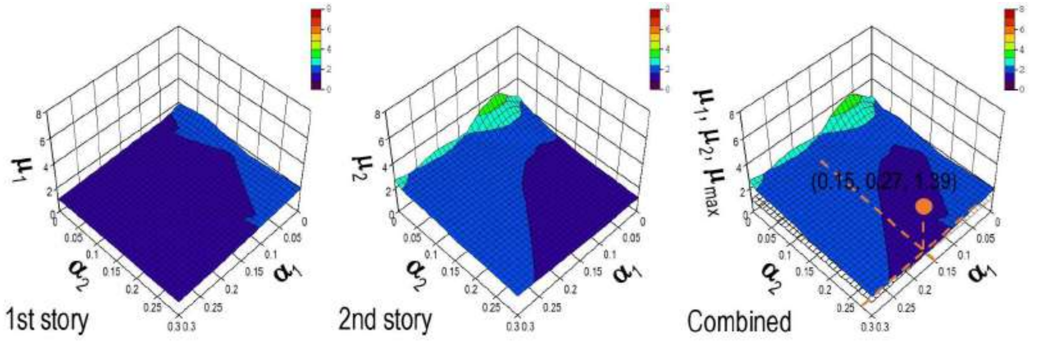

(e)

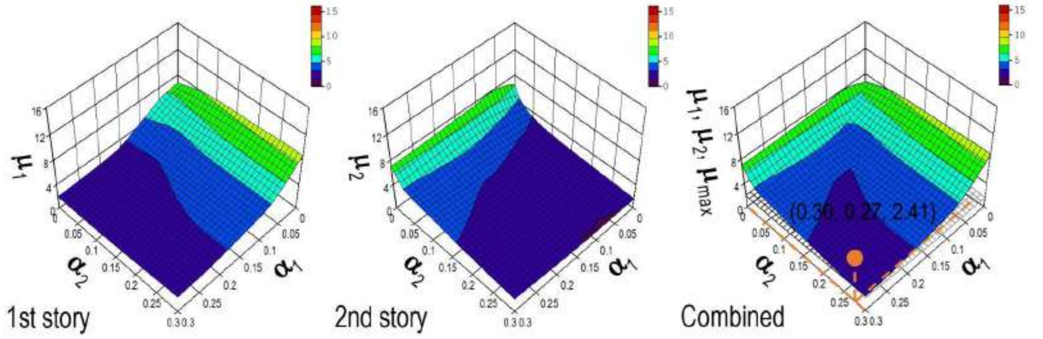

(f)

$\alpha_i = K_{bi} / K_{fi}, \mu_{max} = max\ \{\mu_1, \mu_2\}$, and the brackets present the PSO minimum results of α_1, α_2 and $\mu_{\max}$.

Figure 4.8. The relationship between maximum story drift and story stiffness ratio by Round Robin analysis as (a) Ohta NS wave (50 kine); (b) Ohta NS wave (90 kine); (c) BCJ–L1 (50 kine); (d) BCJ–L1 (50 kine); BCJ–L1 (90 kine); (e) Wakuya NS wave (50 kine); and (f) Wakuya NS wave (90 kine) (Reference [101]).

Figure 4.8 demonstrates the relationship between the maximum story drift and story stiffness ratio by Round Robin analysis. The orange data points on the graphs represent the results obtained from the PSO approach, specifically highlighting the minimum solutions achieved through PSO. These figures consistently show valley–shaped response surfaces, illustrating the model's behavior during significant seismic events. The valley–shaped surfaces consisted of the first and second story response surfaces combined. Moreover, the first story response became the same as the second story response, and the two stories gave a smaller response locally on the valley lines. Consequently, the PSO solutions were located on the valley lines in almost all cases. The findings from both the PSO and Round Robin experiments validate the PSO minimum solution as the global optimum of the Round Robin response surface. Ultimately, these insights highlight the impact of inherent frequency alterations on stiffness ratios, resulting in the structure's enhanced strength, durability, and usability during moderate seismic events and severe earthquakes.

Figure 4.8(c–f) for BCJ–L1 and Wakuya NS wave show that μ_1 decreased as α_1 increased, and μ_2 decreased as α_2 increased. Consequently, this result formed a valley shape centered on the combined response surface. Meanwhile, the results are difficult to understand in the case of the Ohta wave. Figure 4.8(a–b) demonstrate that μ_2 significantly increased as α_1 increased in the small α_2 region. This difficult–to–understand result shifted the valley shape rightward on the combined response surface. The reason for the result is that increasing α_1 led to increasing the second mode response. We can observe the first peak at 0.23s of the natural period on the response spectrum for the Ohta wave, as shown in Figure 4.3.

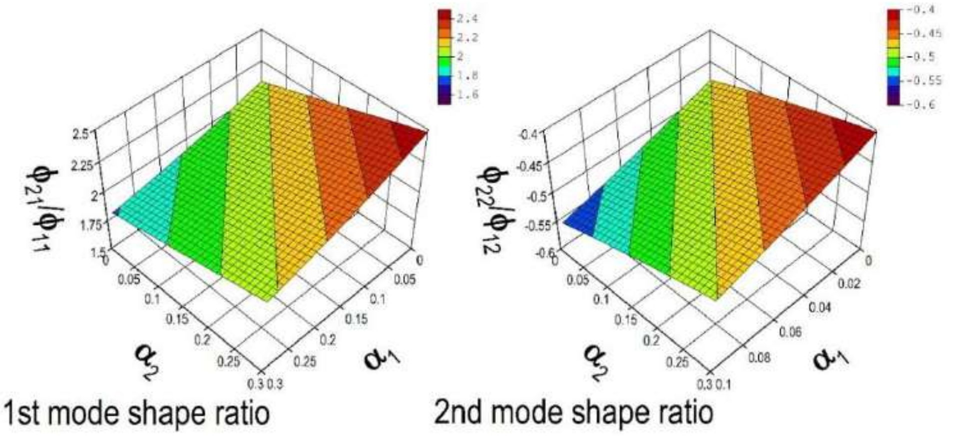

1st mode shape ratio

2nd mode shape ratio

Figure 4.9. Modal properties change in natural period and mode shape (1st story fixed to 1) due to varying stiffness ratio (Reference [101]).

Table 4.2 shows that the natural periods of both the first and second modes decreased as the LDEBs' stiffness ratio increased. This means that the structures became stiffer as the LDEBs became stiffer.

This is because the LDEBs added stiffness to the structure, which reduced the overall stiffness of the system. As a result, the structures vibrated at lower frequencies (longer periods).

Figure 4.9 shows the changes in the mode shapes due to the varying stiffness ratio. The mode shapes are plotted as the relative displacement of each floor, with the first floor fixed at one. As the stiffness ratio increased, the mode shapes became more concentrated in the lower floors. This means that the upper floors vibrated less compared with the lower floors. This is because the LDEBs were on the lower floors, and they added more stiffness to these floors.

Figure 4.10 shows that the spectral velocity values at both the first and second modes decreased as the LDEBs' stiffness ratio increased except for the second mode of Ohta. This means that the structures became stiffer as the LDEBs became stiffer. This is consistent with the observations made in Table 4.2 and Figure 4.9.

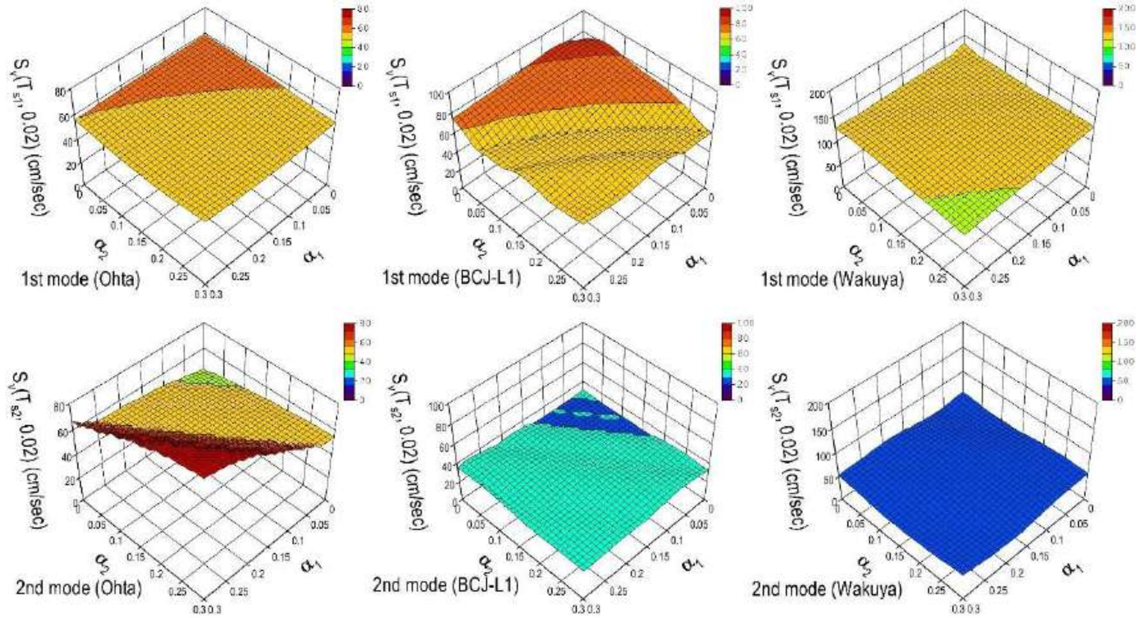

Figure 4.10. Response surface illustrates the relationship between axial stiffness (k), damping ratio (ζ), and maximum displacement (Δmax) of LDEP system under seismic loading. The surface indicates how variations in k and ζ influenced Δmax. Axes are labeled with corresponding units: k (kN/mm), ζ (%), and Δmax (mm) (Reference [101]).

This study successfully demonstrated the effectiveness of LDEBs in enhancing the seismic resilience of steel structures. LDEBs, despite seeming to decrease stiffness, led to improved strength, durability, and reduced story drift. Optimizing the LDEBs' placement and stiffness ratios proved crucial, suggesting potential for wider use in earthquake–prone regions.

4.12. Limitations

In this paper, response surfaces were visualized for just two design variable models (SDOF). In cases with more than three design variables, we can visualize response surfaces on any two–design–variable axes around a PSO optimum solution.

This study adopted a damping model that assumed proportionality to total stiffness, which included contributions from both the main frame and the LDEBs. Although this approach enables computational efficiency and is widely used in seismic analysis, it cannot fully capture the complex damping behaviors for geometrically nonlinear components. LDEBs may introduce additional damping effects related to their large deformation capacity, restoring forces, and interaction with the main structural frame. As such, the current assumption may lead to some simplification of the dynamic response, particularly under strong seismic excitation. Future studies are encouraged to explore more detailed damping models that incorporate these nonlinear effects for a more comprehensive evaluation of LDEBs' performance.

4.13. Conclusions

This study showed that LDEBs can effectively improve the seismic performance of steel structures. Using LDEBs can lead to increased strength, durability, and reduced story drift. Optimizing LDEBs' placement and stiffness ratios proved crucial, suggesting potential for wider use in earthquake–prone regions.

Here are some of the key findings of this study:

1. Optimized LDEB stiffness distributions significantly reduced maximum story drifts and ductility demands across different seismic inputs, achieving drift reductions ranging from 15% to over 64%, depending on the earthquake characteristics.
2. The optimal stiffness distribution of LDEBs depends on the earthquake intensity, the natural periods of the structure, and the ground motion frequency content. LDEBs dynamically shift natural periods away from resonance regions, suppressing the amplification of the seismic response and minimizing damage.
3. PSO is an effective method for finding the optimal stiffness distribution of LDEBs.
4. Round Robin analysis can be used to validate the PSO results and provide additional insights into the behavior of the structure.

Overall, this study provides valuable insights for designers who are considering using LDEBs to improve the seismic performance of steel structures. By optimizing the placement and stiffness of LDEBs, designers can create structures that exhibit favorable modal behavior, reduce both first– and higher–mode amplifications, and enhance seismic resilience across a wide range of earthquake intensities. In particular, by integrating PSO with Round Robin analysis, this study provides a more comprehensive optimization and validation framework, which allows designers to capture global optima while simultaneously visualizing the sensitivity of structural response across a broad range of stiffness configurations and seismic intensities. This dual approach advances current optimization practices for LDEBs beyond conventional methods.

Furthermore, the PSO–based optimization framework developed in this study holds significant potential for practical engineering applications. In early–stage design, it enables structural engineers to identify optimal LDEB stiffness distributions that shift structural periods away from resonance zones and minimize inter–story drift, leading to enhanced seismic resilience while ensuring material and cost efficiency. In retrofit scenarios, this approach can guide the selective implementation of LDEBs in existing structures, improving seismic performance without requiring major structural alterations. The integrated PSO equipment with Round Robin validation guarantees both the overall optimization and seismic diversity and robustness of these optimum design solutions so engineers can make performance–based decisions for buildings constructed in seismic zones.

CHAPTER 5: CONCLUSIONS

This research has developed a holistic scientific and engineering framework for LDEBs as a seismic mitigation concept that reduces the key issue of residual deformation in earthquake–resistant building structures. By conducting three collaborating investigations of experimental verification, failure mode analysis, and system optimization for LDEB performance improvement, this study has elevated the LDEBs from conceptual innovation to practical implementation.

The experimental and analytical study of tensile behavior (Chapter 3) showed that the LDEBs retained elastic properties for strains up to 1/200 and 1/80 of their original length, ten times that expected in regular steel structural members. Three FEM–optimized samples (F1–1, F1–2 and F2) were tested on which good agreements were found between experiments and FEM predictions including yielding loads and displacements. Use of closed–form predictive equations derived from flexural theory allows practical engineers to design LDEBs without resorting to advanced finite–element–analysis techniques. The present study, which is presented in the Journal of Structural Engineering B (2025) offers to the worldwide structural engineering practice some validated design tools available straight away.

The compressive response study overcame a major obstacle to practical LDEB implementation by demonstrating that buckling is effectively avoided when proper geometric constraints are met. Both eigenvalue analysis and experimental results confirm that LDEBs do not fail by buckling. Experimental verification demonstrated that local yielding occurs at 3.00 kN and no buckling up to 5.90 kN which extends the applicability of LDEBs to compression members in braced frames and knee braces overstressed by combined axial load and bending effect design cases.

The optimization of the stiffness distribution (Chapter 4) was the crucial point that connected the component response to system level seismic response. Employing the hybrid methodology that consists of particle swarm optimization in combination with multi scenario Round Robin response surface analysis, it was found out by this study that well designed LDEB configurations result in a change of maximum story drifts of 15–64% when compared to those revealed from the corresponding unbraced frames under distinct shaking events. The optimization process indicated that optimum building under earthquake loading depends on the seismic intensity and frequency content with highest percentage increase at high intensity shaking where life safety is of great concern. This work has been published by the Journal of Buildings (2025) and provides validated optimization procedures to the structural engineer that allow the efficient identification of performance maximizing designs.

These three ingredients together demonstrate that LDEBs are a mature technology with unique benefits compared to traditional seismic control methods. Unlike hysteresis dampers where energy dissipates through the irrecoverable plastic deformation, LDEBs do not degrade in performance with each earthquake and exhibits elastic response to restore Structures under a load to their original state directly targeting residual drift, critical for post–earthquake building function. Even after the main structure of frames yield, LDEBs have ability to provide elastic restoring force, hence secondary stiffness that is not attainable by conventional techniques.

Practical implications are substantial and immediate. The prediction equations and optimization methodologies allow the engineer to include LDEBs in new construction and retrofit projects under performance–based design methods, in which given drift reduction targets are used to select a configuration. The extensive validation experiments, analytical developments and documented performance benefits provide the technical justification to add this new technology into building codes and seismic design standards. Publishing of the two major branches in the research sector guarantees that these results directly lead to further development of seismic protective technology in real application.

Downstream research efforts to further build on this foundation will be to multi story MDOF systems that include higher modes effects, shake table testing to demonstrate system level performance with realistic earthquake sequences, develop connection detailing based on component level testing and hybrid systems that combine LDEBs with other seismic solutions. Studies on long term durability would also provide additional practical relevance.

This research argues that it is not only conceptually but also practically possible to shift the paradigm from damage tolerances to a damage prevention regime in which the elastic restorative ability plays an analogous role as reparative bone in bone tissue. The fact that elastic design is retained, even in the presence of more extreme deformations than those at which common members fail, allows structures to snap back into original profile after earthquakes rather than crumble, maintaining function and worth. With the seismic hazard, urbanization pressures, and resilience aspirations mounting, technologies such as LDEBs that reduce residual damage and offer a mechanism to quickly restore functionality will continue to be critical in shaping our built environment in a way that is not only capable of surviving major earthquakes but emerges ready for further use by its community. This study will present the scientific basis, practical tools, and proven procedures required to allow structural engineers to employ LDEB technology with confidence in support of achieving the overarching objective of building resilient earthquake–resistant design solutions.

Future Study

The future development of research on Large Deformable Elastic Braces (LDEBs) will focus on expanding from fundamental analysis to full–scale application and practical design evaluation. The following studies are proposed as the next stages of this work:

1. Static and Dynamic Behavior of 2D Portal Frames Using Large Deformable Elastic Braces.
2. Cost and Economic Feasibility Analysis of Structures with and without Large Deformable Elastic Braces.
3. Seismic Performance Evaluation of 3D Steel Frames Incorporating Large Deformable Elastic Braces.
4. Experimental Verification of Full–Scale Large Deformable Elastic Brace Systems under Shaking–Table and Pseudo–Dynamic Loading.

Reference

[1] Sawada, K., Kajitani, K., Uno, T., Teramoto, J., & Komatsu, S. (2022). A study on multi-objective optimization of large deformable elastic plates. *Buildings, 12*(9), 1323. https://doi.org/10.3390/buildings12091323

[2] Sawada, K. (2020). Topology optimization of large deformable elastic plates. *Journal of Structural and Construction Engineering (Transactions of AIJ), 85*(771), 683–692. https://doi.org/10.3130/aijs.85.683

[3] Kuramoto, H. (2006). Seismic design codes for buildings in Japan. *Journal of Disaster Research, 1*(3), 341–356. https://doi.org/10.20965/jdr.2006.p0341

[4] Otani, S. (2021). Development and present status of seismic evaluation and seismic retrofit of existing reinforced concrete buildings in Japan. *Journal of Asian Architecture and Building Engineering, 3*(1), 1–10. https://doi.org/10.3130/jaabe.3.1

[5] McCormick, J., Aburano, H., Ikenaga, M., & Nakashima, M. (2025). Multidisciplinary research to advance the development of functional recovery for community resilience. *Disaster Prevention and Resilience, 2*(1), Article 15. https://doi.org/10.20517/dpr.2023.15

[6] Priestley, M. J. N. (2000). Performance based on seismic design. *Bulletin of the New Zealand Society for Earthquake Engineering, 33*(3), 325–346. https://doi.org/10.5459/bnzsee.33.3.32 25-346

[7] Mahin, S. A. (1998). Lessons from damage to steel buildings during the Northridge earthquake. *Engineering Structures, 20*(4–6), 261–270. https://doi.org/10.1016/S0141-0296(97)00032-1

[8] Kawashima, K., & Unjoh, S. (1996). Impact of Hanshin/Awaji earthquake on seismic design and seismic strengthening of highway bridges. *Structural Engineering International, 6*(3), 179–184. https://doi.org/10.2749/101686696780495536

[9] Astroza, M., Ruiz, S., & Astroza, R. (2012). Damage assessment and seismic intensity analysis of the 2010 (Mw 8.8) Maule earthquake. *Earthquake Spectra, 28*(S1), S145–S164. https://doi.org/10.1193/1.4000027

[10] Kajitani, Y., Chang, S. E., & Tatano, H. (2013). Economic impacts of the 2011 Tohoku-Oki earthquake and tsunami. *Earthquake Spectra, 29*(S1), S457–S478. https://doi.org/10.1193/1.4000108

[11] Korkmaz, K. A., Demir, C., Sivri, M., & Börekçi, O. S. (2023). Observations on the Van earthquake and structural damage. *Natural Hazards, 119*(1), 1–25. https://doi.org/10.1007/s11069-023-06010-x

[12] Hori, T., Kato, N., Hirahara, K., Baba, T., & Kaneda, Y. (2004). A numerical simulation of earthquake cycles along the Nankai Trough in southwest Japan. *Journal of Geophysical Research: Solid Earth, 109*(B6), B06302. https://doi.org/10.1029/2003JB002703

[13] Goldfinger, C., Ikeda, Y., Yeats, R. S., & Ren, J. (2013). Super quakes and super cycles. *Seismological Research Letters, 84*(1), 24–32. https://doi.org/10.1785/0220110135

[14] Takahashi, Y. (2019). Review on seismic isolation and response control methods of buildings in Japan. *Geoenvironmental Disasters, 6*(1), Article 7. https://doi.org/10.1186/s40677-019-0123-y

[15] De Luca, A., & Guidi, L. G. (2019). State of art in the worldwide evolution of base isolation design. *Soil Dynamics and Earthquake Engineering, 125*, Article 105722. https://doi.org/10.1016/j.soildyn.2019.105722

[16] Naeim, F., & Kelly, J. M. (1999). *Design of seismic isolated structures: From theory to practice*. John Wiley & Sons.

[17] Black, C. J., Makris, N., & Aiken, I. D. (2004). Component testing, seismic evaluation and characterization of buckling-restrained braces. *Journal of Structural Engineering, 130*(6), 880–894. https://doi.org/10.1061/(ASCE)0733-9445(2004)130:6(880)

[18] Sabelli, R., Mahin, S., & Chang, C. (2003). Seismic demands on steel braced frame buildings with buckling-restrained braces. *Engineering Structures, 25*(5), 655–666. https://doi.org/10.1016/S0141-0296(02)00175-X

[19] Watanabe, A., Hitomi, Y., Saeki, E., Wada, A., & Fujimoto, M. (1988). Properties of brace encased in buckling-restraining concrete and steel tube. In *Proceedings of the Ninth World Conference on Earthquake Engineering* (Vol. IV, pp. 719–724). Tokyo–Kyoto, Japan.

[20] Tsai, K. C., Hsiao, P. C., Wang, K. J., Weng, Y. T., Lin, M. L., Lin, K. C., Chen, C. H., Lai, J. W., & Lin, S. L. (2008). Pseudo-dynamic tests of a full-scale CFT/BRB frame—Part I: Specimen design, experiment and analysis. *Earthquake Engineering & Structural Dynamics, 37*(7), 1081–1098. https://doi.org/10.1002/eqe.804

[21] Hariri, B., Montgomery, M., Zhong, C., & Christopoulos, C. (2025). Enhancing the seismic stability of buckling-restrained steel braced frames in subduction interface seismic regions using viscoelastic dampers. *Earthquake Spectra, 41*(1), 457–489. https://doi.org/10.1177/87552930241298916

[22] Banihashemi, M. A., & Wiebe, L. (2025). Seismic loss comparison for buildings designed with ductile steel seismic force-resisting systems and with controlled rocking braced frames. *Earthquake Spectra, 41*(1), 127–153.

[23] Ferrari, F., & Sigmund, O. (2021). Topology optimization methods for 3D structural problems: A comparative study. *Archives of Computational Methods in Engineering*, *28*, 1–58. https://doi.org/10.1007/s11831-021-09626-2

[24] Sawada, K., Uno, T., & Nishida, G. (2017). Analytical study on large deformable elastic members. *Journal of Structural Engineering B, 63B*, 345–352. [In Japanese]

[25] Teramoto, J., Sawada, K., & Komatsu, S. (2019). Study on the determination of the structure of large elastic members that can withstand compressive loads using bending process.

Journal of Structural and Construction Engineering (Transactions of AIJ), 84(765), 1557–1565. [In Japanese]

[26] Sawada, K. (2018). Seismic response analyses of RC portal frames with large deformable elastic braces. *International Journal of Computational Methods and Experimental Measurements*, 6(5), 880–886. WIT Press. https://doi.org/10.2495/CMEM-V6-N5-880-886

[27] Rashid, M. H. U., Komatsu, S., & Sawada, K. (2025). Performance of optimized large deformable elastic plates under tensile load. *Journal of Structural Engineering B, 71B*, 103–112. https://doi.org/10.3130/aijjse.71B.0_103

[28] Kishizoe, M., & Sawada, K. (2020). Seismic response of steel structural frameworks incorporating large deformed elastic members as braces. *Journal of Steel Structures, 27*(105), 53–60.

[29] Algamati, M., Rahman, M. N., Kumar, S., Nazir, S., & Al-Sherrawi, M. H. (2025). Energy dissipation technologies in seismic retrofitting. *CivilEng*, *6*(2), 23. https://doi.org/10.3390/civileng6020023

[30] Housner, G. W., Bergman, L. A., Caughey, T. K., Chassiakos, A. G., Claus, R. O., Masri, S. F., Skelton, R. E., Soong, T. T., Spencer, B. F., Jr., & Yao, J. T. P. (1997). Structural control: Past, present, and future. *Journal of Engineering Mechanics*, *123*(9), 897–971. https://doi.org/10.1061/(ASCE)0733-9399(1997)123:9(897)

[31] Housner, G. W., Bergman, L. A., Caughey, T. K., Chassiakos, A. G., Claus, R. O., Masri, S. F., Skelton, R. E., Soong, T. T., Spencer, B. F., Jr., & Yao, J. T. P. (1997). Structural control: Past, present, and future. *Journal of Engineering Mechanics*, *123*(9), 897–971. https://doi.org/10.1061/(ASCE)0733-9399(1997)123:9(897)

[32] Li, X., Zou, J., Zhao, Y., & Wang, D. (2023). Research on the application of BRBs in seismic resistance of bridge. *Materials*, *16*(7), 2549. https://doi.org/10.3390/ma16072549

[33] Dharmajan, N. B., & AlHamaydeh, M. (2025). State-of-the-art review of structural vibration control: Overview and research gaps. *Applied Sciences*, *15*(14), 7966. https://doi.org/10.3390/app15147966

[34] Pall, A. S., & Marsh, C. (1982). Response of friction damped braced frames. *Journal of the Structural Division*, *108*(6), 1313–1323. https://doi.org/10.1061/JSDEAG.0005968

[35] Li, X., Zou, J., Zhao, Y., & Wang, D. (2023). Research on the application of BRBs in seismic resistance of bridge. *Materials*, *16*(7), 2549. https://doi.org/10.3390/ma16072549

[36] Ras, A., & Boumechra, N. (2016). Seismic energy dissipation study of linear fluid viscous dampers in steel structure design. *Alexandria Engineering Journal*, *55*(3), 2821–2832. https://doi.org/10.1016/j.aej.2016.07.012

[37] Katsimpini, P., Papagiannopoulos, G., & Hatzigeorgiou, G. (2025). A thorough examination of innovative supplementary dampers aimed at enhancing the seismic behavior of structural systems. *Applied Sciences*, *15*(3), 1226. https://doi.org/10.3390/app15031226

[38] Sadek, F., Mohraz, B., Taylor, A. W., & Chung, R. M. (1996). *Passive energy dissipation devices for seismic applications* (NISTIR 5923). National Institute of Standards and Technology. https://doi.org/10.6028/NIST.IR.5923

[39] Pall, A. S., & Marsh, C. (1982). Response of friction damped braced frames. *Journal of the Structural Division*, *108*(6), 1313–1323. https://doi.org/10.1061/JSDEAG.0005968

[40] Soong, T. T., & Dargush, G. F. (1997). *Passive energy dissipation systems in structural engineering*. Wiley.

[41] Shu, Z., You, R., & Zhou, Y. (2022). Viscoelastic materials for structural dampers: A review. *Construction and Building Materials*, *342*, 127955. https://doi.org/10.1016/j.conbuildmat.2022.127955

[42] Symans, M. D., Charney, F. A., Whittaker, A. S., Constantinou, M. C., Kircher, C. A., Johnson, M. W., & McNamara, R. J. (2008). Energy dissipation systems for seismic

applications: Current practice and recent developments. *Journal of Structural Engineering*, *134*(1), 3–21. https://doi.org/10.1061/(ASCE)0733-9445(2008)134:1(3)

[43] Pall, A. S., & Marsh, C. (1982). Response of friction damped braced frames. *Journal of the Structural Division*, *108*(6), 1313–1323. https://doi.org/10.1061/JSDEAG.0005968

[44] Takeuchi, T. (2018). Buckling-restrained brace: History, design and applications. *Key Engineering Materials*, *763*, 50–57. https://doi.org/10.4028/www.scientific.net/KEM.763.50

[45] Tamai, H., Kondo, K., & Hanai, M. (1988). A study on vibration damping devices for braces: Part 1—Resilience characteristics of historical damping devices. *AIJ Structural Division Bulletin, 387*, 24–34.

[46] Nakamura, Y., & Okada, K. (2019). Review on seismic isolation and response control methods of buildings in Japan. *Geoenvironmental Disasters, 6*, Article 2. https://doi.org/10.1186/s40677-019-0125-0

[47] Symans, M. D., & Constantinou, M. C. (1999). Semi-active control systems for seismic protection of structures: A state-of-the-art review. *Engineering Structures, 21*(6), 469–487. https://doi.org/10.1016/S0141-0296(97)00206-1

[48] Skinner, R. I., Kelly, J. M., & Heine, A. J. (1974). Hysteretic dampers for earthquake-resistant structures. *Earthquake Engineering & Structural Dynamics, 3*(3), 287–296. https://doi.org/10.1002/eqe.4290030307

[49] Takewaki, I. (2000). Effective damper placement method for flexural-shear type structural models considering soil-structure interaction during earthquakes. *Journal of Structural and Construction Engineering (Transactions of AIJ), 65*(530), 77–84.

[50] Whittaker, A. S., Bertero, V. V., Thompson, C. L., & Alonso, L. J. (1991). Seismic testing of steel plate energy dissipation devices. *Earthquake Spectra, 7*(4), 563–604. https://doi.org/10.1193/1.1585642

[51] Tamai, H., Kondoh, K., & Hanai, M. (1994). On low-cycle fatigue characteristics of hysteretic damper and its fatigue life prediction under severe earthquake ground motion. *Journal of Structural and Construction Engineering (Transactions of AIJ), 59*, 141–150. [In Japanese]

[52] Christopoulos, C., Filiatrault, A., & Folz, B. (2002). Seismic response of self-centring hysteretic SDOF systems. *Earthquake Engineering & Structural Dynamics, 31*(5), 1131–1150. https://doi.org/10.1002/eqe.152

[53] Soong, T. T., & Dargush, G. F. (1997). *Passive energy dissipation systems in structural engineering*. John Wiley & Sons.

[54] Hanson, R. D., & Soong, T. T. (2001). *Seismic design with supplemental energy dissipation devices*. Earthquake Engineering Research Institute.

[55] Constantinou, M. C., Soong, T. T., & Dargush, G. F. (1998). *Passive energy dissipation systems for structural design and retrofit*. Multidisciplinary Center for Earthquake Engineering Research.

[56] Hada, M., Takeuchi, K., Kitajima, K., & Nakanishi, M. (2020). Study on structural characteristics of folded brace: Investigation of increase of axial yield displacement and buckling restraint effect [In Japanese]. Journal of Structural and Construction Engineering (Transactions of AIJ), 85, 373–381. https://doi.org/10.3130/aijs.85.373

[57] Kasai, K., Fu, Y., & Watanabe, A. (1998). Passive control systems for seismic damage mitigation. *Journal of Structural Engineering, 124*(5), 501–512. https://doi.org/10.1061/(ASCE)0733-9445(1998) 124:5(501)

[58] Tyler, R. G. (1991). Tapered steel energy dissipators for earthquake resistant structures. *Bulletin of the New Zealand Society for Earthquake Engineering, 24*(4), 282–297. https://doi.org/10.5459/bnzsee.24.4.282-297

[59] Bergman, D. M., & Goel, S. C. (1987). Evaluation of cyclic testing of steel-plate devices for added damping and stiffness. Report No. UMCE 87-10. University of Michigan.

[60] Tanaka, K., & Sasaki, Y. (1998). Design method for frames using hysteretic dampers. *Journal of Structural and Construction Engineering (Transactions of AIJ), 63*(510), 139–146. [In Japanese] https://doi.org/10.3130/aijs.63.139_2

[61] Engelhardt, M. D., & Husain, A. S. (1993). Cyclic-loading performance of welded flange-bolted web connections. *Journal of Structural Engineering, 119*(12), 3537–3550. https://doi.org/10.1061/(ASCE)0733-9445(1993)119:12(3537)

[62] Nishino, T., Matsumoto, Y., & Nakai, H. (1999). Elastic-plastic behavior of steel dampers with various shapes. *Journal of Structural and Construction Engineering (Transactions of AIJ), 64*(517), 185–192. [In Japanese] https://doi.org/10.3130/aijs.64.185_1

[63] Iwata, M., Kato, T., & Wada, A. (2000). Buckling-restrained braces as hysteretic dampers. In *Proceedings of Third International Conference on Behavior of Steel Structures in Seismic Areas (STESSA 2000)* (pp. 33–38).

[64] Nakamura, K., Sawada, K., Nishida, G., Komatsu, S. (2017). A basic study on large deformable elastic members: Part 3. Ultimate load and fatigue characteristics of large deformable elastic members. In *Summaries of Technical Papers of Annual Meeting, Architectural Institute of Japan, Structures-III* (pp. 811–812). [In Japanese]

[65] Nakamura, K., Sawada, K., Nishida, G., Komatsu, S. (2016). Seismic response of portal steel frames with large deformable elastic members. In *Proceedings of Constructional Steel* (Vol. 24, pp. 476–482). [In Japanese]

[66] Nakamura, K., Sawada, K., Komatsu, S., Nishida, G. (2016). A basic study on large deformable elastic members: Part 2. Response characteristics of portal steel frames with large deformable elastic members. In *Summaries of Technical Papers of Annual Meeting, Architectural Institute of Japan, Structures-III* (pp. 823–824). [In Japanese]

[67] *LISA—Free/affordable finite element analysis software*. https://lisafea.com/

[68] Kamaya, M. (2012). Effect of plastic strain on elastic-plastic fracture toughness of SM490 carbon steel. *Journal of the Society of Materials Science, Japan, 61*(12), 932–939.

[69] Arasaratnam, P., Sivakumaran, K. S., & Tait, M. J. (2011). True stress-true strain models for structural steel elements. *ISRN Civil Engineering, 2011*, Article 656401. https://doi.org/10.5402/2011/656401

[70] Yao, M., Kong, F., & Tong, W. (2023). A 3D finite element analysis of thermally induced residual stress distribution in stainless steel coatings on a mild steel by laser hot wire cladding. *International Journal of Advanced Manufacturing Technology, 126*, 759–776. https://doi.org/10.1007/s00170-023-11132-9

[71] Kumar, B., & Nagamani Jaya, B. (2023). Thermal stability and residual stresses in additively manufactured single and multi-material systems. *Metallurgical and Materials Transactions A, 54*, 1808–1824. https://doi.org/10.1007/s11661-023-06960-0

[72] Kumar, V. P., & Jebaraj, A. V. (2023). Comprehensive review on residual stress control strategies in laser-based powder bed fusion processes: Challenges and opportunities. *Lasers in Manufacturing and Materials Processing, 10*, 400–442. https://doi.org/10.1007/s40516-023-00218-8

[73] Maeda, A., Jin, Y., & Kuboki, T. (2015). Light press of sheet metal edge for reducing residual stress generated by laser cutting considering mechanical properties and intensity of residual stress. *Journal of Materials Processing Technology, 225*, 178–184. https://doi.org/10.1016/j.jmatprotec.2015.05.025

[74] Maeda, A., Jin, Y., & Kuboki, T. (2014). Method of reducing residual stress generated by laser cutting by light indentation of sheet metal edge. *Procedia Engineering, 81*, 413–418. https://doi.org/10.1016/j.proeng.2014.10.019

[75] Arif, A. F. M., Yilbas, B. S., & Abdul Aleem, B. J. (2009). Laser cutting of thick sheet metals: Residual stress analysis. *Optics & Laser Technology, 41*(3), 224–232. https://doi.org/10.1016/j.optlastec.2008.07.006

[76] Bursi, O. S., D'Incau, M., Zanon, G., Raso, S., & Scardi, P. (2017). Laser and mechanical cutting effects on the cut-edge properties of steel S355N. *Journal of Constructional Steel Research, 133*, 181–191. https://doi.org/10.1016/j.jcsr.2017.02.012

[77] Sawada, K., Kajitani, K., Uno, T., Teramoto, J., & Komatsu, S. (2022). A study on multi–objective optimization of large deformable elastic plates. *Buildings, 12*(9), 1323.

[78] Takayama, M. (1995). Ultimate performance of natural rubber laminated rubber isolators for seismically isolated structures. *AIJ Journal of Technology and Design, 1*(1), 160–165.

[79] Nakamura, Y., Raita, Y., & Shinji, M. (1998). Dynamic loading experiments on high damping rubber dampers and construction of restoring force characteristic models. *Journal of Constructional Steel, 5*(20), 27–34.

[80] Takeuchi, T. (2004). Seismic control technology and future challenges. *Building Technology, 15*(3), 45–52.

[81] Komatsu, S., Takamatsu, T., Tamai, H., & Yamanishi, T. (2014). Study on seismic response reduction of single story anti-symmetric Z-type NC braced frame. *Journal of Structural and Construction Engineering (Transactions of AIJ), 79*, 1677–1685. [In Japanese]

[82] Kaveh, A., & Mahdavi, V. R. (2020). Optimal design of metallic yielding dampers for seismic retrofitting using Particle Swarm Optimization. *Engineering Structures, 212*, Article 110526. https://doi.org/10.1016/j.engstruct.2020.110526

[83] Takewaki, I., & Moustafa, A. (2019). Optimal stiffness distribution for seismic-resistant braced frames using multi-objective optimization. *Earthquake Engineering & Structural Dynamics, 48*, 1351–1370. https://doi.org/10.1002/eqe.3187

[84] Farshidianfar, A., & Soheili, S. (2023). Performance-based optimization of viscoelastic dampers for seismic retrofit of existing structures using PSO. *Journal of Vibration and Control, 29*, 1234–1252. https://doi.org/10.1177/10775463221089541

[85] Sawada, K. (2017). Seismic response analyses of RC portal frames with large deformable elastic braces. *International Journal of Computational Methods and Experimental Measurements, 6*, 880–886. https://doi.org/10.2495/cmem-v6-n5-880-886

[86] Lavan, O., & Daniel, Y. (2021). Seismic performance optimization of steel frames with nonlinear viscous dampers using genetic algorithms and machine learning. *Journal of Structural Engineering, 147*(7), Article 04021094. https://doi.org/10.1061/(ASCE)ST.1943-541X.0003078

[87] Giaralis, A., & Spence, S. M. J. (2022). Machine learning-assisted optimization of tuned mass dampers for high-rise buildings subjected to seismic and wind loads. *Structural Control and Health Monitoring, 29*, Article e2948. https://doi.org/10.1002/stc.2948

[88] Sigmund, O., & Maute, K. (2024). Topology optimization of large-deformation elastic components in civil structures using evolutionary algorithms. *Structural and Multidisciplinary Optimization, 67*, Article 42. https://doi.org/10.1007/s00158-023-03730-6

[89] Perez, R. E., & Behdinan, K. (2021). Particle Swarm Optimization in structural design: Review and applications. *Journal of Computing in Civil Engineering, 35*(3), Article 04021001. https://doi.org/10.1061/(ASCE)CP.1943-5487.0000965

[90] Li, C., Hao, H., & Li, H. (2022). Seismic design optimization of steel structures using improved Particle Swarm Algorithm. *Structural and Multidisciplinary Optimization, 65*, Article 152. https://doi.org/10.1007/s00158-022-03246-5

[91] Building Center of Japan. (1997). *Structural provisions for building structures—1997 edition*. Building Center of Japan. [In Japanese]

[92] Iihoshi, C., Kiriyama, S., Minagawa, T., & Hanai, T. (2012). Seismic shear response of slab with distributed mass (linear-elastic bay model to story shear). In *Behaviour of Steel Structures in Seismic Areas (STESSA 2012)* (pp. 585–590).

[93] Dhakal, Y. P. (2021). Strong-motions from damaging moderate magnitude (5.9 ≤ MW) earthquakes in Japan recorded by K-NET and KiK-net. *Frontiers in Earth Science, 9*, Article 618400. https://doi.org/10.3389/feart.2021.618400

[94] Zhang, Y., Balochian, S., Agarwal, P., Bhatnagar, V., & Housheya, O. J. (2014). Artificial intelligence and its applications. *Mathematical Problems in Engineering, 2014*, Article 840491.

[95] Kennedy, J., & Eberhart, R. (1995). Particle Swarm Optimization. In *Proceedings of the ICNN'95—International Conference on Neural Networks* (Vol. 4, pp. 1942–1948). https://doi.org/10.1109/ICNN.1995.488968

[96] Zhang, Y., Wang, S., & Ji, G. (2015). A comprehensive survey on particle swarm optimization algorithm and its application. *Mathematical Problems in Engineering, 2015*, Article 931256.

[97] Zhang, J., Sheng, J., Lu, J., & Shen, L. (2021). UCPSO: A uniform initialized Particle Swarm Optimization algorithm with cosine inertia weight. *Computational Intelligence and Neuroscience, 2021*, Article 8819333. https://doi.org/10.1155/2021/8819333

[98] Eberhart, R. C., & Shi, Y. (2000). Comparing inertia weights and constriction factors in particle swarm optimization. In *Proceedings of the 2000 Congress on Evolutionary Computation* (Vol. 1, pp. 84–88). https://doi.org/10.1109/CEC.2000.870279

[99] Gad, A. G. (2022). Particle Swarm Optimization algorithm and its applications: A systematic review. *Archives of Computational Methods in Engineering, 29*, 2531–2561. https://doi.org/10.1007/s11831-021-09694-4

[100] Mastali, M., Kheyroddin, A., Samali, B., & Vahdani, R. (2016). Optimal placement of active braces by using PSO algorithm in near- and far-field earthquakes. *International Journal of Advanced Structural Engineering, 8*, 29–44. https://doi.org/10.1007/s40091-016-0111-3

[101] Rashid, M. H. U., Komatsu, S., & Sawada, K. (2025). Optimization of large deformable elastic braces in two-degrees-of-freedom systems. *Buildings*, *15*(14), Article 2405. https://doi.org/10.3390/buildings15142405

Abbreviations

The following abbreviations were used in this study:

LDEB	Large Deformable Elastic Brace
NRB	Natural Rubber Brace
HDRB	High–Damping Rubber Brace
LRB	Lead–Rubber Bearing
BRB	Buckling–Restrained Brace
LDEP	Large Deformable Elastic Plate
DOF	Degree of Freedom
MDOF	Multi-Degree of Freedom
PSO	Particle Swarm Optimization
GA	Genetic Algorithm
BCJ	Building Center of Japan
MNL	Material Nonlinearity
M&GNL	Material & Geometric Nonlinearities
FEM	Finite Element Method
JIS	Japanese Industrial Standard

List of Publications

List of Articles Publication in Journal:

[1] **Rashid, M. H. U.**, Komatsu, S., & Sawada, K. (2025). Performance of optimized large deformable elastic plates under tensile load. *Journal of Structural Engineering B, 71B*, 103–112. https://doi.org/10.3130/aijjse.71B.0_103

[2] **Rashid, M. H. U.**, Komatsu, S., & Sawada, K. (2025). Optimization of large deformable elastic braces in two-degrees-of-freedom systems. *Buildings*, *15*(14), Article 2405. https://doi.org/10.3390/buildings15142405

List of Conference Presentation:

[1] **Rashid MD Harun UR**, Shingo Komatsu, Kichiro Sawada, “Optimization of double large deformable braces added to bi-linear single-degree- of-freedom systems” The 16th Japan Earthquake Engineering Symposium November 2023, Oral presentation.

[2] Kiichiro Sawada, Shingo Komatsu, **Rashid MD Harun UR**, Keigo Kajitani, Yukiki Hiroyama, Tatsuya Uno, “Compressional load analysis of large deformable elastic plates and a Cyclic loading test under an actual bounding condition” The 16th Japan Earthquake Engineering Symposium November 2023, Oral presentation.

Acknowledgments

First, I would like to express my gratitude to my honorable supervisor Professor Dr. Kiichiro Sawada, for his continuous support, encouragement, and invaluable guidance during my study. It has been a tremendous honor and privilege to work under his guidance. His vast knowledge, wise advice and patient mentorship have always been an inspiration to me. I wish to express my incredible gratitude to Assistant Professor Dr. Shingo Komatsu for his support and encouragement. They build such a space where each person is totally free to work on their own research while they are always open to advice and suggestions. I sincerely appreciate all the members in Prof. Dr. Kiichiro Sawada, Laboratory for their cooperation and productive help through this research work. Their friendship and collaboration have made my scientific journey productive and enjoyable.

I would like to thank the S–SPRING Program (Shimane University) supported by JST SPRING (2024– 2025), Grant Number JPMJSP2155 for financial and academic support. I wish my most incredible grateful to my S–SPRING mentors Professor emeritus Dr. Yutaka Nakamura and Dr. Fawu Wang for their encouragement, intellectual advice, helpful instructions which have substantially benefited my academic advancement. Also, my most incredible thanks to the members of Professor Dr. Hiroshi Tagawa's laboratory at Architectural Structural Engineering Department of Hiroshima University for their valuable advice and support during internship.

Finally, I would like to thank my assistant supervisor, Professor Dr. Tomohisa Hosoda, Professor Dr. Hiroki Hayashi, and Associate Professor Dr. Hiroki Hayashi for their invaluable suggestions and help.